

Compositional and interfacial optimization for enhancement of perovskite solar cells performance

Présentée le 16 février 2022

Faculté des sciences de base
Laboratoire de photonique et interfaces
Programme doctoral en photonique

pour l'obtention du grade de Docteur ès Sciences

par

Essa Awadh R ALHARBI

Acceptée sur proposition du jury

Prof. J.-E. Moser, président du jury
Prof. M. Graetzel, Dr S. M. Zakeeruddin, directeurs de thèse
Prof. T. Sargent, rapporteur
Dr S. Stranks, rapporteur
Prof. R. Buonsanti, rapporteuse

Acknowledgment

First of all, I would like to thank my supervisors Prof. Michael Graetzel and Dr. S. M. Zakeeruddin for giving me the possibility to explore my scientific creativity and acquire valuable in-depth research experience at LPI. They encourage me to explore the uncertainties and guide me for scientific research and academic career. They showed me how to think scientifically and ethically and I will take their pieces of advice for the rest of my scientific carrier. So, doing my Ph.D. at LPI is one of the best options, I have ever made in my life.

I would like to especially thank Dr. Anurag Krishna, for all his support, collaboration, and motivation which immensely help in my Ph.D. journey. I would like to thank Dr. Ibrahim Dar and Dr. Neha Arora for training me in device fabrication as well as for the collaboration.

Also, I would like to thank my friends and colleagues: Thomas Baumeler, Algirdas Ducinskas, Viktor Škorjanc, Gabriele, Dr. Sandy, Dr. Natalie, Dr. Yameng, Dr.Zaiwei and Dr.Bowen.

I would like to thank our collaborators, Prof. Lyndon Emsley, Dr. Dominik J. Kubicki for their collaboration in NMR measurements, as well as Prof. Ursula Roethlisberger and Mathias Dankl for their help in DFT calculations. Also, I would like to express my **acknowledgment** to Prof. Jacques-E Moser and George C. Fish for the collaboration as well. Moreover, Pascal Schouwink and Mounir Mnesi are acknowledged for their assistance with XRD and XPS, respectively.

I would like also to thank Dr. Lukas Pfeifer, Dr. Felix Eickemeyer, and Dr. Olivier Ouellette for very fruitful discussions and collaborations. Also, I would like to thank Prof. Ahmed Alyamani, Dr. Abdulrahman Albadri, Dr. Mohammad Hayal Alotaibi, Fahad Alghamdi and Dr. Hamad A. H. Albrithen from KACST for their help during my Ph.D. study.

I thank Heidi , Cathy Buchs and Carmen for their great help regarding the administrative stuff.

Last but not the least, I am extremely grateful to my family for their love, patience, and support throughout my Ph.D.

Abstract

Non-renewable sources are responsible for most of the overall greenhouse gas emissions, the development of sustainable energy sources is of prime importance in order to mitigate the negative effects of climate change. Among renewable sources, solar energy is one of the most abundant forms of energy available. Photovoltaic (PV) devices are used to convert solar energy into electricity. Among next-generation PV devices, metal halide perovskites-based PV has emerged becoming one of the most promising PV technology. The first breakthrough occurred in 2009 when Miyasaka's group reported a methylammonium lead iodide (MAPbI₃) based PV device with a PCE of 3.8%. Since then there has been an unprecedented rise in the perovskite solar cells (PSCs) with a certified PCE of 25.5% reported in 2020. However, despite the big improvement in PCE just in few years, some critical issues need to be carefully addressed, such as defects and solvent toxicities, and, most importantly, the intrinsic material and device instability.

Chapter 2. To gain high photovoltages and power conversion efficiencies of perovskite solar cells (PSCs) can be realized by controlling the undesired nonradiative charge carrier recombination. Here, we introduce a judicious amount of guanidinium iodide into mixed-cation and mixed-halide perovskite films to suppress the parasitic charge carrier recombination, which enabled the fabrication of >20% efficient and operationally stable PSCs yielding reproducible photovoltage as high as 1.20 V. By introducing guanidinium iodide into the perovskite precursor solution, suppression in the nonradiative recombination occurred considerably as revealed by time-resolved photoluminescence and electroluminescence studies. Furthermore, using capacitance-frequency measurements, we were able to correlate the hysteresis features exhibited by the PSCs with interfacial charge accumulation. This study opens up a path to realize new record efficiencies for PSCs based on guanidinium iodide doped perovskite films.

Chapter 3. We introduce a straightforward strategy to reduce the level of electronic defects present at the interface between the perovskite film and the hole transport layer by treating the perovskite surface with different types of ammonium salts, namely ethylammonium, imidazolium, and guanidinium iodide. We use a triple cation perovskite formulation containing primarily formamidinium and small amounts of cesium and methylammonium. We find that this treatment boosts the power conversion efficiency from 20.5% for the control to 22.3%, 22.1%, and 21.0% for the devices treated with

ethylammonium, imidazolium, and guanidinium iodide, respectively. Best performing devices showed a loss in efficiency of only 5% under full sunlight intensity with maximum power tracking for 550 h. We apply 2D- solid-state NMR to unravel the atomic-level mechanism of this passivation effect.

Chapter 4. We report a facile and very effective method that employs methylammonium triiodide (MAI₃) as an additive to the perovskite precursor solution for holistic defect mitigation in a perovskite semiconductor. Specifically, TRPL and TRTS show that MAI₃ suppresses non-radiative recombination and increases the charge carrier mobility. As a result, the champion device shows a power conversion efficiency (PCE) of 23.46% with a high fill factor (FF) of over 80%. Furthermore, these devices exhibit enhanced operational stability, with the best device retaining ~ 90% of its initial PCE under 1 Sun illumination with maximum power point tracking for 350 h.

Chapter 5. We reconfigured the design of the alkylammonium salts to create a holistic bulk and interface engineering of α -FAPbI₃ perovskite. We showed that dimethylammonium head along with octyl chain and iodide counter anion works best in the bulk whereas dimethylammonium head along with octyl chain and fluoride counter anion works best at the surface. With a synergistic combination of both bulk and surface passivation, we achieved a high PCE of 24.91% along with exceptional long-term operational stability.

Keywords.

Perovskite Solar cells, Spin coating, Antisolvents method, compositional engineering, radiative and non-radiative recombination, defect engineering, surface passivation, Stability.

Résumé

Les sources d'énergie non-renouvelables sont responsables de la majeure partie des émissions globales de gaz à effet de serre. Le développement de sources d'énergie renouvelables est donc d'une importance cruciale afin de mitiger les changements climatiques et leurs effets néfastes. Parmi les sources renouvelables, l'énergie solaire est l'une des plus abondantes. Les cellules photovoltaïques (PV) sont utilisées pour convertir l'énergie solaire en électricité. Parmi les technologies photovoltaïques de nouvelle génération, les cellules à base de pérovskites de métaux-halogènes se sont imposées comme l'une des plus prometteuses. La première percée eut lieu en 2009 lorsque le Prof. Miyasaka et son groupe ont présenté une cellule PV à base d'iodure de plomb de methylammonium (MAPbI_3) ayant une efficacité de conversion de puissance de 3.8%. Depuis, la recherche sur les cellules à pérovskites croît à un rythme sans précédent, l'efficacité record obtenue en 2020 se trouvant désormais à 25.5%. Toutefois, malgré ces rapides progrès, certaines problématiques critiques demeurent, telles que les défauts cristallins, la toxicité des solvants utilisés et, la plus importante, l'instabilité intrinsèque des matériaux et des cellules.

Chapitre 2. Des photovoltages et des efficacités élevés peuvent être obtenus en contrôlant la recombinaison non-radiative indésirable des porteurs de charge. Dans ce chapitre, nous présentons incorporation d'une quantité judicieuse d'iodure de guanidinium dans des films de pérovskites multi-cations et multi-halogènes pour réduire la recombinaison des porteurs de charge, ce qui a rendu possible la fabrication de cellules à pérovskites stables en opération, dont l'efficacité dépasse les 20% et produisant de façon reproductible un photovoltage atteignant 1.20V. En introduisant l'iodure de guanidinium dans la solution précurseur de pérovskites, la recombinaison non-radiative est considérablement inhibée, ce qui est révélé au moyen de mesures de photoluminescence et électroluminescence résolue dans le temps. De plus, à l'aide de mesures de capacité-fréquence, nous avons pu corrélérer les caractéristiques d'hystérèse des cellules solaires et l'accumulation de charges interfaciales. Cette étude ouvre la voie à la réalisation d'efficacités record pour les cellules solaires à pérovskites dopées à l'iodure de guanidinium.

Chapitre 3. Nous présentons une stratégie simple pour réduire la densité de défauts électroniques présents à l'interface entre le film de pérovskite et la couche de transport de trous en traitant la surface de la couche de pérovskite à l'aide de différents types de sels d'ammonium, soient l'ethylammonium, l'imidazolium et l'iodure de guanidinium. Nous

utilisons une composition de pérovskite à triple cations contenant principalement du formamidinium ainsi que de faibles quantités de césium et de méthylammonium. Nous observons que ce traitement augmente l'efficacité de conversion : de 20.5% pour le contrôle à 22.3%, 22.1% et 21.0% pour les cellules traitées à l'éthylammonium, l'imidazolium et l'iodure de guanidinium, respectivement. Les cellules les plus performantes démontraient des pertes d'efficacité de seulement 5% sous illumination solaire artificielle à 1-Soleil avec suivi du point de puissance maximale pendant 550h. Nous employons la spectroscopie RMN à l'état solide 2-D pour expliquer/démontrer le mécanisme de cet effet de passivation à l'échelle atomique.

Chapitre 4. Nous rapportons une méthode simple et efficace, employant le triiodure de méthylammonium (MAI_3) en tant qu'additif à la solution précurseur de pérovskite, qui permet la mitigation holistique des défauts cristallins dans le semiconducteur de pérovskite. Les spectroscopies THz et de photoluminescence résolues dans le temps montrent spécifiquement que le MAI_3 supprime la recombinaison non-radiative et augmente la mobilité des porteurs de charge. Cette stratégie permet aux cellules championnes d'atteindre une efficacité de 23.46% ainsi qu'un facteur de remplissage dépassant 80%. De plus, ces cellules possèdent une stabilité opérationnelle améliorée, les meilleures cellules maintenant 90% de leur efficacité initiale après 350h d'illumination à 1-Soleil avec suivi du point de puissance maximale.

Chapitre 5. Nous avons reconfiguré le design des sels d'alkylammonium afin d'optimiser de façon holistique le volume et les interfaces de la pérovskite $\alpha\text{-FAPbI}_3$. Nous démontrons qu'une tête de diméthylammonium jointe à une chaîne d'octyl et d'un contre-anion d'iodure donnent les meilleurs résultats pour le traitement du volume, alors qu'une tête de diméthylammonium jointe à une chaîne d'octyl et d'un contre-anion de fluorure fonctionne le mieux pour les surfaces. À l'aide d'une combinaison synergique de passivation simultanée du volume et des surfaces, nous accomplissons une haute efficacité de 24.91% ainsi qu'une stabilité opérationnelle à long terme exceptionnelle.

Mots-clés.

Cellules solaires à pérovskites, spin-coating, méthodes à antisolvants, ingénierie compositionnelle, recombinaison radiative et non-radiative, ingénierie des défauts cristallins, passivation de surfaces, stabilité.

Contents

| | |
|---|-----------|
| Acknowledgement | i |
| Abstract (English) | ii |
| Résumé | iv |
| Contents | vi |
| Chapter 1: Introduction | 1 |
| 1.1 Energy demand and need for photovoltaics | 1 |
| 1.2 Photovoltaic Device parameters | 7 |
| 1.3 Structural and electronic properties of hybrid metal halide perovskites | 10 |
| 1.4 Losses and defects in hybrid metal halide perovskites | 19 |
| 1.5 Mitigation strategy of defects | 14 |
| 1.5.1 Salts and low dimensional perovskites | 22 |
| 1.5.2 Lewis acid | 23 |
| 1.5.3 Lewis base | 24 |
| 1.6 Conclusion | 25 |
| 1.7 Reference | 26 |
| Chapter 2 : Perovskite Solar Cells Yielding Reproducible Photovoltage of 1.20 V | 30 |
| 2.1 Introduction | 30 |
| 2.2 Results | 32 |
| 2.3 Discussion | 39 |
| 2.5 Supplementary Materials | 40 |
| 2.6 References | 45 |
| Chapter 3: Atomic-level passivation mechanism of ammonium salts enabling highly efficient perovskite solar cells | 49 |
| 3.1 Introduction | 49 |
| 3.2 Results | 51 |
| 3.3 Discussion | 61 |
| 3.5 Supporting information | 66 |
| 3.6 References | 79 |

| | |
|--|-----|
| Chapter 4 : Methylammonium triiodide for holistic defect engineering of α-FAPbI₃ perovskite solar cells | 82 |
| 4.1 Introduction | 82 |
| 4.2 Results and discussion | 84 |
| 4.3 Conclusion | 96 |
| 4.4 Supplementary information | 96 |
| 4.5 Reference | 102 |
| Chapter 5: Reconfiguring the molecular design for the engineering of bulk and interface enables high efficiency and stable perovskite photovoltaics | 117 |
| 5.1 Introduction of Designing the ammonium Halide as Passivators | 117 |
| 5.2 Photovoltaic performance of the ammonium halide-treated perovskites | 118 |
| 5.3 Conclusion | 129 |
| 5.5 Reference | 130 |
| Chapter 6: Conclusion | 134 |

Chapter 1.

Introduction

1.1 Energy demand and need for photovoltaics

An overall increase in the global population and enhancement of quality of life has meant that the global energy demand is on the rise. Current estimates show that the overall energy consumption (16 TW) will nearly double by 2050 (30 TW), and more than triple by 2100 (50 TW)¹. This will put a major strain on the global supply chain, making sufficient energy production one of the major challenges of the 21st century. Meeting the energy demand will be even more challenging due to efforts to deter non-renewable energy sources (such as coal, oil, gas), which constitute 80% of current energy consumption² as shown in **Figure 1.1**. Since non-renewable sources are responsible for most of the overall greenhouse gas emissions, the development of sustainable energy sources is of prime importance to mitigate the negative effects of climate change. Among renewable sources, solar energy is one of the most abundant form of energy available (**Figure 1.2**). Typically, the amount of energy that the Sun delivers to Earth in one hour is higher than the current annual global consumption thus solar energy has the potential to deliver over 400 times higher than the predicted energy demand in 2100 horizon³. However, we need a highly efficient system to convert solar energy into electricity. To this end, photovoltaic devices have emerged as the means to efficiently convert solar energy into electricity.

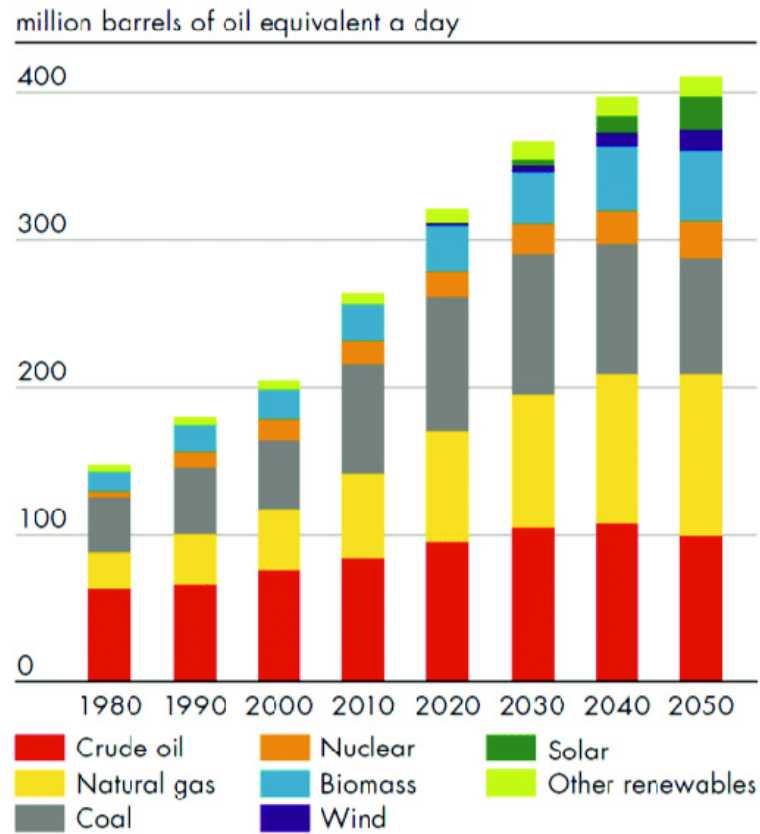


Figure 1.1 illustration of demand energy up to 2050⁴.

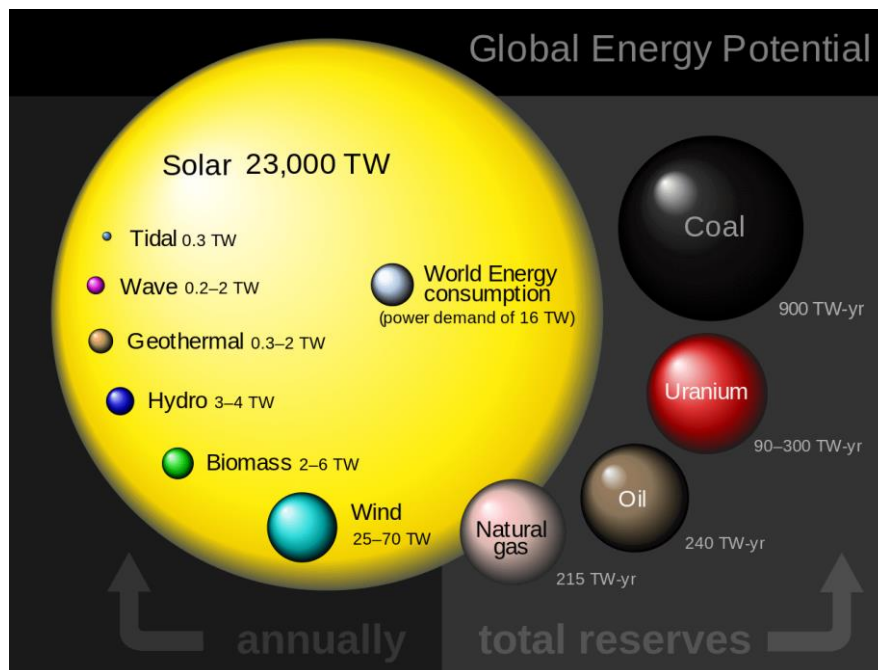


Figure 1.2 Comparing finite and renewable planetary energy reserves (Terawatt-years).⁵

The photovoltaic effect is the generation of voltage and electric current in a material upon exposure to light, which was first described and demonstrated by Edmond Becquerel in 1839 when he used an electrochemical cell that produced electrical power when exposed to light⁶. Inspired by Becquerel's discovery, Charles Fritts produced the first-ever photovoltaic module by coating Selenium with a thin layer of gold. He reported that such cell produced "a current that is continuous, constant and of considerable force", with the cell reaching an estimated power conversion efficiency (PCE) of 1-2%⁷. The next breakthrough happened in the 1950s in Bell Laboratories, where Chapin, Fuller, and Pearson reported "a new silicon *p-n* junction photocell for converting solar radiation into electrical power". The devices they made delivered PCE as high as 6%⁸. From then on, progress in silicon PV technology was made continuously, with mono- and polycrystalline silicon solar cells (sc-Si and pc-Si) reaching PCEs of 26.1% and 23.3% respectively⁹. While silicon PV has emerged as efficient technology but it has not yet substituted fossil fuels mainly due to an intensive fabrication process which increases the production cost, and causes environmental concerns¹⁰. Other PV technologies, based on inorganic thin film, cadmium telluride (CdTe, PCE = 21.0%), gallium arsenide (GaAs, PCE = 29.1%), copper indium gallium selenium (CIGS, PCE = 23.3%), and Copper zinc tin sulfide (CZTS, PCE = 10.0%)¹¹ have emerged as a potential substitute for silicon, but these solar cells never managed to overtake silicon solar cells as the market leader, because of cumbersome fabrication process or potential toxicity of the materials used. Thus, the global PV market is silicon-dominated, with sc-Si and pc-Si constituting 35% and 55% of today's market shares respectively¹¹, and the market share of all thin-film technologies including CdTe (2.3 %), copper indium gallium diselenide or CIGS (1.9 %), and amorphous-Si (0.3 %) amounts to only around 4.5 % of total global solar module production¹². However, despite reaching high efficiency, such technology also comes with high fabrication costs and strong environmental impact, and they alone cannot harvest the full potential of solar energy¹³.

A breakthrough occurred in 2009 when Miyasaka's group published the first peer-reviewed paper reporting the use of an "organometal halide perovskite as visible-light sensitizer for photovoltaic cells in the DSSC device configuration". They replaced the organic dyes in a liquid DSSC with nanocrystals of methylammonium lead iodide ($\text{CH}_3\text{NH}_3\text{PbI}_3 = \text{MAPbI}_3$) and methylammonium lead bromide ($\text{CH}_3\text{NH}_3\text{PbBr}_3 = \text{MAPbBr}_3$) perovskites and reported a PCE of 3.8% with an impressive V_{OC} of 0.96 V¹⁸. In 2012, a tremendous increase in the power conversion efficiency was achieved when liquid electrolyte, initially used by Miyasaka's group, was replaced by spiro-OMeTAD HTM, delivering a PCE of 9.7% with improved J_{SC} and drastically better stability¹⁹. The fact that the perovskite material is rather cheap and easy to synthesize and process for solar cell fabrication encouraged the scientific community to focus on perovskites as efficient light absorbers for photovoltaic solar cells, which caused a sharp growth in the number of perovskite-related publications during the previous decade (**Figure 1.4a**). During this time, several major advances made in (**Figure 1.4b**), compositional, bulk, and interfacial engineering along with the development of new processing methodologies has lead the PCE of PSCs to reach recently as high as 25.5%¹⁷ (**Figure 1.3**).

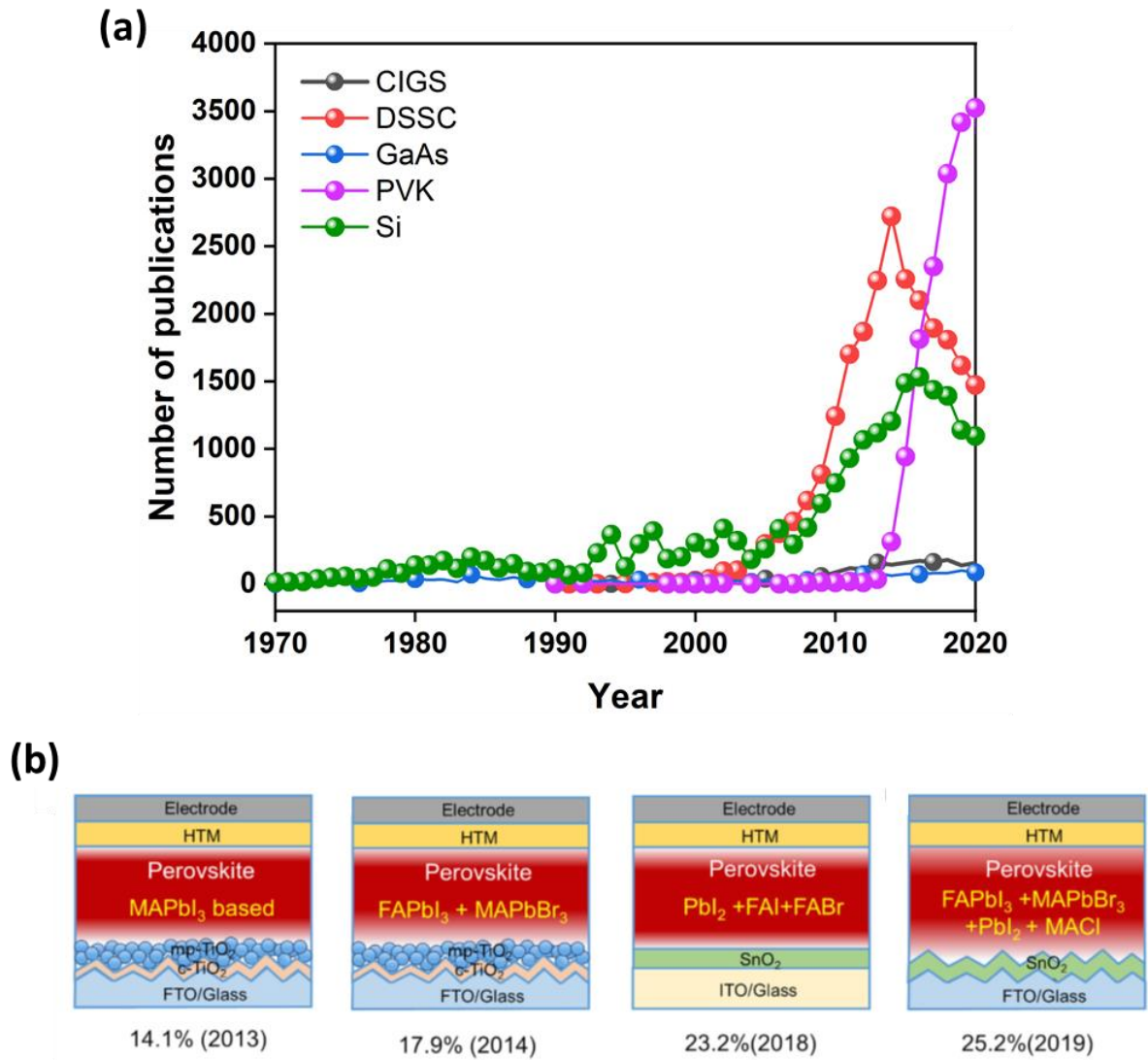


Figure 1.4 (a) Number of publications as a function of years and (b) Changes in the structure and composition of PSCs according to the conversion efficiency record²⁰.

1.2 Photovoltaic Device parameters

To evaluate the power conversion efficiency (PCE) for a solar cell device a current-voltage characteristic (J - V) measurement should be taken under AM1.5G illumination (1 Sun illumination (**Figure 1.5a,b**)).

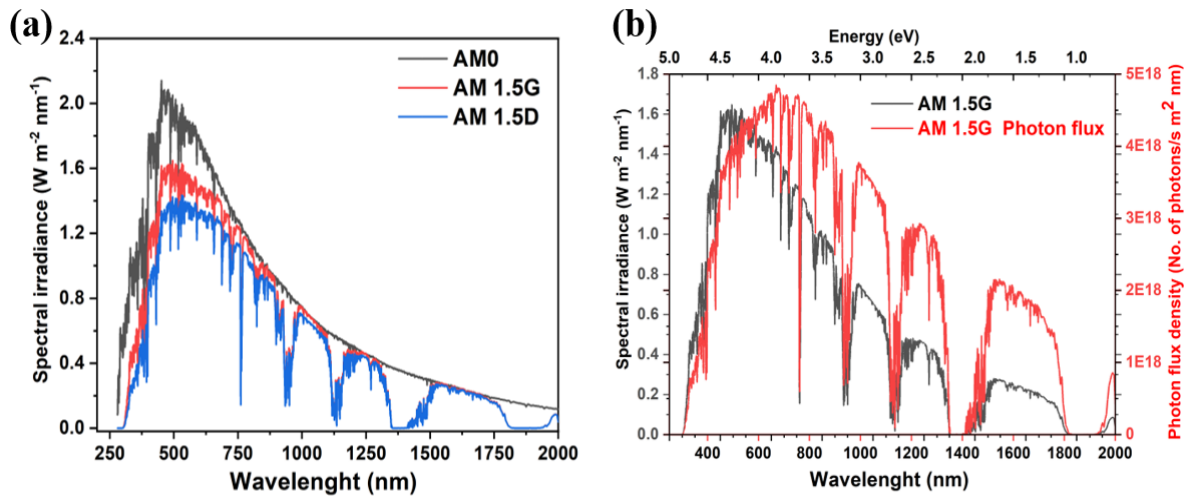


Figure 1.5 (a) Spectral irradiance of AM0, AM1.5G, AM1.5D, and (b) Spectral irradiance of AM1.5G, photon energy, and photon flux density as a function of wavelength, respectively.

Three parameters should be extracted to define the PCE of the solar cell device viz. short circuit density (J_{sc}), open-circuit voltage (V_{oc}), and fill factor (FF) as shown in Figure 1.6. Thus, the PCE of a solar cell device can be easily defined as the ratio of the output electrical power provided by the cell to the power input of the incident light.

Also, the maximum power point (MPP) that is used as a main operational point from the (J - V) curve, which defined as the product of the maximum current and voltage that the solar cells device could be delivered ($P=J_m \times V_m$). Then, the PCE and FF can be calculated by:

$$PCE = \frac{P_{out}}{P_{in}} = \frac{J_m \times V_m}{P_{in}} = \frac{J_{sc} \times V_{oc} \times FF}{P_{in}} \quad (1.1)$$

$$FF = \frac{J_m \times V_m}{J_{sc} \times V_{oc}} \quad (1.2)$$

J_{sc} is measured at the short circuit (0V, J_{sc}) and V_{oc} is measured at the open circuit (V , 0mA) and the FF is a factor of quality of the solar cells and how far from measured solar cell performances are from the theoretical maximum values, as a function of voltage and current. In reality, the solar cells are dissipated via series resistance (R_{series}) and shunt resistance (R_{shunt}). R_{series} an electrical loss at the contacts and a R_{shunt} represent the leakage current. This new expression becomes the so-called solar cell equation:

$$J(V) = J_{sc} - J_0 \left(\exp \left(\frac{q(V+JR_s)}{nK_B T} \right) - 1 \right) - \frac{V+JR_s}{R_{sh}} \quad (1.3)$$

From the equation (1.3), it has to minimize losses, which means a very low series resistance (R_{series}) and high shunt resistance (R_{shunt}) and the typical J - V curve plot, it could be extracted as shown in **Figure 1.6**.

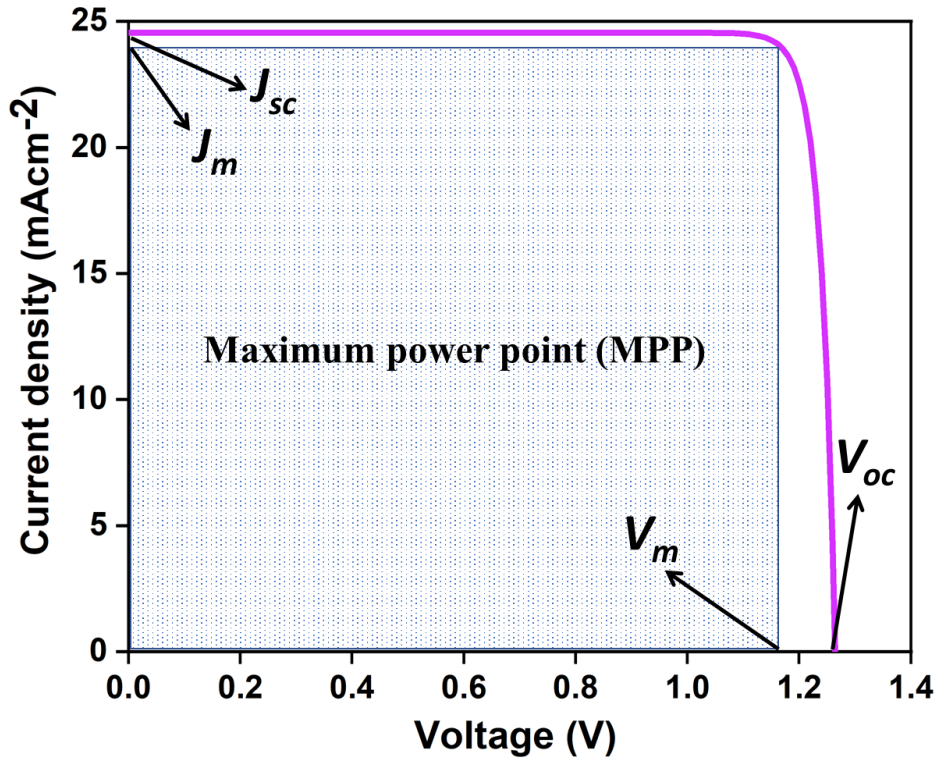


Figure 1.6 A J - V curve of a solar cell under 1 Sun illumination.

Solar cell device is a diode (rectifying behavior), which means that a dark current (J_0) under applied voltage (V) will be produced which flows oppositely to, when light put on the device with energies matches the bandgap of the absorber layer, the photogenerated current density as area dependence known as J_{sc} is produced and the total short circuit current density (J) and V_{oc} can be written, respectively, as:

$$J(V) = J_{sc} - J_0 \left(e^{\frac{qV}{nk_B T}} - 1 \right) \quad (1.4)$$

$$V_{oc} = \frac{kT}{q} \ln \left(\frac{J_{sc}}{J_0} + 1 \right) \quad (1.5)$$

1.3 Structural and electronic properties of hybrid metal halide perovskites

The origin of perovskite name refers to any crystal structure of such as calcium titanate (CaTiO_3), which was discovered by the German mineralogist Gustav Rose in 1839 and named in honor of the Russian mineralogist Lev Perovski (1792-1856). The general structural formula of perovskite is ABX_3 ²¹.

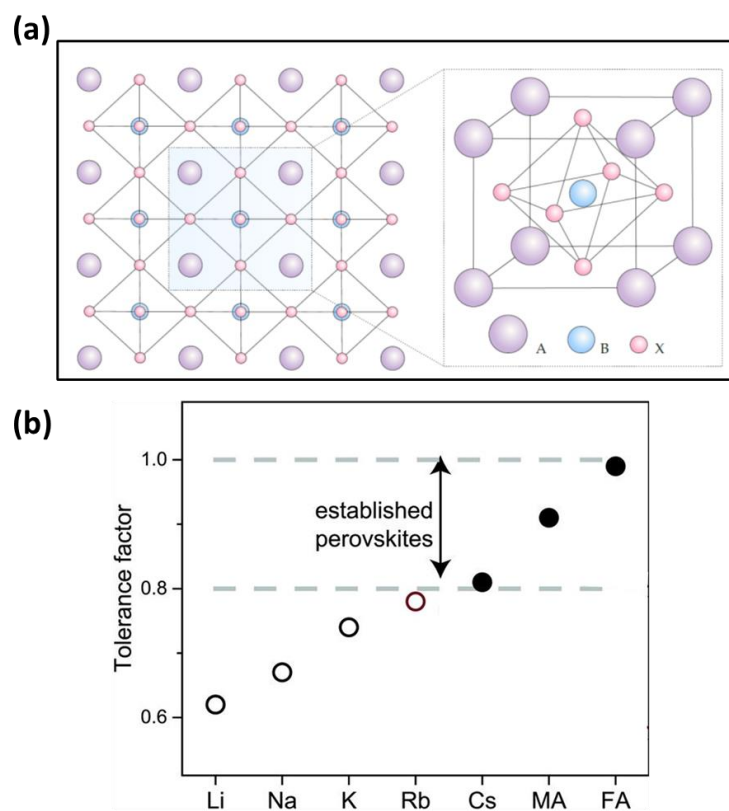


Figure 1.7 (a) Perovskite structure and (b) tolerance factor²².

In hybrid metal halide perovskites (MHPs), the A, B and X sites are occupied by an organic/inorganic cation (e.g. Cs^+ , MA^+ , FA^+ , EA^+ , GA^+), metal cation (e.g. Pb^{2+} , Sn^{2+} , Ge^{2+} , Mg^{2+} , Ca^{2+} , Sr^{2+} , Cu^{2+} , Ni^{2+}) and halide (e.g., I^- , Br^- , Cl^-), respectively. In an ideal perovskite structure with cubic symmetry, the B cation is coordinated by an octahedron of anions (BX_6) which extend in a three-dimensional network with corners sharing as shown in **Figure 1.7a**. The organic cations occupy the 12-fold coordinated voids among the octahedra to fill in the space between the octahedra for balancing the charge of the entire network. The prediction of ideal perovskite structure can be estimated by the Goldschmidt tolerance factor (TF) and an octahedral factor (μ) respectively. TF is defined as an empirical index to predict the stable crystal structure of the perovskite material and μ as an indicator between A-X and B-X bonds length to measure the mismatch in the level of distortion in the system. TF and μ are expressed as $TF = \frac{r_A + r_X}{\sqrt{2}(r_B + r_X)}$ where r is the ionic radii of A, B, X (ABX_3), and $\mu = \frac{r_B}{r_A}$ respectively²³. If A-site is too small or A-site too large that will make the TF below one or higher than one respectively, which means the crystal structure distorted and could be out of the established 3D cubic perovskite regime (**Figure 1.7b**), and making a mixture of crystal structure such as orthorhombic, rhombohedral, or tetragonal. Achieving the cubic crystal system empirically, the TF should meet between 0.8- 1 and μ between 0.4-0.8²⁴. Incorporating too large a cation, the 3D crystal structure of perovskite would break into the low dimensional (2D, 1D, and 0 D) structure (**Figure 1.8**). Each one of these materials has its unique physical and chemical properties with suitability for applications such as optoelectronic devices, photovoltaics (PVs), light-emitting diodes (LEDs), photodetectors, lasers, etc. Typically, the low dimensional perovskites, connected as the face, corner, and edge-sharing to the organic cation. For instance, a 2D perovskite consists of single (or multiple) inorganic sheets of corner-sharing $[\text{BX}_6]^{4-}$ octahedrons sandwiched between organic spacers held together by Coulombic forces²³ and expressed in this structural formula of $\text{R}_2\text{A}_{n-1}\text{B}_n\text{X}_{3n+1}$ where, R is the bulky or a

primary aliphatic or aromatic alkylammonium cation that acts as a spacer between the inorganic sheets, B is a divalent metal, X is a halide anion and n stands for the number of inorganic layers held²⁵. In the case of 1D structure, the BX_6 octahedra are connected in a chain (at the corners, edges, or faces), whereas, in the 0D structure, the BX_6 octahedra are isolated and surrounded by organic cations²⁶. The chemical formulas are changeable depending on the connecting methods and the organic cations chosen. It should be noted that the assembling of 2D (quantum wells), 1D (quantum wires), 0D (quantum clusters) are at the molecular level to form bulk materials, which are structurally completely different from the morphological of 2D (nanosheets/nanoplatelets), 1D (nanowires/nanorods), and 0D (nanoparticles) as conventional materials which must be at least one dimension below 100 nm. However, such materials could be termed as low-dimension perovskite²⁷.

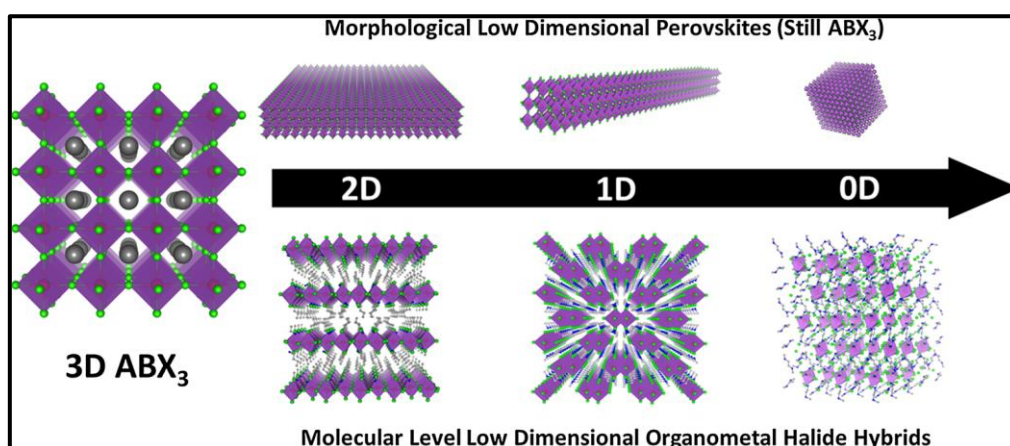


Figure 1.8 (a) 3D metal halide perovskites and perovskite with different dimensionalities at both morphological and molecular levels²⁷.

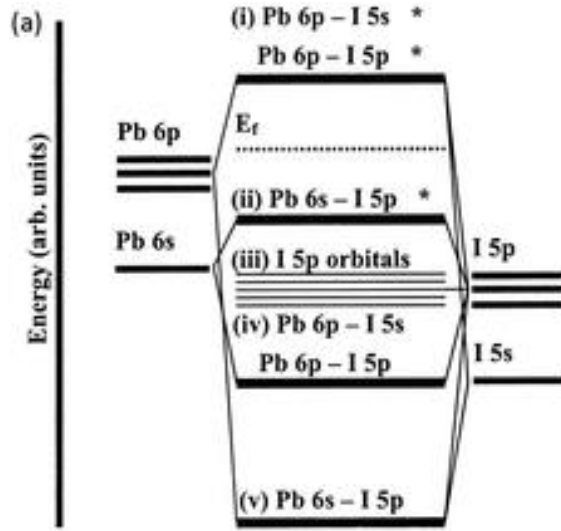


Figure 1.9 Band structure of MAPbI₃ perovskite²⁸.

The MHPs have very unique electronic properties which makes them so successful for PV and optoelectronic applications. The density functional theory (DFT) calculations have been widely employed to understand the nature of the electronic band structure of the most commonly studied type of perovskite (MAPbI₃)^{28,29}. DFT calculations showed that only B-site and X-site are responsible for the electronic band structures of a MHP (**Figure 1.9**). The nature of the interaction between Pb 6s, 6p and I 5p orbitals in the PbI₆ octahedra generates two bands with the electronic configuration of Pb: 5d¹⁰6s²6p⁰ and I: 5p⁶. Thus, the valence band maximum (VBM) consists of Pb 6s–I 5p interactions and the conduction band minimum (CBM) is formed of empty Pb 6p orbitals and/or from Pb 6p–I 5p interactions. The A⁺-site is located deeply (5 eV below Fermi level) in the VBM, thus it does not contribute directly to band structure. A⁺-site and its size (FA, MA, Cs, etc.) would affect the symmetry of perovskite lattice and chemical bonds in PbI₆ octahedra leading to a change in the bandgap. Also, the MAPbI₃ showed better optical absorption compared to one of the most popular PV materials such as GaAs. However, the DFT helped to explain the higher optical absorption of MAPbI₃ than GaAs, it was found that the density of states (DOS) derived from the Pb p orbital in the lower conduction band

(CB) of the halide perovskites is significantly higher than that of GaAs owing to a more dispersed s orbital from Ga and the strong s–p anti-bonding coupling in MAPbI₃ perovskite leads to small effective masses for both electrons and holes, which could make it efficient in solar cell application^{28,30}.

1.4 Losses and defects in hybrid metal halide perovskites

For a solar cell with a single junction absorber layer under 1.5 AM illumination (Figure 3a), there is a theoretical power conversion efficiency (PCE) efficiency limit which is known as Shockley-Queisser (SQ) limit. SQ limit considers all physical limitations except imperfections/defects³¹ (**Figure 1.10a**).

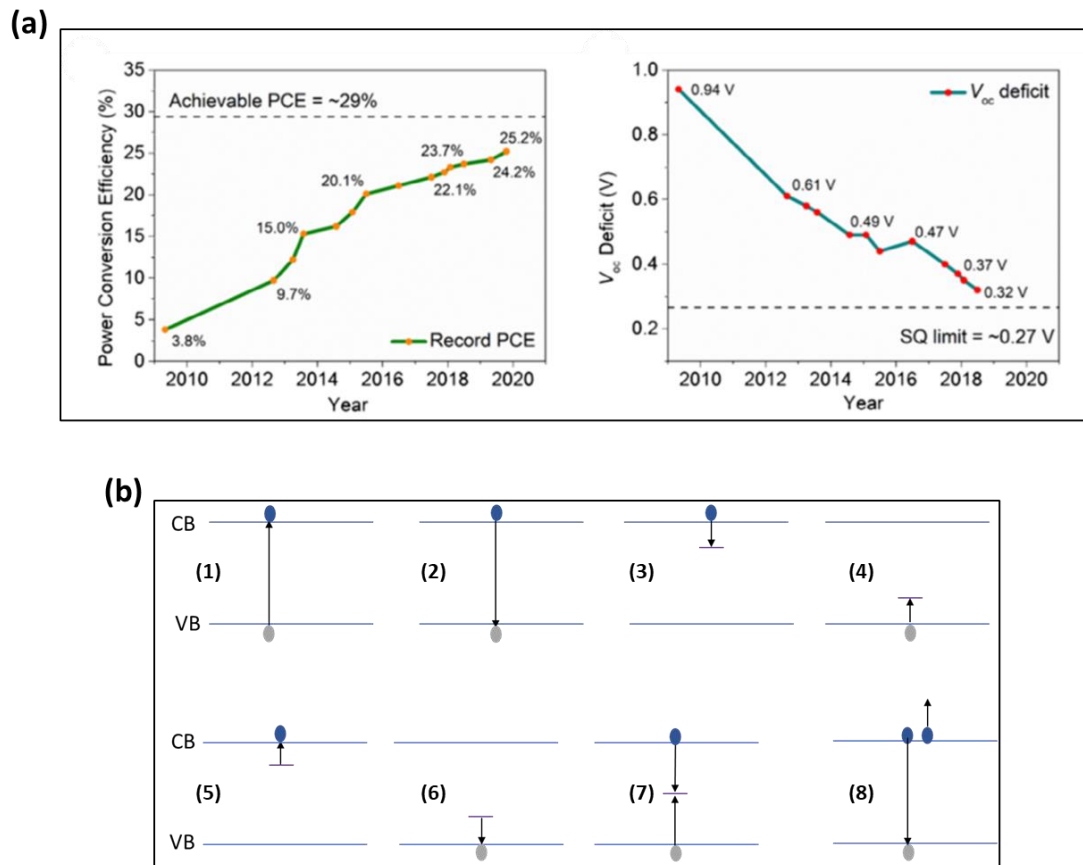


Figure 1.10 a) Recorded perovskite solar deceives and calculated $V_{oc,def}^{32}$, and (b) absorption (1) band to band radiative recombination (2), electron trapping (3), hole trapping (4), electron de-trapping (5), hole de-trapping (6), nonradiative recombination (via deep defects) (7) and Auger recombination (8)

MHPs are direct bandgap with high absorption coefficients (10^5 cm^{-1})³³ which allows it to efficiently harvest most of the incident photons in the 400-800 nm. After light absorption, the electrons are excited from the valance band (VB) to the conduction band (CB) which leads to a quasi-Fermi level of electrons (E_{Fn}) and holes (E_{Fp}) and the maximum V_{oc} of a device depends on the difference of E_{Fn} and E_{Fp} , which is known as quasi fermi level splitting (ΔE_F). After the excitation, the charge carriers will undergo recombination through different processes: (a) radiative recombination which is an intrinsic and unavoidable process (band-to-band recombination), (b) non-radiative recombination (Shockley-Read-Hall or trap assisted defects) which is not desirable, and (c) Auger recombination, which is not pronounced in perovskite solar cells at 1 Sun illumination due to the low carrier charge concentrations^{34,35} as shown **in Figure 1.10b**. To express the recombination dynamics, a rate law equation (1.1) which is a combination of monomolecular (first-order), bimolecular (second-order), and Auger (third-order) recombinations is used³⁶:

$$\frac{dn}{dt} = -k_1 n - k_2 n^2 - k_3 n^3 \quad (1.6)$$

where k_1 , k_2 and k_3 are monomolecular (first-order), bimolecular (second-order), and Auger (third-order) recombinations rate constants, respectively, and n is the photo-generated carrier density. The non-radiative recombination is deleterious for solar cell efficiency due to a reduction in the effective charge carrier density and lowers the E_F splitting, which will negatively affect the V_{oc} . The external photoluminescence quantum yield (PLQY) or and electroluminescence quantum efficiency (EQE_{EL}) can be used to calculate the voltage loss as well as the maximum V_{oc} of perovskite solar device and ΔE_F from the defect-mediated nonradiative recombination via these equations in the reciprocity relationship³³:

$$\left. \begin{aligned} V_{oc} &= \Delta E_F/q = V_{oc,sq} + k_B T/q \ln(PLQY) \\ V_{oc} &= \Delta E_F/q = V_{oc,sq} + k_B T/q \ln(EQE_{EL}) \end{aligned} \right\} \quad (1.7)$$

$$\left. \begin{aligned} V_{oc,sq} - V_{oc} &= \Delta V (V_{oc,non-rad}) = -k_B T/q \ln(PLQY) \\ &= -k_B T/q \ln(EQE_{EL}) \end{aligned} \right\} \quad (1.8)$$

Where $V_{oc,sq}$ is the radiative limit of the open-circuit voltage, k_B is the Boltzmann constant, T is the temperature, q is the elementary charge and $\Delta V (V_{oc,non-rad})$ is the voltage loss.

The presence of defects in a perovskite absorber material is deleterious for the optoelectronic properties, thus an in-depth understanding of defects is important before formulating mitigation strategies. In simple terms, defects are defined as an interruption from the ideal crystal lattice via forming a lattice irregularity or and the existence of impurities at the atomic scale in one or extended dimensions. Defects in a semiconductor are classified into four types of dimensional defects, namely as Zero-dimensional defects (point defects) and extended defects such as one-dimensional or line defects, two-dimensional defects (dislocation, surface, grain boundaries), and three-dimensional defects (voids, precipitates, cluster ... etc) as shown in **Figure 1.11**.

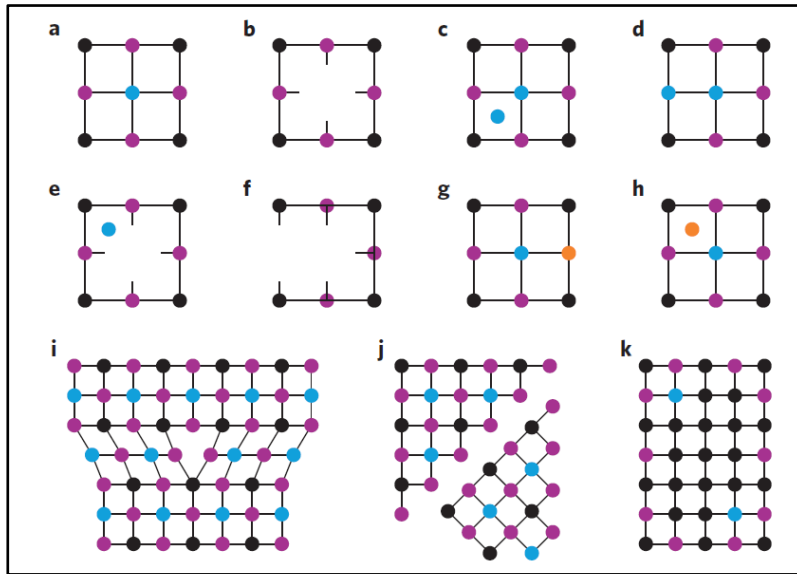


Figure 1.11 a-k) Defects type in semiconductor³⁶.

These defects could be formed due to many reasons such as synthesis process, growth process, impurity, annealing, post-annealing, stoichiometric and non-stoichiometric composition. In MHP, the point defects and extended defects (such as surface, grain boundaries) are considered as the main defects. The point defects are categorized as a vacancy (when the atom is missing from the lattice), interstitial (when the atom occupies a space between the atoms), anti-site (when the atom occupies a wrong site of the lattice), Frenkel (if the same atom missed from the original position and occupies a wrong place in the crystal) and Schottky (if the anion and cation missed) as shown in **Figure 1.11**. Thus, one can easily summarize the possible types of defects in perovskite material as **1) vacancy defect, 2) interstitial 3) anti-site, 4) Frenkel, 5) Schottky, 6) grain boundaries, 7) surface defect, 8) foreign atoms forming an impurity and substitution (such as mixed cations or mixed halide) and 9) precipitate defect** such as a lead cluster³⁷. **Figure 1.12** illustrates the most common defects in perovskite materials. From the density functional theory (DFT), it has been reported that there are 12 types of point defects possible in MAPbI_3 as $(\text{MA}_i, \text{Pb}_i, \text{and } \text{I}_i)$, $(\text{V}_{\text{MA}}, \text{V}_{\text{Pb}}, \text{and } \text{V}_{\text{I}})$ and $(\text{MA}_{\text{Pb}},$

M_{AI} , Pb_{MA} , Pb_I , I_{MA} , and I_{Pb}) as interstitials, vacancies and antisites, respectively³⁸. For state of art composition $FAPbI_3$, DFT showed that there possibility of several types of point defects such as interstitials (FA_i , Pb_i , I_i), vacancies (V_{FA} , V_{Pb} , V_I) antisites (FA_{Pb} , Pb_{FA} , FA_I , Pb_I , I_{FA} , I_{Pb})³⁹. **Table 1, Figure 1.13, and Table 2, Figure 1.14** show that the formation energy and energetics of the defect in $MAPbI_3$ and $FAPbI_3$, respectively.

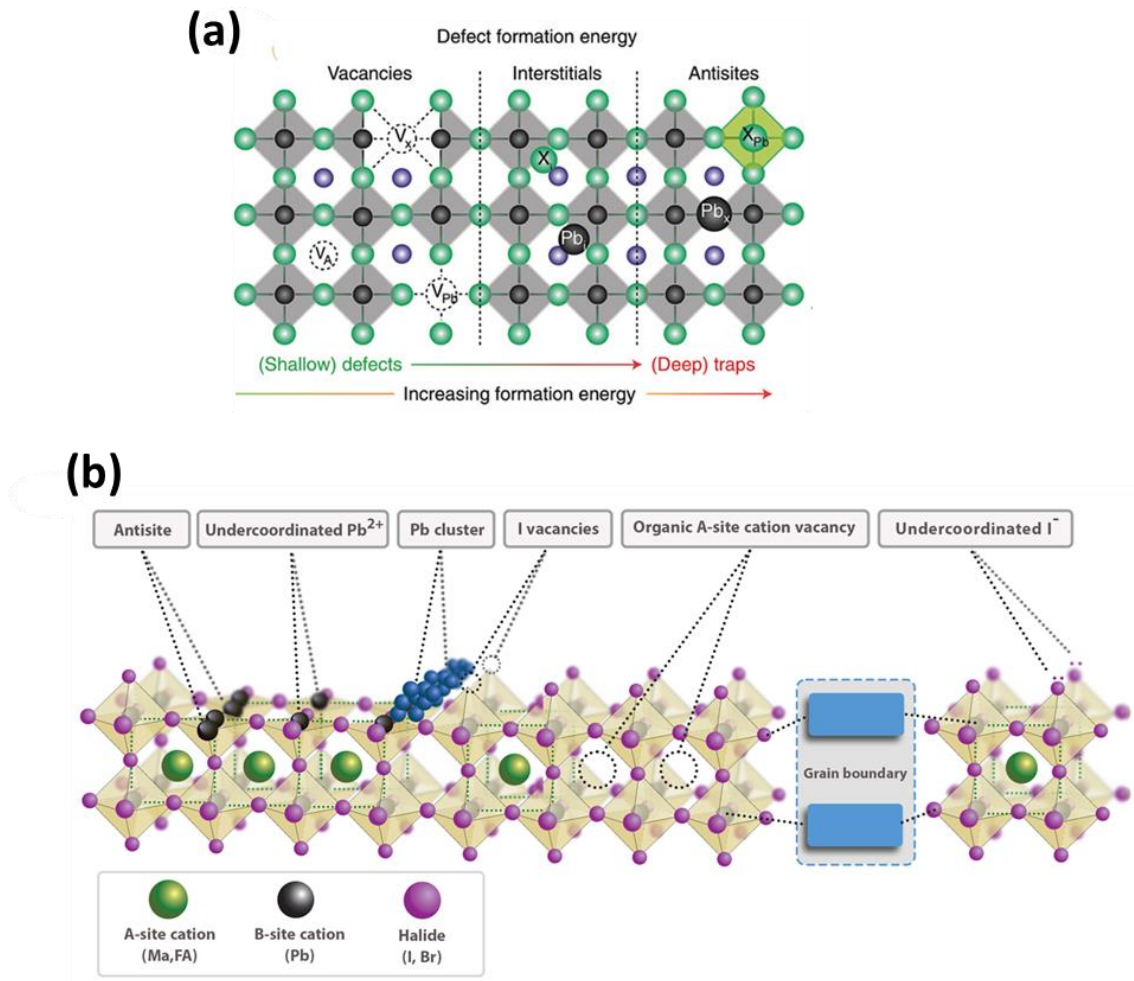


Figure 1.12 (a) Schematic representation of point defects in $MAPbI_3$ ⁴⁰ and (b) the most common surface defects in perovskite materials.

Table 1: Defect formation energies in eV of point defects for MAPbI₃ perovskite calculated Via DFT³⁸.

| Condition | I _i | MA _{Pb} | V _{MA} | V _{Pb} | I _{MA} | I _{Pb} | MA _i | Pb _{MA} | V _i | Pb _i | MA _i | Pb _i |
|----------------|----------------|------------------|-----------------|-----------------|-----------------|-----------------|-----------------|------------------|----------------|-----------------|-----------------|-----------------|
| Pb-rich/I-poor | 0.23 | 0.28 | 0.81 | 0.29 | 1.96 | 1.53 | 1.39 | 2.93 | 1.87 | 4.24 | 3.31 | 5.54 |
| Moderate | 0.83 | 1.15 | 1.28 | 1.62 | 3.01 | 3.45 | 0.93 | 2.51 | 1.27 | 2.91 | 2.25 | 3.62 |
| Pb-poor/I-rich | 1.42 | 1.47 | 2.01 | 2.68 | 4.34 | 5.10 | 0.20 | 1.74 | 0.67 | 1.85 | 0.93 | 1.97 |

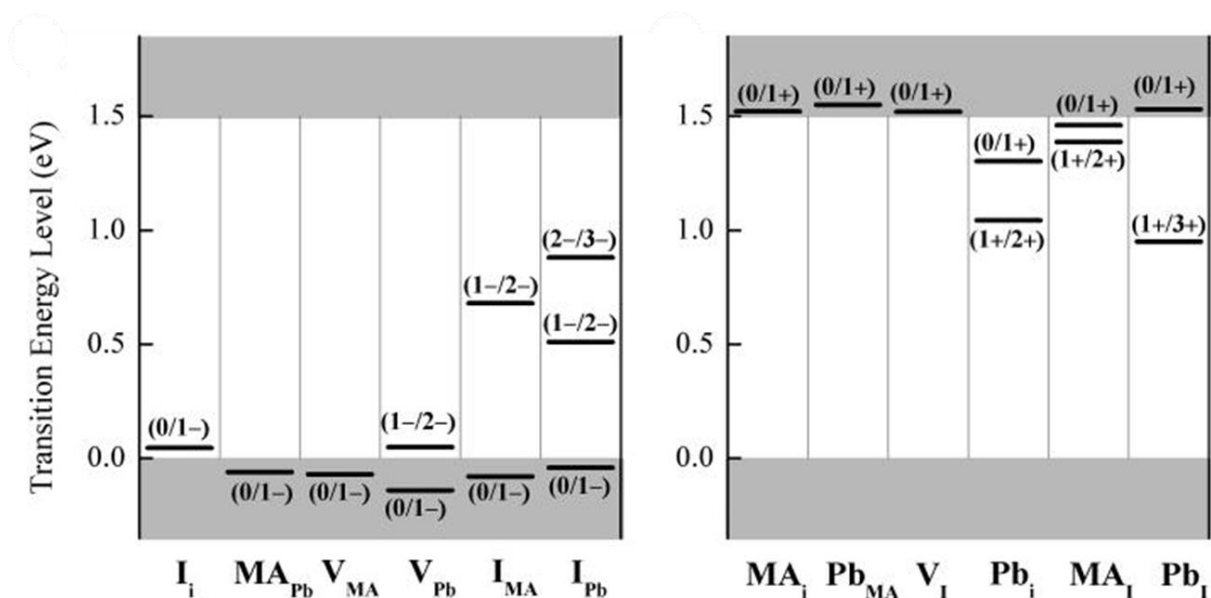


Figure 1.13 (a) The transition energy levels of (a) intrinsic acceptors and (b) intrinsic donors in MAPbI₃⁴¹.

Table 2: Defect formation energies in eV of point defects for FAPbI₃ perovskite calculated Via DFT³⁹.

| Condition | I _i | FA _{Pb} | V _{FA} | V _{Pb} | I _{FA} | I _{Pb} | FA _i | Pb _{FA} | V _I | Pb _i | FA _I | Pb _I |
|-----------|----------------|------------------|-----------------|-----------------|-----------------|-----------------|-----------------|------------------|----------------|-----------------|-----------------|-----------------|
| I-poor | 0.60 | 1.02 | 0.14 | 0.86 | 0.34 | 0.72 | 2.36 | 2.28 | 1.69 | 3.38 | 2.30 | 4.63 |
| Pb-rich | 1.60 | 2.08 | 1.09 | 2.97 | 2.45 | 3.89 | 1.31 | 1.22 | 0.63 | 1.27 | 0.19 | 1.46 |
| Moderate | 1.13 | 1.61 | 0.54 | 1.95 | 1.37 | 2.34 | 1.86 | 1.69 | 1.16 | 2.29 | 1.27 | 3.01 |

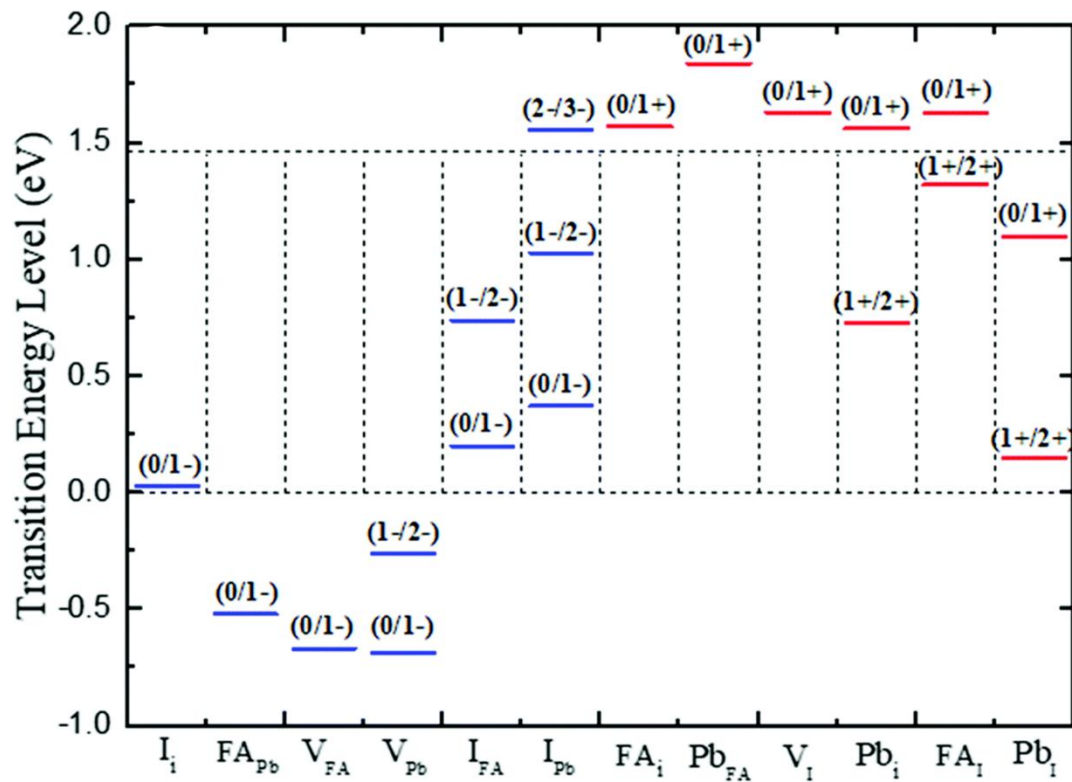


Figure 1.14 (a) The transition energy levels of intrinsic defects in FAPbI₃³⁹.

The majority of the deleterious defects which form deep traps have high formation energy, thus they seldom form. Whereas, the commonly formed defects which have low formation energy are mostly shallow and hence, they have a negligible contribution to non-radiative recombination, possibly a reason behind the long lifetime (hundreds of ns to several μ s), and long diffusion lengths (hundreds of nm to several μ m)³⁷. However, as these MHP have are mixed conductors, i.e. both the ionic and electronic conductivity, thus and these shallow traps can assist the ion migration in the bulk of the perovskite absorber as well as to the interfaces, especially in the presence of electric field⁴². Such ion migration is detrimental to the performance of perovskite solar cells also considered as one major reason behind the hysteresis effect and un-stabilized MPP in devices⁴³. Thus, to obtain a highly efficient and stable perovskite solar device, it is not only enough to suppress the deep level traps, but also it is critical to passivate the shallow traps which cause the ion migration.

1.5 Mitigation strategy of defects

In the previous section, we show the nature of defects and their role in performance and stability. The ionic nature of the defects in the MHP allows us to employ different strategies based on non-covalent interaction to passivate these bulk and interfacial defects and thus enhancing the performance and long-term stability. In this section, some of the key strategies of defect mitigation will be discussed.

1.5.1 Salts and low dimensional perovskites

Organic/inorganic salts have been reported as effective defect passivators. The passivator material as the ions can interact and passivate the charged defects. Monovalent cations such as Na^+ , K^+ , Rb^+ , Cu^+ , Ag^+ showed that indeed they were capable and suitable materials for passivation⁴⁴. Organic ammonium salts have functional groups of ammonium ($-\text{NH}_3^+$) and were shown a good candidate to effectively passivate negatively charged defects through electrostatic interactions including ionic bonding and hydrogen bonding. Some of the common organic ammonium functionalities used for passivation are butylammonium (BA^+)⁴⁵, octylammonium (OA^+)⁴⁵, and phenylethylammonium (PEA^+)⁴⁶. Apart from these commonly used salts, our group reported that a new tailored amphiphilic molecule, 4-*tert*-butylbenzylammonium iodide (tBBAI) which was highly efficient in surface defect passivation which enabled a champion device a PCE of 23.5% PSCs,⁴⁷. However, some of the organic ammonium salts can react with lead halide and can form a layered structure called Low-dimensional (low-D) perovskites. In the case of the perovskite bulk engineering, it is shown that some organic molecules formed a 2D perovskite layer within the grain boundaries of perovskite such as PEA^+ (PEA_2PbI_4) and when passivated the interface of perovskite/HTL formed bilayer 2D/3D structure⁴⁸. Long chain alkylammonium halide salts such as OA^+ etc. were found to be very interesting for surface/interface passivation. They can passivate interface defects and makes a humidity barrier due to the hydrophobicity feature which results in an enhancement of perovskite stability as well as improving the contact between perovskite with the interface of HTL^{45,49}. In addition, zwitterions molecules such as L- α -phosphatidylcholine, choline chloride, and choline iodide have shown both abilities to passivate the negative and a positive charged functional group and have been used⁵⁰. Halide engineering also is important such as I^- , Cl^- , Br^- , F^- , SCN^- and formates⁵¹ are the most studied as anion passivators⁵². For

example, sodium fluoride (NaF) was used as an anionic passivator to form a bond with Pb^{2+} as well as to passivate the X-site and A-site vacancies. Due to the strongest electronegativity of F^- , the strongest hydrogen bond formed stabilized the surface of perovskite⁵³.

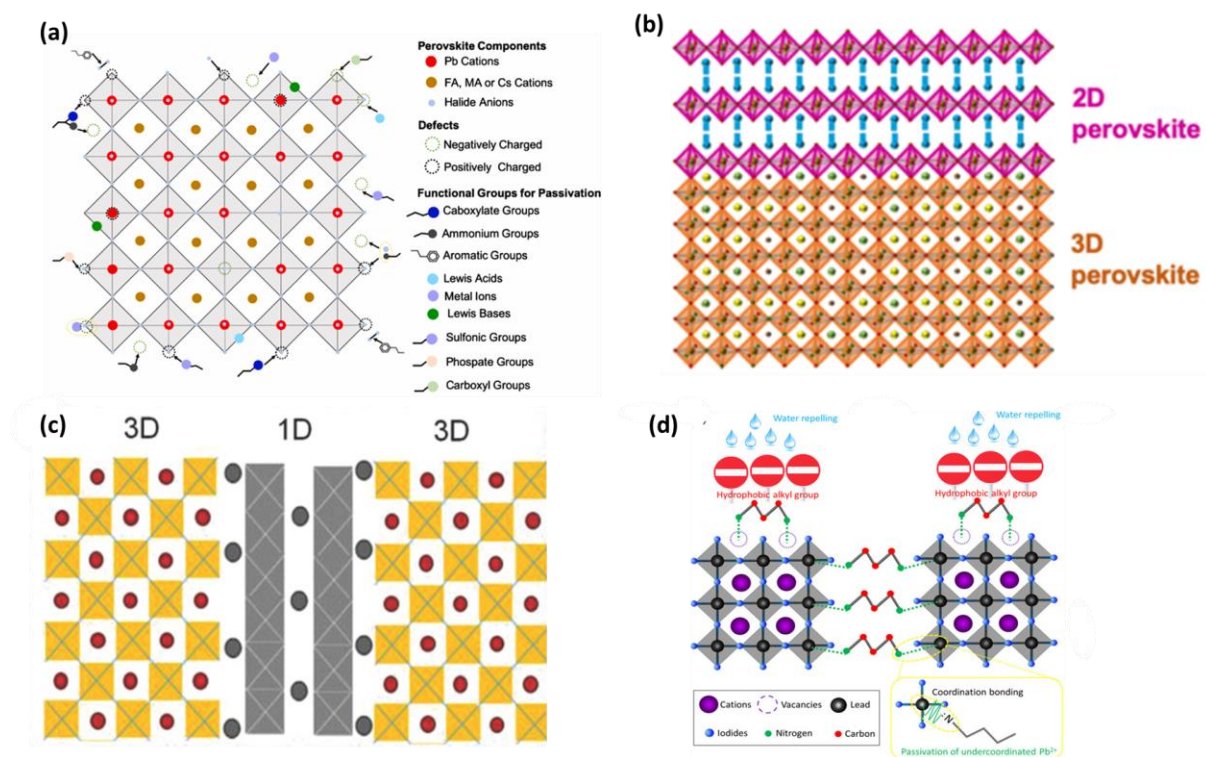


Figure 1.15 (a) An illustration of passivation mechanisms⁵⁴, (b) Schematic illustration of the 2D/3D perovskite interface⁵⁵, (c) Schematic illustration of the 1D/3D perovskite, and (d) illustration of Alkylammonium (BAA) with perovskite⁵⁶.

1.5.2 Lewis acid

Lewis acids have a good capability to accept a pair of electrons to passivate negative defects such as undercoordinated I^- , as well as anti-site PbI_3^- . Lewis acid such as fullerene and their derivatives have proven as the most effective defect passivator because they are observed to be having excellent electron-accepting properties^{57,58}. The passivation of undercoordinated halide ions by iodopentafluorobenzene via halogen bonding was reported⁵⁹.

It was found that the strong electronegative of fluorine atoms which are withdrawing the electron density out of the aromatic ring of iodopentafluorobenzene reduced the electron density of iodine on the aromatic ring, $-C-I$. The electron-deficient nature of this iodine makes it act as an electron acceptor, Lewis acid, for strong halogen bonding with an undercoordinated halide or $Pb-X$ antisite defect. The production of this $-C-I\cdots X$ bond enhances the charge transfer at the perovskite/HTM interface and increases the carrier lifetime by lowering the possibility of charge trapping at electron-rich surface defects. Also, 2-aminoterephthalic acid was found to work as an additive to stop I^- ion migration by forming high coordination with I^- ions in the perovskite⁶⁰. The introduction of hydroxylamine hydrochloride (HaHc) was found to enhance the quality, optoelectronic properties, and stability of perovskite films. The Cl^- ions from HaHc can improve the crystallization kinetic of perovskite and reduce the grain boundary. Also, the hydroxyl (OH) groups in HaHc can form a strong H bond with I^- in the perovskite, suppressing the possible degradation of the perovskite film and resulted in stability improvement⁶¹.

1.5.3 Lewis base

Lewis bases are a good candidate for donating a pair of non-bonding electrons to coordinate the positively charged defects. Several Lewis bases containing heteroatoms such as O, N, P, or S with lone electron pairs, which can favorably interact with undercoordinated Pb^{2+} ions, as well as Pb clusters⁶². As for the first report using a Lewis base surface treatment, a thin layer of thiophene and pyridine was deposited on top of the perovskite surface. The strong coordinate bonding between the sulfur atom in thiophene or nitrogen atom in pyridine with under-coordinated Pb^{2+} can effectively passivate the Pb^{2+} point defects. Due to the Lewis base treatment, a remarkable improvement in the lifetime and improved stability of the perovskite films. Poly(4-vinylpyridine) (PVP) functionalized with pyridine was reported as a passivation

agent that could improve the performance of the the PSCs⁶³. Yang and co-worker showed that the molecular configuration of the Lewis base can also play an important role. They reported a set of tailored small molecules, namely, theophylline, caffeine, and theobromine, interacting with the surface defects. It was found that when N-H and C=O were in an optimal configuration in the molecule, hydrogen-bond formation between N-H and I (iodine) assisted the primary C=O binding with the anti-site Pb defect to maximize surface-defect binding. A stabilized PCE of 22.6% of PSC was demonstrated with theophylline treatment⁶⁴.

1.6 Conclusion

Over the years, there has been drastic improvement in the performance and stability of PSCs. One of the key reasons for such improvement is the development of defect passivation strategies. In this chapter, we discuss different kinds of defects and their effects on the performance of perovskite solar cells along with mitigation strategies. Most of the commonly formed defects in the perovskites are shallow defects as they have low formation energy compared to the deep trap states that have high formation energy. The defects are not only responsible for detrimental phenomena but also contribute to phenomena such as hysteresis and ion migration, which can compromise the device stability. Different defect passivation strategies have been developed which include organic/inorganic salts based on electrostatic/van der Waals interactions and Lewis acid-base chemistry-based non-covalent interactions. The facile and rational designing of the defect passivation material has the potential to stimulate other successful developments and unlock the full potential of the PSCs in the future.

1.7 Reference

- 1 B. J. van Ruijven, E. De Cian and I. Sue Wing, *Nat. Commun.*, 2019, **10**, 1–12.
- 2 *World Energy Outlook 2020*, <https://www.iea.org/reports/world-energy-outlook-2020>, .
- 3 T. Watari, B. C. McLellan, D. Giurco, E. Dominish, E. Yamasue and K. Nansai, *Resour. Conserv. Recycl.*, 2019, **148**, 91–103.
- 4 S. Bajracharya, *Microbial electrosynthesis of ethanol*, 2016.
- 5 R. Perez and M. Perez, *Int. Energy Agency SHC Program. Sol. Updat.*, 2009, **50**, 4–6.
- 6 B. P. Rappaport, *The Photovoltaic Effect and its Utilization**, 1959, vol. 3.
- 7 C. E. Fritts, *J. Franklin Inst.*, 1885, **119**, 221–232.
- 8 D. M. Chapin, C. S. Fuller and G. L. Pearson, *J. Appl. Phys.*, 1954, **25**, 676–677.
- 9 N. E. B. Cower, *Silicon-based photovoltaic solar cells*, Woodhead Publishing Limited, 2012.
- 10 A. Ur Rehman and S. H. Lee, *Sci. World J.*, , DOI:10.1155/2013/470347.
- 11 M. A. Green, E. D. Dunlop, J. Hohl-Ebinger, M. Yoshita, N. Kopidakis and X. Hao, *Prog. Photovoltaics Res. Appl.*, 2020, **28**, 629–638.
- 12 J. S. Park, S. Kim, Z. Xie and A. Walsh, *Nat. Rev. Mater.*, 2018, **3**, 194–210.
- 13 D. Zhou, T. Zhou, Y. Tian, X. Zhu and Y. Tu, *J. Nanomater.*, , DOI:10.1155/2018/8148072.
- 14 W. L. Waltz, *Radiat. Phys. Chem.*, 1984, **23**, 491.
- 15 J. Simpura, *Nord. Stud. Alcohol Drugs*, 1998, **15**, 131–132.
- 16 Y. Cao, Y. Liu, S. M. Zakeeruddin, A. Hagfeldt and M. Grätzel, *Joule*, 2018, **2**, 1108–1117.
- 17 N. Chart, <https://www.nrel.gov/pv/cell-efficiency.html>, .
- 18 A. Kojima, K. Teshima, Y. Shirai and T. Miyasaka, *J. Am. Chem. Soc.*, 2009, **131**, 6050–6051.
- 19 H. S. Kim, C. R. Lee, J. H. Im, K. B. Lee, T. Moehl, A. Marchioro, S. J. Moon, R. Humphry-Baker, J. H. Yum, J. E. Moser, M. Grätzel and N. G. Park, *Sci. Rep.*, 2012, **2**, 1–7.
- 20 G. H. Kim and D. S. Kim, *Joule*, 2021, **5**, 1033–1035.
- 21 P. Qin, A. L. Domanski, A. K. Chandiran, R. Berger, H. J. Butt, M. I. Dar, T. Moehl, N. Tetreault, P. Gao, S. Ahmad, M. K. Nazeeruddin and M. Grätzel, *Nanoscale*, 2014,

- 6, 1508–1514.
- 22 L. Liu, A. Mei, X. Li, H. Han, Y. Dkhissi, A. D. Scully, R. A. Caruso, Y. B. Cheng, I. Jeong, J. Lee, M. J. Ko, K. Yong, B. S. Richards, T. L. Kelly, N. Pellet, M. Levi, S. Turri, M. Levi and S. Turri, .
- 23 L. Dou, A. B. Wong, Y. Yu, M. Lai, N. Kornienko, S. W. Eaton, A. Fu, C. G. Bischak, J. Ma, T. Ding, N. S. Ginsberg, L. W. Wang, A. P. Alivisatos and P. Yang, *Science* (80-.), 2015, **349**, 1518–1521.
- 24 F. S. Galasso, *Structure, Properties and Preparation of Perovskite-Type Compounds*, 1st Editio., 1969.
- 25 C. C. Stoumpos, D. H. Cao, D. J. Clark, J. Young, J. M. Rondinelli, J. I. Jang, J. T. Hupp and M. G. Kanatzidis, *Chem. Mater.*, 2016, **28**, 2852–2867.
- 26 L. Harlow, N. Herron, L. Thorn, Y. Wang, E. I. Pont and R. September, 1991, 2328–2330.
- 27 C. Zhou, H. Lin, Q. He, L. Xu, M. Worku, M. Chaaban, S. Lee, X. Shi, M. H. Du and B. Ma, *Mater. Sci. Eng. R Reports*, 2019, **137**, 38–65.
- 28 T. Umebayashi, K. Asai, T. Umebayashi, K. Asai, T. Kondo, T. Kondo and A. Nakao, *Phys. Rev. B - Condens. Matter Mater. Phys.*, 2003, **67**, 2–7.
- 29 S. Colella, E. Mosconi, P. Fedeli, A. Listorti, A. Rizzo, F. Gazza, F. Orlandi, P. Ferro, T. Besagni, G. Calestani, F. De Angelis, R. Mosca and G. Gigli, *Mater. Res. Soc. Symp. Proc.*, , DOI:10.1557/opl.2014.898.
- 30 E. Mosconi, P. Umari and F. De Angelis, *Phys. Chem. Chem. Phys.*, 2016, **18**, 27158–27164.
- 31 W. Shockley and H. J. Queisser, *J. Appl. Phys.*, 1961, **32**, 510–519.
- 32 P. Chen, Y. Bai and L. Wang, *Small Struct.*, 2021, **2**, 2000050.
- 33 S. D. Stranks, R. L. Z. Hoyer, D. Di, R. H. Friend and F. Deschler, *Adv. Mater.*, , DOI:10.1002/adma.201803336.
- 34 W. Tress, N. Marinova, O. Inganäs, M. K. Nazeeruddin, S. M. Zakeeruddin and M. Graetzel, *Adv. Energy Mater.*, 2015, **5**, 1–6.
- 35 L. M. Pazos-Outón, T. P. Xiao and E. Yablonovitch, *J. Phys. Chem. Lett.*, 2018, **9**, 1703–1711.
- 36 J. M. Ball and A. Petrozza, *Nat. Energy*, 2016, **1**, 16149.
- 37 B. Chen, P. N. Rudd, S. Yang, Y. Yuan and J. Huang, *Chem. Soc. Rev.*, 2019, **48**, 3842–3867.
- 38 H. Uratani and K. Yamashita, *J. Phys. Chem. Lett.*, 2017, **8**, 742–746.

- 39 N. Liu and C. Y. Yam, *Phys. Chem. Chem. Phys.*, 2018, **20**, 6800–6804.
- 40 L. K. Ono, S. Liu and Y. Qi, *Angew. Chemie - Int. Ed.*, 2020, **59**, 6676–6698.
- 41 W. J. Yin, T. Shi and Y. Yan, *Appl. Phys. Lett.*, 2014, **104**, 3–6.
- 42 H. Xie, Z. Wang, Z. Chen, C. Pereyra, M. Pols, K. Gałkowski, M. Anaya, S. Fu, X. Jia, P. Tang, D. J. Kubicki, A. Agarwalla, H. S. Kim, D. Prochowicz, X. Borrisé, M. Bonn, C. Bao, X. Sun, S. M. Zakeeruddin, L. Emsley, J. Arbiol, F. Gao, F. Fu, H. I. Wang, K. J. Tielrooij, S. D. Stranks, S. Tao, M. Grätzel, A. Hagfeldt and M. Lira-Cantu, *Joule*, 2021, **5**, 1246–1266.
- 43 E. Bi, Z. Song, C. Li, Z. Wu and Y. Yan, *Trends Chem.*, 2021, **3**, 575–588.
- 44 M. Abdi-Jalebi, M. Pazoki, B. Philippe, M. I. Dar, M. Alsari, A. Sadhanala, G. Divitini, R. Imani, S. Lilliu, J. Kullgren, H. Rensmo, M. Grätzel and R. H. Friend, *ACS Nano*, 2018, **12**, 7301–7311.
- 45 H. Kim, S. U. Lee, D. Y. Lee, M. J. Paik, H. Na, J. Lee and S. Il Seok, *Adv. Energy Mater.*, 2019, **9**, 1–8.
- 46 Q. Jiang, Y. Zhao, X. Zhang, X. Yang, Y. Chen, Z. Chu, Q. Ye, X. Li, Z. Yin and J. You, *Nat. Photonics*, 2019, **13**, 460–466.
- 47 H. Zhu, Y. Liu, F. T. Eickemeyer, L. Pan, D. Ren, M. A. Ruiz-Preciado, B. Carlsen, B. Yang, X. Dong, Z. Wang, H. Liu, S. Wang, S. M. Zakeeruddin, A. Hagfeldt, M. I. Dar, X. Li and M. Grätzel, *Adv. Mater.*, 2020, **32**, 1–8.
- 48 P. Chen, Y. Bai, S. Wang, M. Lyu, J. H. Yun and L. Wang, *Adv. Funct. Mater.*, 2018, **28**, 1–10.
- 49 M. Jung, T. J. Shin, J. Seo, G. Kim and S. Il Seok, *Energy Environ. Sci.*, 2018, **11**, 2188–2197.
- 50 X. Zheng, B. Chen, J. Dai, Y. Fang, Y. Bai, Y. Lin, H. Wei, X. C. Zeng and J. Huang, *Nat. Energy*, 2017, **2**, 1–9.
- 51 J. Jeong, M. Kim, J. Seo, H. Lu, P. Ahlawat, A. Mishra, Y. Yang, M. A. Hope, F. T. Eickemeyer, M. Kim, Y. J. Yoon, I. W. Choi, B. P. Darwich, S. J. Choi, Y. Jo, J. H. Lee, B. Walker, S. M. Zakeeruddin, L. Emsley, U. Rothlisberger, A. Hagfeldt, D. S. Kim, M. Grätzel and J. Y. Kim, *Nature*, 2021, **592**, 381–385.
- 52 D. Luo, W. Yang, Z. Wang, A. Sadhanala, Q. Hu, R. Su, R. Shivanna, G. F. Trindade, J. F. Watts, Z. Xu, T. Liu, K. Chen, F. Ye, P. Wu, L. Zhao, J. Wu, Y. Tu, Y. Zhang, X. Yang, W. Zhang, R. H. Friend, Q. Gong, H. J. Snaith and R. Zhu, *Science (80-.)*, 2018, **360**, 1442–1446.
- 53 N. Li, S. Tao, Y. Chen, X. Niu, C. K. Onwudinanti, C. Hu, Z. Qiu, Z. Xu, G. Zheng, L.

- Wang, Y. Zhang, L. Li, H. Liu, Y. Lun, J. Hong, X. Wang, Y. Liu, H. Xie, Y. Gao, Y. Bai, S. Yang, G. Brocks, Q. Chen and H. Zhou, *Nat. Energy*, 2019, **4**, 408–415.
- 54 D. Luo, R. Su, W. Zhang, Q. Gong and R. Zhu, *Nat. Rev. Mater.*, 2020, **5**, 44–60.
- 55 A. A. Sutanto, P. Caprioglio, N. Drigo, Y. J. Hofstetter, I. Garcia-Benito, V. I. E. Queloz, D. Neher, M. K. Nazeeruddin, M. Stollerfoht, Y. Vaynzof and G. Grancini, *Chem*, 2021, **7**, 1903–1916.
- 56 J. Ye, M. M. Byranvand, C. O. Martínez, R. L. Z. Hoye, M. Saliba and L. Polavarapu, *Angew. Chemie - Int. Ed.*, 2021, 2–27.
- 57 J. Xu, A. Buin, A. H. Ip, W. Li, O. Voznyy, R. Comin, M. Yuan, S. Jeon, Z. Ning, J. J. McDowell, P. Kanjanaboos, J. P. Sun, X. Lan, L. N. Quan, D. H. Kim, I. G. Hill, P. Maksymovych and E. H. Sargent, *Nat. Commun.*, 2015, **6**, 1–8.
- 58 Y. Shao, Z. Xiao, C. Bi, Y. Yuan and J. Huang, *Nat. Commun.*, 2014, **5**, 1–7.
- 59 A. Abate, M. Saliba, D. J. Hollman, S. D. Stranks, K. Wojciechowski, R. Avolio, G. Grancini, A. Petrozza and H. J. Snaith, *Nano Lett.*, 2014, **14**, 3247–3254.
- 60 Z. Liu, F. Cao, M. Wang, M. Wang and L. Li, *Angew. Chemie - Int. Ed.*, 2020, **59**, 4161–4167.
- 61 H. Jiang, Z. Yan, H. Zhao, S. Yuan, Z. Yang, J. Li, B. Liu, T. Niu, J. Feng, Q. Wang, D. Wang, H. Yang, Z. Liu and S. F. Liu, *ACS Appl. Energy Mater.*, 2018, **1**, 900–909.
- 62 L. Su, Y. Xiao, L. Lu, G. Han and M. Zhu, *Org. Electron.*, 2020, **77**, 9815–9821.
- 63 M. Yavari, M. Mazloum-Ardakani, S. Gholipour, M. M. Tavakoli, N. Taghavinia, A. Hagfeldt and W. Tress, *ACS Omega*, 2018, **3**, 5038–5043.
- 64 R. Wang, J. Xue, K. L. Wang, Z. K. Wang, Y. Luo, D. Fenning, G. Xu, S. Nuryyeva, T. Huang, Y. Zhao, J. L. Yang, J. Zhu, M. Wang, S. Tan, I. Yavuz, K. N. Houk and Y. Yang, *Science (80-.)*, 2019, **366**, 1509–1513.

Chapter 2.

Perovskite Solar Cells Yielding Reproducible Photovoltage of 1.20 V

*This work has been published: E. A. Alharbi, M. I. Dar, N. Arora, M. H. Alotaibi, Y. A. Alzhrani, P. Yadav, W. Tress, A. Alyamani, A. Albadri, S. M. Zakeeruddin and M. Grätzel, Research, 2019, **2019**, 1–9.*

2.1 Introduction

Over the past few years, perovskite solar cells (PSCs) have attracted great attention in the applied and theoretical research fields [1]. The appealing photophysical properties, such as small exciton binding energy, tunable bandgap, high absorption coefficient, relatively high carrier mobility, and diffusivity, and tolerance to defects, broaden the application horizon of perovskites from photovoltaics to light-emitting diodes and lasing [2–6]. Since PSCs were first introduced by the Miyasaka group in 2009, the power conversion efficiency (PCE) has been improved from 3.8% to over 23% using solution-based deposition methods [2,7]. However, these methods can generate films exhibiting pinholes and defects, which are detrimental to the device performance due to the occurrence of parasitic charge carrier recombination under operational conditions [8,9]. Therefore, to develop high-efficiency PSCs using solution-based approaches, one of the challenges is to achieve rational control over the quality of the absorber layer [10,11]. Recent reports on PSCs have shown that nonradiative charge carrier recombination or charge injection at the interfaces to charge transport layers limits the open-circuit voltage (V_{oc}) [12–15]. The role of grain boundaries acting as recombination centers is under debate as such processes depend on the processing conditions and composition of the perovskite layer [16–20]. As it has become important to suppress the nonradiative recombination losses occurring at the interfaces or throughout the bulk of the perovskite film [21], many efforts have been devoted towards passivating the defects, which consequently retard the trap-assisted nonradiative charge carrier recombination. For example, a series of

dialkylammonium and phenyltrimethylammonium halides were successfully explored to passivate the interfaces and grain boundaries resulting in a much-improved PCE [22–24]. In a similar manner, the guanidinium (Gua) cation (CH_6N_3^+) was employed for the passivation of nonradiative recombination centers at $\text{CH}_3\text{NH}_3\text{PbI}_3$ grain boundaries enhancing the V_{oc} up to 1.07 V [25–27]. The Gua cation may also act as a crosslinker between the neighboring perovskite grains in the film [28]. It is worth emphasizing that the Gua cation was mainly investigated as an additive to $\text{CH}_3\text{NH}_3\text{PbI}_3$ based PSCs displaying moderate power conversion efficiencies. In addition to forming mixed-cation phases exhibiting relatively large bandgap, Gua cation can mix with MA and/or FA cations in the 3D perovskite lattice [29, 30] and consequently influence the excitonic and structural properties of the host phase remarkably. However, its influence on the bandgap, film quality, and performance of multication-based PSCs has not been explored so far.

In this article, we illustrate the effect of guanidinium iodide (GuaI) on the photophysical properties of mixed-cation and mixed-halide perovskite films. Thorough analyses based on scanning electron microscopy and emission studies were carried out to investigate the effect of GuaI addition on the morphology and emission of the perovskite material. Furthermore, electroluminescence and time-resolved photoluminescence studies were performed, respectively, to investigate the fully assembled devices and the charge carrier recombination occurring within the perovskite films. The operational stability carried out at a maximum power point under continuous full-sun illumination for 200 h showed that the PSCs containing Gua cations are as stable as control PSCs. In addition to providing new physical insights, we demonstrate for the first time robust stability for Gua based PSCs which are >20% efficient and yield photovoltage as high as 1.20 V.

2.2 Results

As a reference PSC, we used the mixed-halide and mixed-cation formulation “ $\text{Cs}_{0.05}(\text{MA}_{0.17}\text{FA}_{0.83})_{0.95}\text{Pb}(\text{I}_{0.83}\text{Br}_{0.17})_3$ ” (abbreviated as Cs_5Pb). By adding $x = 5\%$ volume ratio of 1.5 M GuaI in DMSO, we prepared $\text{Cs}_5\text{Pb}\cdot 5\text{GuaI}$ perovskite films [31].

2.2.1 Steady-State and Time-Resolved Photoluminescence. To unravel the impact of GuaI on the emission properties of the absorber layer, steady-state photoluminescence (PL) was measured for $\text{Cs}_5\text{Pb}\cdot 5\text{GuaI}$ films (Figure 2.1(A)). Upon addition of 5% GuaI, a slight red shift from 757 to 766 nm in the peak position indicates that incorporation of GuaI in the perovskite lattice decreases the band gap slightly. In addition, the emission intensity enhanced dramatically with the incorporation of GuaI in Cs_5Pb precursor solution indicating a decrease in the nonradiative recombination.

Variation in the steady-state PL intensity apparently demonstrates that the level of defects promoting nonradiative carrier recombination in the perovskite film decreases upon introducing GuaI into the precursor solution. We employed time-resolved photoluminescence (TRPL) to further characterize the perovskite films quantitatively (Figure 2.1(B)). While exciting the films from the perovskite side using 408 nm photons, we studied the charge carrier dynamics occurring within the reference and $\text{Cs}_5\text{Pb}\cdot x\text{GuaI}$ perovskite films. Figure 2.1(B) shows that the incorporation of 5% GuaI dramatically increases the charge carrier lifetime. Charge carrier life time of 215 ns and 627 ns was estimated, respectively, for the Cs_5Pb , and $\text{Cs}_5\text{Pb}\cdot 0.05\text{GuaI}$ films. The initial fast decay is strongly reduced in the $\text{Cs}_5\text{Pb}\cdot 0.05\text{GuaI}$ film, consistent with the high PL intensity [32].

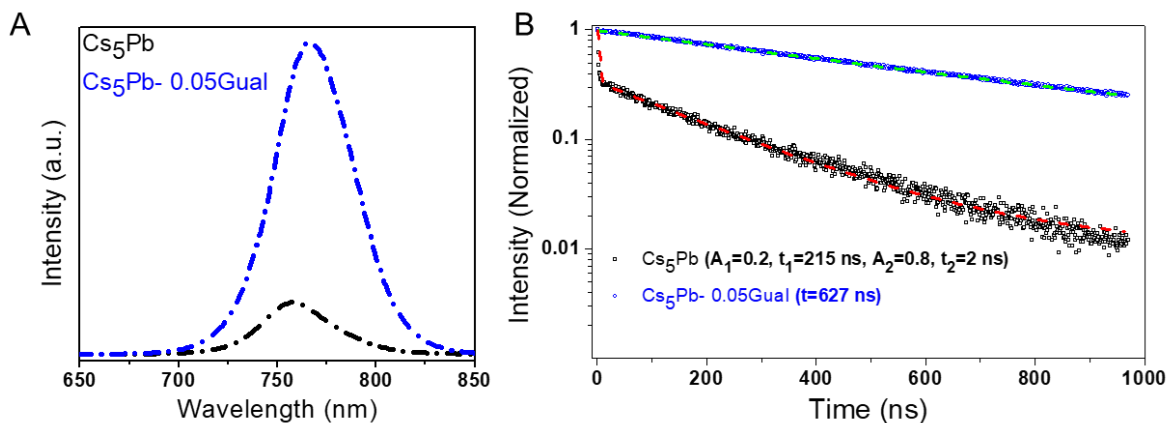


Figure. 2.1 Photoluminescence studies of pure and GuaI containing perovskite films. (A), steady-state photoluminescence (B), time-resolved photoluminescence spectra; solid lines present the fitting curves obtained using a mono- or a bi-exponential decay model.

2.2.2 Morphological and Photovoltaic Characterization. Furthermore, the surface morphology of perovskite films was characterized via scanning electron microscopy (SEM) (Figure 2.2). Ostensibly, top view (Figures 2.2(A) and 2.2(B)) and cross-sectional (Figures 2.2(C) and 2.2(D)) SEM micrographs acquired from Cs₅Pb, Cs₅Pb.0.05GuaI perovskite films and the devices based on them confirm that the morphology of absorber layers is not affected by the addition of GuaI. The effect of GuaI incorporation on the photovoltaic performance is further examined in a device configuration of FTO/c-TiO₂/m-TiO₂/perovskite/spiro-OMeTAD/Au (for more details see Methods). Figure 2.3(A) depicts the *J-V* curves of the devices with 5% GuaI content in comparison to the reference Cs₅Pb device, and the corresponding photovoltaic parameters are summarized in Table 2.1. For the Cs₅Pb device, the highest PCE obtained is 20.03% with an open-circuit voltage (V_{OC}) of 1.13 V, a short-circuit current density (J_{SC}) of 23 mA cm⁻², and a fill factor (FF) of 77%, which is in agreement with the values reported for the cesium-containing triple cation PSCs previously [31].

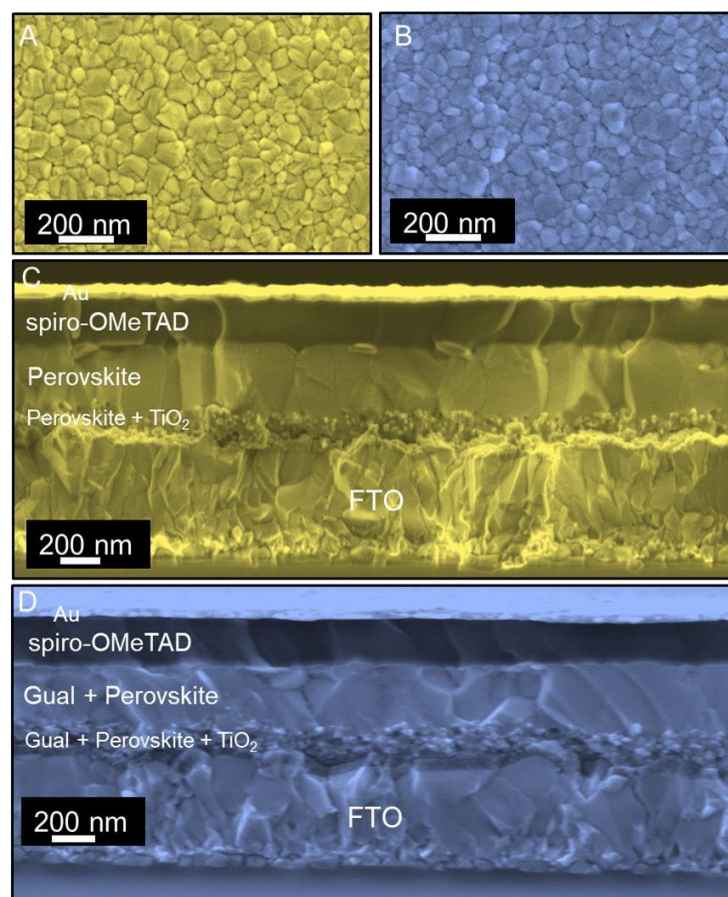


Figure 2.2 Morphological characterization. (A), (B), Top view SEM micrographs acquired from Cs_5Pb , and $\text{Cs}_5\text{Pb.0.05GuaI}$ films (C), (D), Cross-sectional SEM micrographs acquired from the fully assembled devices based on Cs_5Pb , and $\text{Cs}_5\text{Pb.0.05GuaI}$ films.

The PCE of $\text{Cs}_5\text{Pb.0.05GuaI}$ based device is comparable to that of the reference device (Table 2.1). With respect to the Cs_5Pb based device, the $\text{Cs}_5\text{Pb.0.05GuaI}$ devices showed higher J_{SC} values of 23.6 mA/cm^2 . Intriguingly, the addition of 5% GuaI to Cs_5Pb significantly improved the V_{OC} from 1.13 V to 1.20 V. To the best of our knowledge, a V_{OC} of 1.20 V is among the highest values reported in the literature for a similarly configured PSC. Consistent with the PL data, Figure 2.3(B) shows the incident photon-to-current efficiency (IPCE) and integrated current density as a function of wavelength. From the IPCE spectra, we found that upon the addition of 5% GuaI (Figure 2.3(B)), the same number of photons appears to generate more current compared to the reference Cs_5Pb device. Based on the photovoltaic characterization, we found that the incorporation of 5% GuaI into mixed-cation and mixed-

halide perovskite films improved the overall performance of PSCs. The reproducibility of the device performance was further ascertained by measuring 22 devices each from Cs₅Pb and Cs₅Pb.0.05GuaI as shown in Figure 2.3(C). We noted that a V_{OC} between 1.19-1.20 V is consistently achievable. By contrast, the fill factor of the Cs₅Pb.0.05GuaI devices is lower than that of the Cs₅Pb reference. Generally, the FF of a solar cell is affected by the series resistance (R_s) and ideality factor of the device [33]. By taking the slope of light J - V characteristics at the V_{OC} , R_s was calculated and summarized in Table S2.1. The Cs₅Pb.0.05GuaI device exhibits a higher value of R_s as compared to the Cs₅Pb device. Therefore, by simply improving the FF, substantially higher PCEs could be realized.

Table 2.1 Summarized J-V characteristics. J-V characteristics of the best devices with 5% GuaI content in comparison to the reference Cs₅Pb device.

| Samples | J_{sc} (mA/cm²) | V_{oc} (V) | FF (%) | PCE (%) |
|-----------------------------|--|--------------------------------|-------------------|--------------------|
| Cs ₅ Pb | 23.0 | 1.13 | 77 | 20.0 |
| Cs ₅ Pb.0.05GuaI | 23.6 | 1.20 | 70 | 20.3 |

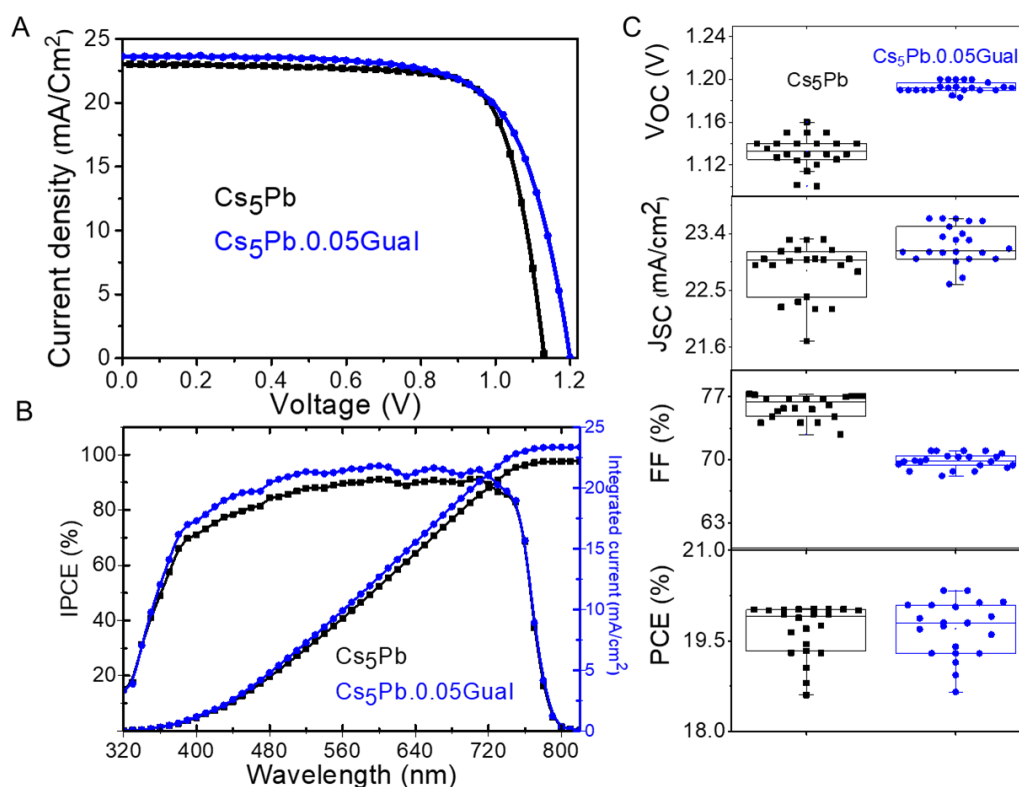


Figure 2.3: Photovoltaic characteristics of the perovskite solar cells based on Cs₅Pb and Cs₅Pb.0.05GuaI films. (A), Current density versus voltage characteristics of perovskite solar cells (B), Incident photon-to-current efficiency spectra as a function of the wavelength and the corresponding integrated J_{SC} (C), J-V metrics for 22 devices using Cs₅Pb and Cs₅Pb.0.05GuaI films.

2..2.3 Insight about the Hysteresis Behaviour. The Cs₅Pb and Cs₅Pb.0.05GuaI based devices were also examined for hysteresis (Figure S2.2) and despite favorable properties of Gua ions, such as zero dipole moment, the hysteresis effects were more prominent in GuaI based devices [34]. To understand the cause of the dominant hysteresis feature [35], capacitance frequency measurements at zero bias in the dark were carried out (Figure 2.3(A)), where features in the low and high frequency of C-f response are clearly distinguishable. A constant capacitance element at a frequency >10³ Hz for Cs₅Pb and >10⁴ Hz for Cs₅Pb.0.05GuaI based devices is associated with the dielectric response of the absorber material. In turn, the capacitance in the low-frequency spectra could be associated with the ionic characteristics [35, 36]. Apparently,

excess Gua ions, which are not confined within the perovskite crystal lattice and have weak bonding capability, could pile up near the contact interface and screen the local electric field leading to a higher value of capacitance in the low-frequency region [37]. By considering the electrostatic interactions at room temperature, space charge densities of $6.04 \times 10^{17} \text{ cm}^{-3}$ and $1.4 \times 10^{18} \text{ cm}^{-3}$ were obtained, respectively, for the reference and $\text{Cs}_5\text{Pb}_0.05\text{GuaI}$ devices. The accumulation of relatively higher ions causes an excess capacitance in the low frequency, which consequently leads to hysteresis. Furthermore, the motion of these ions under the applied bias can screen the internal electric field at the interface ($\text{TiO}_2/\text{perovskite}$), thus amplifying the hysteresis effect.

2.2.4 Electroluminescence Study. Electroluminescence (EL) measurements were carried out to compare the radiative emission properties of Cs_5Pb and $\text{Cs}_5\text{Pb}_0.05\text{GuaI}$ PSCs. The EL was measured during a voltage sweep from 0 to 2 V and back. Figure S3 shows the J - V curve (solid lines) and emitted photon flux (dashed lines) obtained from Cs_5Pb and $\text{Cs}_5\text{Pb}_0.05\text{GuaI}$ devices by a voltage loop starting from 0 V with a scan rate of 20 mV/s. The current onset is shifted towards higher voltages upon the addition of GuaI (solid lines), consistent with the increased V_{OC} . This comes along with a roughly four-times higher radiative emission yield when compared at the same driving current (Figure 2.3(A)). Therefore, the increased PL signal and lifetime of charge carriers observed in perovskite films could be maintained. Following the approach in [38], V_{OC} can be derived from the emission yield (Table 2.2). The calculated values of 1.16 and 1.19 V for Cs_5Pb and $\text{Cs}_5\text{Pb}_0.05\text{GuaI}$, respectively, coincide with the experimental data.

2.1.5 Operational Stability of the Perovskite Solar Cells. Finally, the operational stability of Cs_5Pb and $\text{Cs}_5\text{Pb}_0.05\text{GuaI}$ based devices was investigated at a maximum power point under constant one-sun illumination for 200 h in a nitrogen environment (Figure 2.3(C))

[39]. It is evident that Cs₅Pb and Cs₅Pb.0.05GuaI remain relatively stable for almost 200 h, which indicates that the incorporation of Gua cations, an organic species, does not introduce any additional source of degradation [40]. Thus far, such promising operational stability has not been demonstrated for >20% efficient guanidinium-based PSCs yielding photovoltage as high as 1.20 V, which makes this investigation highly important.

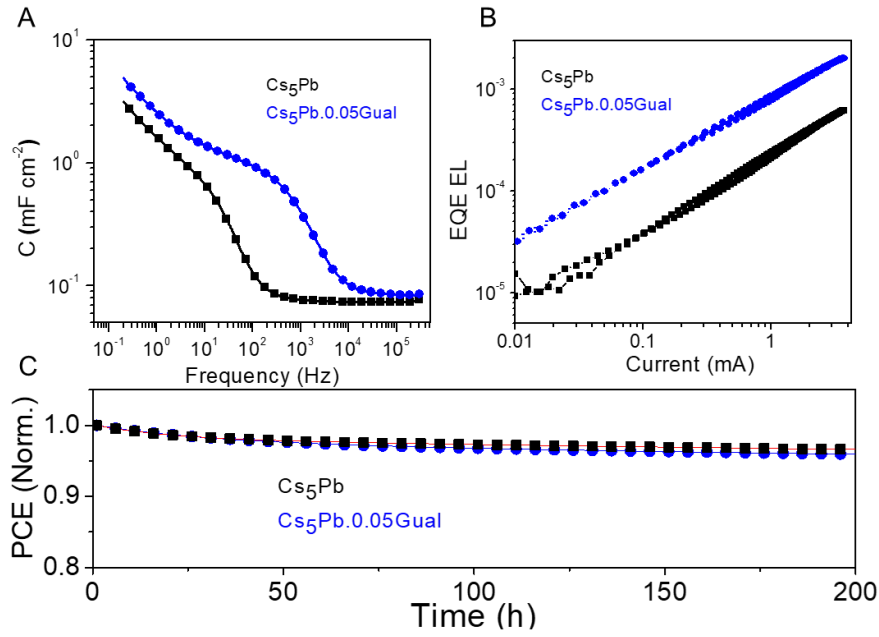


Figure 2.3 Electroluminescence and stability measurements. (A), Capacitance versus frequency spectra of Cs₅Pb and Cs₅Pb.0.05GuaI based devices under short circuit conditions in the frequency range of 200 MHz to 1 MHz. The active area of perovskite solar cell is 0.16 cm² for both the measurements, (B), External electroluminescence quantum efficiency as a function of the injection current for the Cs₅Pb, and Cs₅Pb.0.05GuaI devices, (C), A comparison of operational stability of Cs₅Pb and Cs₅Pb.0.05GuaI devices. The devices were measured under a nitrogen environment at room temperature under constant illumination (LED source, approximated 1 Sun) at a maximum power point for 200 h.

Table 2.2 Summarized electroluminescence data. Summary of the observed and calculated parameters derived from the electroluminescence data.

| Device | V_{OC} , rad | EQE EL at injection current approx. J_{SC} | Nonrad. loss | $V_{OC,calc.}$ |
|-----------------------------|----------------|--|--------------|----------------|
| Cs ₅ Pb | 1.34 V | 0.09 % | 180 mV | 1.16 V |
| Cs ₅ Pb.0.05GuaI | 1.34 V | 0.3 % | 150 mV | 1.19 V |

2.3 Discussion

We investigated the effect of guanidinium iodide incorporation into mixed-cation and mixed-halides perovskite films. Apparently, a slight red shift from 757 to 766 nm in the PL peak position indicates the incorporation of GuaI in the perovskite lattice. A gradual increase in the content of GuaI shows a significant enhancement of the open circuit voltage from 1.13 V to 1.20 V leading to the realization of >20.3% PCE. The increased photoluminescence and lifetime of charge carriers observed in GuaI containing perovskite films were maintained in the fully assembled device, justifying the trends in the V_{OC} . PSCs containing a definite amount of GuaI showed four-times higher radiative emission yield than Cs_5Pb devices. The accumulation of higher ions in GuaI based PSCs causes an excess capacitance in the low-frequency response of capacitance-frequency measurements, which eventually increased the hysteresis. The realization of high photovoltages is quite intriguing, although while dealing with low FF values. Both parameters, i.e., V_{OC} and FF, are interdependent as both are subservient to the ideality factor. Therefore, by simply improving the electronic and interfacial quality in the guanidinium iodide-based perovskite systems, the FF values could be improved. Consequently, much higher photovoltages thus efficiencies exceeding record values can be achieved from the resulting perovskite solar cells. Finally, the thorough understanding gained through in-depth analyses unfolded the reasons leading to the realization of operationally stable and highly efficient (>20%) PSCs yielding photovoltage as high as 1.20 V. Our study shows that there is still plenty of room to improve PCE to new record levels by strategically maneuvering the precursor chemistry.

2.4 Materials and Methods

2.4.1 Experimental Design

We aimed to fabricate highly reproducible and highly efficient perovskite solar cells yielding remarkable photovoltages by judiciously tailoring the photophysical properties of perovskite structures. In this direction, the following steps and detailed characterization techniques, including spectroscopy, scanning electron microscopy, X-ray diffraction, and other device characterization techniques were employed.

2.4.2 Materials

All materials were purchased from Sigma-Aldrich and were used as received, unless stated otherwise.

2.4.3 Substrate preparation

Fluorine-doped tin oxide (FTO)-glass substrates (TCO glass, NSG 10, Nippon sheet glass, Japan) were chemically etched using Zn powder and 4 M HCl and cleaned by ultrasonication in Hellmanex (2%, deionized water), rinsed thoroughly with de-ionized water and ethanol, and then treated with oxygen plasma for 15 min. A 30 nm blocking layer (TiO₂) was deposited on the cleaned FTO by spray pyrolysis at 450 °C using a commercial titanium diisopropoxide bis(acetylacetonate) solution (75% in 2-propanol, Sigma-Aldrich) diluted in anhydrous ethanol (1:9, volume ratio) as precursor and oxygen as a carrier gas. A 150 nm mesoporous TiO₂ layer was deposited by spin-coating a diluted paste (1:6 wt. ratio) (Dyesol 30NRD: ethanol) (4000 rpm, acceleration 2000 rpm for 20 s) onto the substrate containing TiO₂ compact layer, and then sintered at 450 °C for 30 min in dry air. For Li treatment of mesoporous TiO₂, 150 µL of LiTFSI solution in acetonitrile (10mg/mL, freshly prepared in an argon atmosphere) was spin-coated (3000

rpm, acceleration 2000 rpm for 20 s) after a loading time of 10 s. Thereafter, Li treated substrates were sintered at 450 °C for 30 min.

2.4.4 Deposition of perovskite films

The perovskite films were deposited using a single-step deposition method from the precursor solution containing FAI (1M), PbI₂ (1.1 M), MABr (0.2 M), and PbBr₂ (0.2 M) in anhydrous dimethylformamide/ dimethylsulphoxide (4:1 (volume ratio)). Thereafter, 5% of CsI (Acros 99.9%) (1.5 M DMSO) (1.5 M DMSO) was added to the perovskite precursor solution. The precursor solution was spin-coated onto the mesoporous TiO₂ films in a two-step program at 1000 and 6000 r.p.m. for 10 and 30 s, respectively. During the second step, 130 µl of chlorobenzene was dropped on the spinning substrate 10 s prior the end of the program. This was followed by annealing the films at 100 °C for 40 min. The device fabrication was carried out under controlled atmospheric conditions with humidity <2%. For completing the fabrication of devices, 2,2',7,7'-tetrakis(N,N-di-p-methoxyphenylamine)-9,9-spirobifluorene (spiro-OMeTAD, 60 mM in chlorobenzene), the HTM was doped with bis(trifluoromethylsulfonyl)imide lithium salt, tris(2-(1H-pyrazol-1-yl)-4-tert-butylpyridine)-cobalt(III) tris(bis(trifluoromethylsulfonyl) imide) (FK 209, from Dyenamo) and 4-tert-Butylpyridine in a molar ratio of 0.5, 0.05 and 3.3, respectively. Finally, ~75 nm gold (Au) layer was thermally evaporated.

2.4.5 Device characterization

The current-voltage (J-V) characteristics of the perovskite devices were recorded with a digital source meter (Keithley model 2400, USA). A 450 W xenon lamp (Oriel, USA) was used as the light source for photovoltaic (J-V) measurements. The spectral output of the lamp was filtered using a Schott K113 Tempax sunlight filter (Präzisions Glas & Optik GmbH, Germany) to reduce the mismatch between the simulated and actual solar spectrum

to less than 2%. The photo-active area of 0.16 cm^2 was defined using a dark-coloured metal mask. The IPCE measurements were performed using a LED light source (Ariadne EQE from Cicci Research).

2.4.6 Morphological characterization

Scanning electron microscopy (SEM) was performed on a ZEISS Merlin HR-SEM using an In-lens detector.

2.4.7 Structural characterization

X-ray diffraction data were collected on a Bruker Advance D8 X-ray diffractometer with a graphite monochromator, using $\text{Cu K}\alpha$ radiation.

2.4.8 Spectroscopic measurements

UV-vis measurements were performed on a Varian Cary 5. Photoluminescence spectra were obtained with a Florolog 322 (Horiba Jobin Yvon Ltd) in the wavelength range from 500 nm to 850 nm by exciting at 460 nm. The spectrometer working in a time-correlated single-photon counting mode with $< \text{ns}$ time resolution was used for the time-resolved photoluminescence studies. Picosecond pulsed diode laser head NanoLED-405LH (Horiba) emitting $< 200 \text{ ps}$ duration pulses at 408 nm with a repetition rate of 1 MHz was used as an excitation source.

2.4.9 Electroluminescence measurements

The emitted photon flux was detected with a large-area (1 cm^2) Si-photodiode (Hamamatsu S1227-1010BQ) positioned close to the sample. The voltage scan was performed using a Bio-Logic SP300 potentiostat, which was also used to simultaneously measure the short circuit current of the photodiode connected to a second channel.

2.4.10 Long-term light soaking test

Stability measurements were performed using a home-built system with white LED illumination with an intensity equivalent to 1 sun. The devices were kept at maximum power point (MPP) by a custom-made computer controlled MPP tracking routine. The inert atmosphere was achieved by flushing the sample holder with nitrogen.

2.5 Supplementary Materials

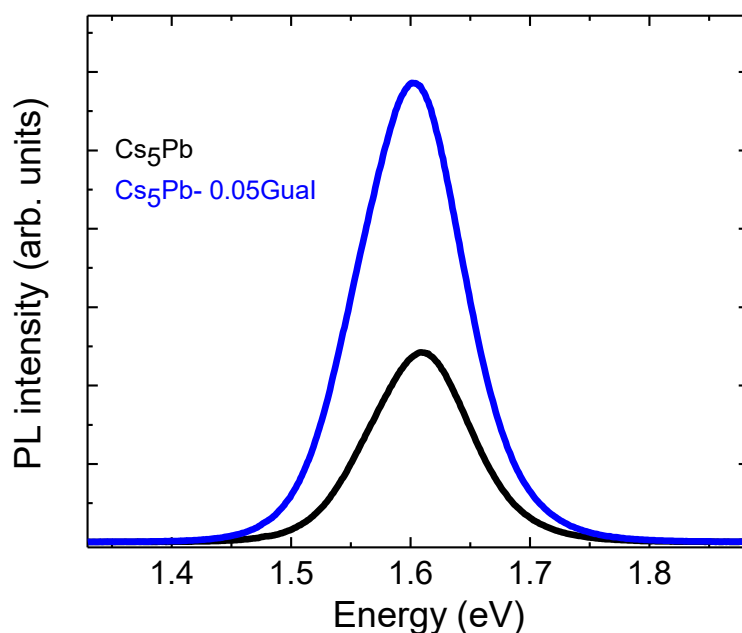


Figure S2.1: Photoluminescence spectra recorded from Cs₅Pb.*x*GuaI films deposited onto the mesoporous Al₂O₃ substrate.

Table S2.1. Summarized *J-V* characteristic of the devices with 5% GuaI content in comparison to the reference Cs₅Pb device:

| Samples | J_{sc} (mA/cm ²) | V_{oc} (V) | FF (%) | PCE (%) | Series Resistance (R_s) (Ω.cm ²) |
|-----------------------------|--------------------------------|--------------|--------|---------|--|
| Cs ₅ Pb | 23.0 | 1.13 | 76.8 | 20.0 | 3.5 |
| Cs ₅ Pb.0.05GuaI | 23.6 | 1.20 | 70.3 | 20.3 | 5.0 |

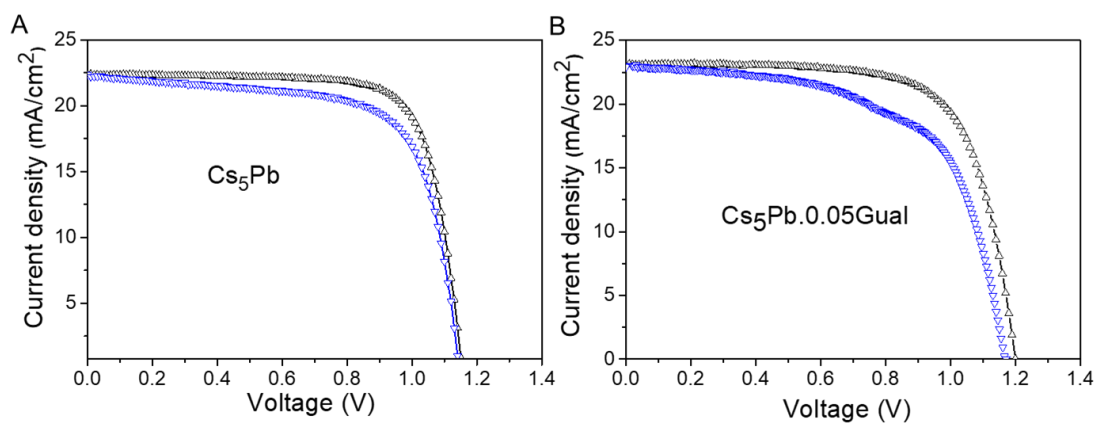


Figure S2.2: Forward and reverse current-voltage scans for (a) Cs_5Pb , and (b) $\text{Cs}_5\text{Pb.0.05GuaI}$ devices.

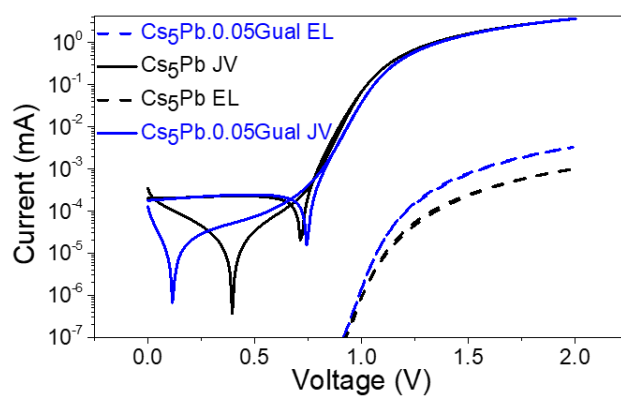


Figure S2.3: J - V curve (solid lines) and emitted photon flux (dashed lines) obtained from Cs_5Pb and $\text{Cs}_5\text{Pb.0.05GuaI}$ devices by a voltage loop starting from 0 V with a scan rate of 20 mV/s.

Differences in current at low voltages are due to the hysteresis phenomenon.

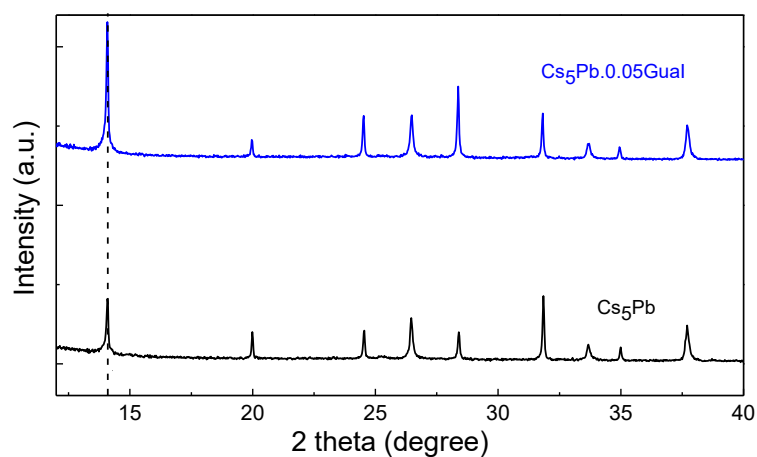


Fig. S2.4. X-ray diffraction patterns corresponding to pure and GuaI containing perovskite films.

2.6 References

- [1] C. C. Stoumpos, C. D. Malliakas, and M. G. Kanatzidis, “Semiconducting tin and lead iodide perovskites with organic cations: phase transitions, high mobilities, and near-infrared photoluminescent properties,” *Inorganic Chemistry*, vol. 52, no. 15, pp. 9019–9038, 2013.
- [2] A. Kojima, K. Teshima, Y. Shirai, and T. Miyasaka, “Organometal halide perovskites as visible-light sensitizers for photovoltaic cells,” *Journal of the American Chemical Society*, vol. 131, no. 17, pp. 6050–6051, 2009.
- [3] M. M. Lee, J. Teuscher, T. Miyasaka, T. N. Murakami, and H. J. Snaith, “Efficient hybrid solar cells based on mesosuperstructured organometal halide perovskites,” *Science*, vol. 338, no. 6107, pp. 643–647, 2012.
- [4] H.-S. Kim, C.-R. Lee, J.-H. Im et al., “Lead iodide perovskite sensitized all-solid-state submicron thin film mesoscopic solar cell with efficiency exceeding 9%,” *Scientific Reports*, vol. 2, article 591, 2012.
- [5] H. Zhu, Y. Fu, F. Meng et al., “Lead halide perovskite nanowire lasers with low lasing thresholds and high quality factors,” *Nature Materials*, vol. 14, no. 6, pp. 636–642, 2015.
- [6] G. Xing, N. Mathews, S. S. Lim et al., “Low-temperature solution-processed wavelength-tunable perovskites for lasing,” *Nature Materials*, vol. 13, no. 5, pp. 476–480, 2014.
- [7] “NRELchart,” <https://www.nrel.gov/pv/assets/pdfs/pv-efficiency-chart.20181221.pdf>.
- [8] T. Leijtens, S. D. Stranks, G. E. Eperon et al., “Electronic properties of meso-superstructured and planar organometal halide perovskite films: Charge trapping, photodoping, and carrier mobility,” *ACS Nano*, vol. 8, no. 7, pp. 7147–7155, 2014.
- [9] M. I. Dar, A. Hinderhofer, G. Jacopin et al., “Function follows form: correlation between the growth and local emission of perovskite structures and the performance of solar cells,” *Advanced Functional Materials*, vol. 27, no. 26, Article ID 1701433, 2017.
- [10] D. Shi, V. Adinolfi, R. Comin et al., “Low trap-state density and long carrier diffusion in organolead trihalide perovskite single crystals,” *Science*, vol. 347, no. 6221, pp. 519–522, 2015.
- [11] H. D. Kim, H. Ohkita, H. Benten, and S. Ito, “Photovoltaic performance of perovskite solar cells with different grain sizes,” *Advanced Materials*, vol. 28, no. 5, pp. 917–922, 2016.

- [12] Y. Hou, W. Chen, D. Baran et al., “Overcoming the interface losses in planar heterojunction perovskite-based solar cells,” *Advanced Materials*, vol. 28, no. 25, pp. 5112–5120, 2016.
- [13] H. Chen, W. Fu, C. Huang et al., “Molecular engineered hole-extraction materials to enable dopant-free, efficient p-i-n perovskite solar cells,” *Advanced Energy Materials*, vol. 7, no. 18, p. 1700012, 2017.
- [14] J.-P. Correa-Baena, W. Tress, K. Domanski et al., “Identifying and suppressing interfacial recombination to achieve high open-circuit voltage in perovskite solar cells,” *Energy & Environmental Science*, vol. 10, no. 5, pp. 1207–1212, 2017.
- [15] N. Arora, M. I. Dar, M. Abdi-Jalebi et al., “Intrinsic and extrinsic stability of formamidinium lead bromide perovskite solar cells yielding high photovoltage,” *Nano Letters*, vol. 16, no. 11, pp. 7155–7162, 2016.
- [16] M. L. Agiorgousis, Y.-Y. Sun, H. Zeng, and S. Zhang, “Strong covalency-induced recombination centers in perovskite solar cell material $\text{CH}_3\text{NH}_3\text{PbI}_3$,” *Journal of the American Chemical Society*, vol. 136, no. 41, pp. 14570–14575, 2014.
- [17] D. W. de Quilettes, S. M. Vorpahl, S. D. Stranks et al., “Impact of microstructure on local carrier lifetime in perovskite solar cells,” *Science*, vol. 348, no. 6235, pp. 683–686, 2015.
- [18] J. S. Manser, J. A. Christians, and P. V. Kamat, “Intriguing optoelectronic properties of metal halide perovskites,” *Chemical Reviews*, vol. 116, no. 21, pp. 12956–13008, 2016.
- [19] M. Yang, Y. Zeng, Z. Li et al., “Do grain boundaries dominate non-radiative recombination in $\text{CH}_3\text{NH}_3\text{PbI}_3$ perovskite thin films?” *Physical Chemistry Chemical Physics*, vol. 19, no. 7, pp. 5043–5050, 2017.
- [20] V. D’Innocenzo, A. R. Srimath Kandada, M. De Bastiani, M. Gandini, and A. Petrozza, “Tuning the light emission properties by band gap engineering in hybrid lead halide perovskite,” *Journal of the American Chemical Society*, vol. 136, no. 51, pp. 17730–17733, 2014.
- [21] S. D. Stranks, V. M. Burlakov, T. Leijtens, J. M. Ball, A. Goriely, and H. J. Snaith, “Recombination kinetics in organic-inorganic perovskites: excitons, free charge, and subgap states,” *Physical Review Applied*, vol. 2, no. 3, Article ID 034007, 2014.
- [22] X. Li, M. Ibrahim Dar, C. Yi et al., “Improved performance and stability of perovskite solar cells by crystal crosslinking with alkylphosphonic acid ω -ammonium chlorides,” *Nature Chemistry*, vol. 7, no. 9, pp. 703–711, 2015.

- [23] A. Abate, M. Saliba, D. J. Hollman et al., “Supramolecular halogen bond passivation of organic-inorganic halide perovskite solar cells,” *Nano Letters*, vol. 14, no. 6, pp. 3247–3254, 2014.
- [24] Y. Wang, T. Zhang, M. Kan, and Y. Zhao, “Bifunctional stabilization of all-inorganic α -CsPbI₃ perovskite for 17% efficiency photovoltaics,” *Journal of the American Chemical Society*, vol. 140, no. 39, pp. 12345–12348, 2018.
- [25] N. D. Marco, H. Zhou, Q. Chen et al., “Guanidinium: a route to enhanced carrier lifetime and open-circuit voltage in hybrid perovskite solar cells,” *Nano Letters*, vol. 16, no. 2, pp. 1009–1016, 2016.
- [26] G. Giorgi, J.-I. Fujisawa, H. Segawa, and K. Yamashita, “Organic - Inorganic hybrid lead iodide perovskite featuring zero dipole moment guanidinium cations: A theoretical analysis,” *The Journal of Physical Chemistry C*, vol. 119, no. 9, pp. 4694–4701, 2015.
- [27] A. D. Jodlowski, C. Roldan-Carmona, G. Grancini et al., “Large’ guanidinium cation mixed with methylammonium in lead iodide perovskites for 19% efficient solar cells,” *Nature Energy*, vol. 2, no. 12, pp. 972–979, 2017.
- [28] X. Hou, Y. Hu, H. Liu et al., “Effect of guanidinium on mesoscopic perovskite solar cells,” *Journal of Materials Chemistry A*, vol. 5, no. 1, pp. 73–78, 2017.
- [29] D. J. Kubicki, D. Prochowicz, A. Hofstetter et al., “Formation of stable mixed guanidinium-methylammonium phases with exceptionally long carrier lifetimes for high-efficiency lead iodide-based perovskite photovoltaics,” *Journal of the American Chemical Society*, vol. 140, no. 9, pp. 3345–3351, 2018.
- [30] O. Nazarenko, M. R. Kotyrba, M. Worle, E. Cuervo-Reyes, S. Yakunin, and M. V. Kovalenko, “Luminescent and photoconductive layered lead halide perovskite compounds comprising mixtures of cesium and guanidinium cations,” *Inorganic Chemistry*, vol. 56, no. 19, pp. 11552–11564, 2017.
- [31] N. Arora, M. I. Dar, A. Hinderhofer et al., “Perovskite solar cells with CuSCN hole extraction layers yield stabilized efficiencies greater than 20%,” *Science*, vol. 358, no. 6364, pp. 768–771, 2017.
- [32] M. I. Dar, G. Jacopin, S. Meloni et al., “Origin of unusual bandgap shift and dual emission in organic-inorganic lead halide perovskites,” *Science Advances*, vol. 2, no. 10, Article ID e1601156, 2016.

- [33] P. Yadav, M. I. Dar, N. Arora et al., “The role of rubidium in multiple-cation-based high-efficiency perovskite solar cells,” *Advanced Materials*, vol. 29, no. 40, Article ID 1701077, 2017.
- [34] C. Eames, J. M. Frost, P. R. F. Barnes, B. C. O'Regan, A. Walsh, and M. S. Islam, “Ionic transport in hybrid lead iodide perovskite solar cells,” *Nature Communications*, vol. 6, article 7497, 2015.
- [35] E. L. Unger, E. T. Hoke, C. D. Bailie et al., “Hysteresis and transient behavior in current-voltage measurements of hybrid perovskite absorber solar cells,” *Energy & Environmental Science*, vol. 7, no. 11, pp. 3690–3698, 2014.
- [36] I. Zarazua, J. Bisquert, and G. Garcia-Belmonte, “Light-induced space-charge accumulation zone as photovoltaic mechanism in perovskite solar cells,” *The Journal of Physical Chemistry Letters*, vol. 7, no. 3, pp. 525–528, 2016.
- [37] O. Almora, I. Zarazua, E. Mas-Marza, I. Mora-Sero, J. Bisquert, and G. Garcia-Belmonte, “Capacitive dark currents, hysteresis, and electrode polarization in lead halide perovskite solar cells,” *The Journal of Physical Chemistry Letters*, vol. 6, no. 9, pp. 1645–1652, 2015.
- [38] W. Tress, N. Marinova, O. Inganäs, M. K. Nazeeruddin, S. M. Zakeeruddin, and M. Graetzel, “Predicting the open-circuit voltage of $\text{CH}_3\text{NH}_3\text{PbI}_3$ perovskite solar cells using electroluminescence and photovoltaic quantum efficiency spectra: The role of radiative and non-radiative recombination,” *Advanced Energy Materials*, vol. 5, no. 3, Article ID 1400812, 2014.
- [39] H. Tan, A. Jain, O. Voznyy et al., “Efficient and stable solution processed planar perovskite solar cells via contact passivation,” *Science*, vol. 355, no. 6326, pp. 722–726, 2017.
- [40] D. Bryant, N. Aristidou, S. Pont et al., “Light and oxygen induced degradation limits the operational stability of methylammonium lead triiodide perovskite solar cells,” *Energy & Environmental Science*, vol. 9, no. 5, pp. 1655–1660, 2016.

Chapter 3.

Atomic-level passivation mechanism of ammonium salts enabling highly efficient perovskite solar cells

This work has been published: E. A. Alharbi, A. Y. Alyamani, D. J. Kubicki, A. R. Uhl, B. J. Walder, A. Q. Alanazi, J. Luo, A. Burgos-Caminal, A. Albadri, H. Albrithen, M. H. Alotaibi, J. E. Moser, S. M. Zakeeruddin, F. Giordano, L. Emsley and M. Grätzel, Nat. Commun., 2019, 10, 1–9.

3.1 Introduction

Metal halides perovskite is one of the most promising light-harvesting materials among emerging photovoltaic technologies ^{1, 2-5} solar to electric power conversion efficiencies (PCEs) reaching presently 23.7% ⁶. Their ease of manufacturing together with low-cost fabrication and high performance have made metal halide perovskites a true breakthrough in thin-film solar cell technology. However, solution deposition methods are prone to produce pinholes and defects whether at the grain boundaries or at the surface which is considered one of the reasons behind a low device performance and stability.^{7,8}. One major obstacle to the development and commercialization of this technology continues to be the operational stability of photovoltaic devices. Despite the vast progress that has been achieved on the synthesis of high-quality multi-crystalline films, some complex problems have only been partially mitigated ³. The often observed hysteretic behavior during *J-V* characterization, caused by ion mobility, can be considered a primary indication for the intrinsic long-term steady-state instability ⁹. In that respect, the phase stabilization of specific perovskite formulations has been the object of thorough investigation ^{2,10,11}. Recently, the reduction of defects at the surface and grain boundaries of the perovskite film as well as at the interfaces with the electrical contacts, has attracted great interest for its dramatic impact on the operational stability and efficiency of the device ^{7,12}. Mitigation of surface defects, whether at the interface of perovskite/HTL or perovskite/electron transport layer (ETL), provides the added benefit of

improving the open circuit voltage (V_{oc}) without affecting the charge carrier transport or the fill factor (FF). Previous studies have employed several types of ammonium cations in order to impede the charge carrier recombination losses occurring at the interfaces or throughout the bulk of the perovskite film. Amongst those, formamidinium bromide (FABr) was used as an electron blocking layer, forming a wide band gap over layer ($\text{FAPbBr}_{3-x}\text{I}_x$) at the interface between the perovskite/HTL and consequently improving V_{oc} by approximately 60 mV¹³. In a similar manner methylammonium iodide (MAI) was thermally evaporated at the interface perovskite/HTL, enhancing efficiency from 14.5% to 17.2% with a high reproducibility¹⁴. Lately, quaternary ammonium halides were found to decrease the ionic defects at the perovskite surface and significantly improve efficiency and stability⁷. Furthermore, phenylalkylamine molecules^{15 16}, and polymers¹⁷ have been used to improve the efficiency and moisture tolerance of perovskite solar cells (PSC). Moreover, guanidinium¹⁸⁻²¹, ethylammonium^{22,23} and imidazolium^{24,25} have been used as an additive to improve different aspects of PSC operation. Herein we report a facile strategy to tailor the interface between the perovskite and the HTL. We show that the modification of the perovskite surface via the addition of organic ammonium salts, namely, ethylammonium iodide ($[(\text{C}_2\text{H}_5)\text{NH}_3]\text{I}$, (EAI)), imidazolium iodide ($[\text{C}_3\text{N}_2\text{H}_5]\text{I}$, (IAI)), and guanidinium iodide ($[\text{C}(\text{NH}_2)_3]\text{I}$, (GuaI)), considerably increases the device performance. We use mixed cation/halide perovskite formulations of the composition $(\text{FA}_{0.9}\text{Cs}_{0.07}\text{MA}_{0.03}\text{Pb}(\text{I}_{0.92}\text{Br}_{0.08})_3)$ with 3% excess of PbI_2 . These agents greatly reduce the hysteresis in the JV curve improving the solar to electric power conversion efficiency from 20.5% for the control device to 22.3%, 22.1% and 21.0% for the EAI-, IAI-, and GuaI-treated device, respectively. Moreover, defect mitigation improves the operational stability for the PSC's which was tested at a full solar intensity under maximum power tracking condition for 550 h with a small loss of only 5% for the best performing devices.

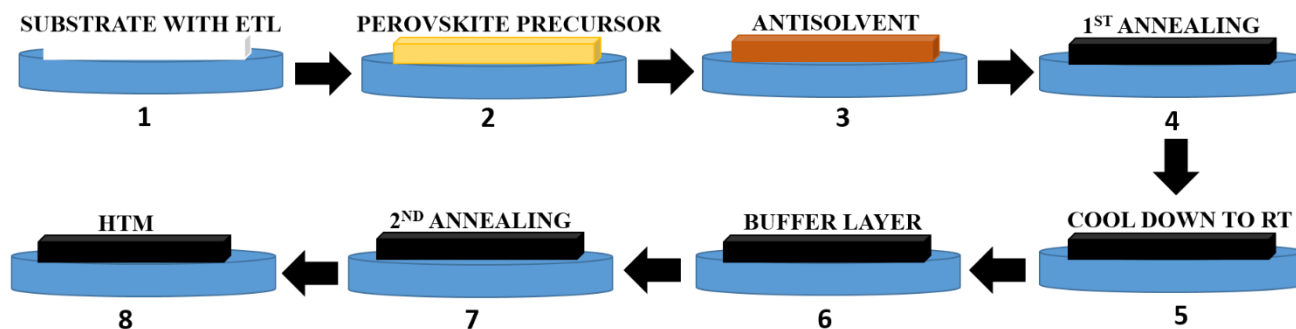


Figure 3.1. Scheme of our method for treating perovskite films by spin-coating of different organic ammonium salts (EAI, IAI, and Gual) and consecutive annealing.

3.2 Results.

3.2.2 Characterization and Fabrication of perovskite thin films. We employed a device architecture comprising an FTO glass substrate, on top of which we deposited a compact TiO₂ layer followed by mesoporous TiO₂/perovskite/passivation layer/spiro-OMeTAD/gold. The complete procedure for the device fabrication is detailed in the method section. In short, the perovskite film was annealed at 150 °C for 30 to 40 min. After cooling down to room temperature, the passivation layer was immediately deposited by spin-coating a solution of ammonium salt (EAI, IAI, and Gual) in isopropanol and subsequent annealing at 70°C for 10 to 15 minutes. The concentration of the solution was optimized for each compound investigated (Supplementary Table S3.1) and the different treatments were compared at their best condition. We note that the high annealing temperature could potentially drive off methylammonium from the thin film. Solid-state NMR quantification²⁶ of the cation content of our films yielded 0.97 mol % FA and 0.03 mol % MA which agrees with the stoichiometry of the precursor solution, indicating that MA is fully retained in the final perovskite composition even after the high annealing (Supplementary Figure S3.1 and Supplementary Note 3.1).

The surface treatment described above significantly modifies the perovskite composition and surface morphology due to a chemical reaction with the perovskite. This was traced by crystallographic structure analysis of the perovskite film using X-ray diffraction (XRD). Figure 3.2a and Supplementary Figure S3.2a,b,c, reveal the presence of unreacted PbI_2 ($2\theta=12.7^\circ$) which is expected since the precursor solution contains 3% excess of PbI_2 . All three surface treatments have a similar effect on the XRD pattern. In particular, for concentrations above 3 mg/ml for all treatments, the PbI_2 peaks completely disappear (Figure 3.2a and Supplementary Figure S3.2a-c), presumably via the formation of a thin non-perovskite cover layer of EA/IA/Gua lead halide on top of the perovskite film. We have recently shown that solid-state magic angle spinning (MAS) NMR can be used to probe this kind of atomic-level microstructure of multi-component lead halide perovskites^{21 26-28}. We, therefore, test the hypothesis by carrying out solid-state NMR measurements on a thin film of $\text{FA}_{0.93}\text{Cs}_{0.07}\text{PbI}_3$ (further referred to as CsFA(I)) treated with EAI (5mg ml⁻¹). (We used the pure-iodide CsFA(I) composition to avoid the overlap between MA and EA ¹H signals and the formation of mixed iodide-bromide phases which would complicate the interpretation.) Figure 3.2b shows a ¹H solid-state MAS NMR spectrum of the CsFA(I) thin-film treated with 5 mg/ml EAI and identifies the presence of two organic cations in the film: FA (8.1 ppm (CH) and 7.3 ppm (NH_2^+)) as well as EA (6.3 ppm (NH_3^+), 3.6 ppm (CH_2) and 1.8 (CH_3)). There is no unreacted EAI in the film (Figure 2c), which would give signals at 7.7, 3.3 and 1.6 ppm with a full width at half maximum (FWHM) of 1.5 to 2.0 ppm due to strong ¹H-¹H dipole-dipole couplings. The EA signals in the thin film have FWHM of 0.1 to 0.2 ppm, consistent with lower ¹H density in the EA-containing phase²⁹. The new EA species in the thin film have a spectral signature similar to that of EAPbI_3 (Figure 2d, 6.4, 3.8, and 2.0 ppm). We thus confirm that EAI is fully converted into EA-containing lead halide phases during the passivation treatment.

That said, the EA signals are slightly shifted, indicating a small structural difference with respect to the pure 1D EAPbI₃ phase²⁹. This can be potentially caused by the formation of mixed FA/EA, Cs/EA, and/or Cs/EA/FA phases. We demonstrate this by preparing α -FAPbI₃ substitutionally doped with 10 mol% EAI (FA_{0.9}EA_{0.1}PbI₃) (Figure 3.2e). The spectrum of this material shows a distribution of environments for each of the EA sites (CH₃: 0.6 to 2.3 ppm, CH₂: 3.0 to 4.3, and NH₃⁺: 5.3 to 6.7 ppm). This distribution is likely caused by the formation of mixed FA/EA structures with a varying number of FA slabs separated by EA spacers, in structures similar to those reported for 2-(*1H*-pyrazol-1-yl)pyridine-doped 1D/3D³⁰ and butylammonium- and phenylethylammonium-based 2D/3D materials³¹. We further evidence the formation of mixed FA/EA phases by performing two-dimensional ¹H-¹H spin diffusion experiments which correlate signals based on their spatial proximity (up to around 10 Å)³² (Figure 3.2g). The peaks lying on the diagonal correspond to the species presented in the 1D projection above. On the other hand, off-diagonal peaks indicate that two chemical environments are in atomic-level proximity (an example is illustrated by the dashed orange line). Beside trivial intramolecular contacts, every EA environment (CH₃, CH₂ and NH₂) is correlated to each of the two FA environments (CH and NH₂⁺), demonstrating unambiguously that EA and FA are microscopically mixed within the same phase.

We then carried out the ¹H-¹H spin diffusion measurement on the EAI-treated CsFA(I) thin film and found through-space atomic-level contact between FA and EA (Figure 3.2h, red circles), confirming that the formation of mixed EA/FA phases is general, regardless of the processing conditions. We also show that analogous atomic-level proximities are present in the case of IAI and Gual treatment, confirming the formation of 3D/1D heterostructures in these cases (Supplementary Figure S3.7h-m and Supplementary Figure 3.8). While the exact spectral signature of EA in such mixed phases will depend on the FA/EA ratio and can conceivably be further modified by the presence of Cs, the chemical shift range and line widths corresponding

to the model FA/EA phase matches that observed in the EAI-passivated thin film of CsFA(I). This finding is of paramount importance in that it shows that EAI is fully converted into new mixed EA/FA phases. Since the reaction is aided by IPA and as such happens without redissolution and recrystallization of the perovskite, the new EA/FA phase must form on the surface of the preexisting perovskite grains and its similarity from NMR to the 1D EAPbI_3 suggests it is a 1D structure. We note that it is not possible to quantify the EA/FA ratio in the 1D passivation layer by simply comparing it to reference 1D $\text{FA}_{1-x}\text{EA}_x\text{PbI}_3$ phases (Supplementary Figure 3.7c-g), as in the 3D/1D heterostructure the EA shift is additionally affected by the presence of the 3D perovskite phase in its immediate microscopic environment. This supports the formation of a firmly adhering passivation layer with high ambient stability, owing to the superior stability of 3D perovskites in hybrids with lower dimensionality structures (Figure. 3.2i)³¹. We also provide a comparison with a EA-treated film but without the second annealing step, which shows that the final 3D/1D heterostructure is formed during spin coating (Supplementary Figure 3.7a-b). Finally, we note that solid-state ^1H MAS NMR quantification of the cation content in the passivated thin film revealed that the EA constitutes 10 mol % of the total organic cation content (with 90 mol % FA). After applying straightforward chemical and geometrical consideration, this corresponds to 27 nm thick 1D passivation layer (Supplementary Note 3.2).

Furthermore, the surface morphology of the perovskite films was recorded via scanning electron microscopy (SEM) (Figure 3.3 a-d). In this study, the bulk perovskite composition was kept identical for all the conditions, and only the surface was modified by the treatment with the 3 different agents. From Figure 3 a-d and Supplementary Figure S3.3, we infer that the surface of the treated films shows much smaller grains than the control sample. To rule out the etching of the perovskite surface by IPA as a cause of the roughening, we examined a control film that was treated by neat IPA and ascertained that the solvent on its own does not

modify the perovskite surface morphology (Supplementary Figure S3.3). We then investigate the surface roughness of the perovskite films after the surface treatment using atomic force microscopy (AFM) (Figure 3.3 f-j). It is apparent that the surface roughness, and thereby the corresponding specific surface area, has increased significantly for all the treated samples, with Gual (5mg ml^{-1}) showing the highest root mean square (RMS) roughness of 12.7 nm, followed by EAI (3mg ml^{-1}) with 12.0 nm, IAI (7mg ml^{-1}) with 9.00 nm, and the control with 6.21 nm.

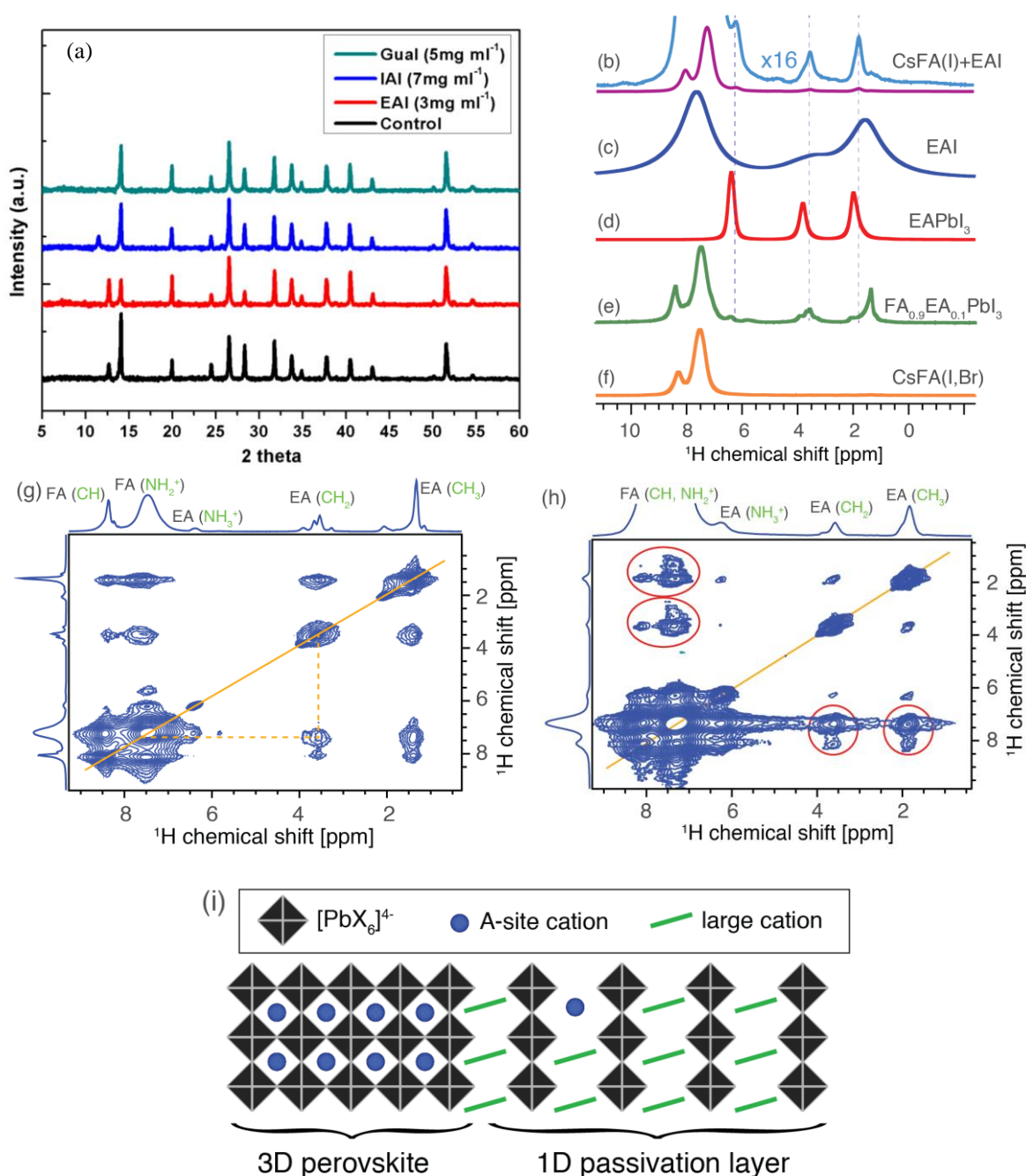


Figure 3.2: Structural characterization of the passivated perovskite films: a) XRD patterns of the treated films compared to the control. Solid-state ^1H MAS NMR measurements at 21.1 T, 300 K and 20 kHz MAS (unless noted otherwise): (b) thin film of CsFA(I) treated with 5 mg ml^{-1} EAI (at 60 kHz MAS), (c) neat EAI, (d) bulk mechanochemical EAPbI_3 , (e) bulk mechanochemical $\text{FA}_{0.9}\text{EA}_{0.1}\text{PbI}_3$, (f) thin film of $\text{FA}_{0.93}\text{Cs}_{0.07}\text{Pb(I}_{0.92}\text{Br}_{0.08})_3$ (CsFA(I,Br)), (g) ^1H - ^1H spin diffusion (20 kHz MAS) experiment evidencing atomic-level proximity between FA and EA in the mixed FA/EA phase; one of the EA/FA cross-peaks has been indicated with dashed lines (h) ^1H - ^1H spin diffusion experiment (60 kHz MAS) evidencing atomic-level proximity between FA and EA in the $\text{FA}_{0.93}\text{Cs}_{0.07}\text{PbI}_3$, thin-film treated with 5 mg/ml EAI (FA/EA cross-peaks in red circles), (i) schematic representation of the 1D/3D heterostructure evidenced by solid-state NMR proximity measurements.

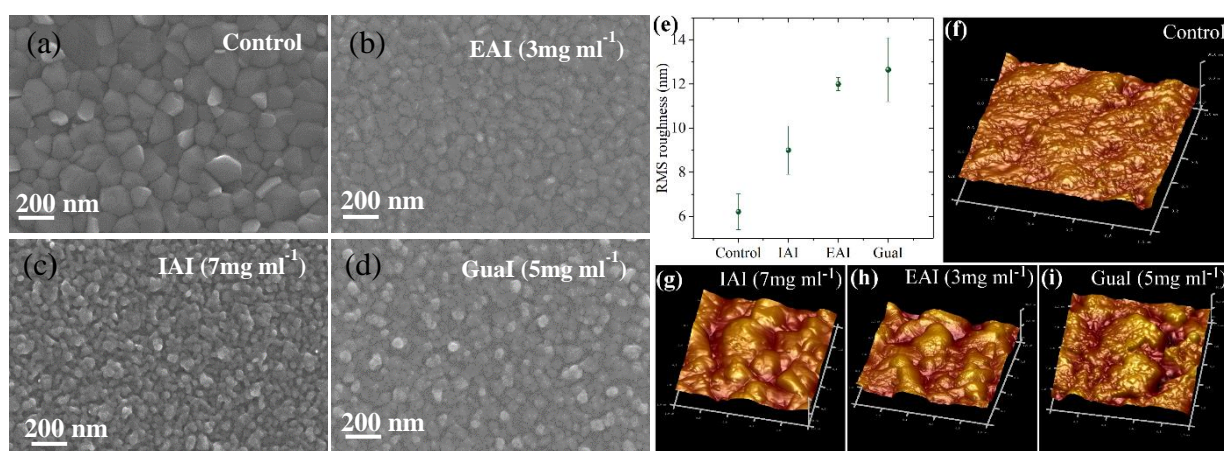


Figure 3.3: Morphological characterization of perovskite layers: a-d) SEM top-view images of the perovskite films with optimized treatment conditions. (e) AFM measurements (x-y: $1 \mu\text{m} \times 1 \mu\text{m}$, z: $0 \pm 90 \text{ nm}$) reveal increasing RMS surface roughness for surface-treated perovskite absorbers: (f) control, (g) IAI, (h) EAI, and (i) Gual.

Figures 3.4a and Supplementary Figure S3.4, show that the absorbance onset for control/IPA corresponded to that of EAI, IAI, and Gual-passivated films indicating that the bandgap of the bulk perovskite was not noticeably affected by the surface treatment. We investigated the steady-state and time-resolved photoluminescence (PL) of the control and modified perovskite layer. Figure 3.4b and Supplementary Figure S3.5 a-d show an increase in PL intensity in response to the post-treatments. This suggests a reduction of the non-radiative recombination losses that could be explained by defect mitigation induced by cation exchange and filling of iodide vacancies at the absorber surface in agreement with previous work on

methyammonium lead iodide films¹⁴. It is worth mentioning that the Gual when applied at 7mg ml⁻¹ and 10mg ml⁻¹ showed a slight red shift as shown in Supplementary Figure 5.

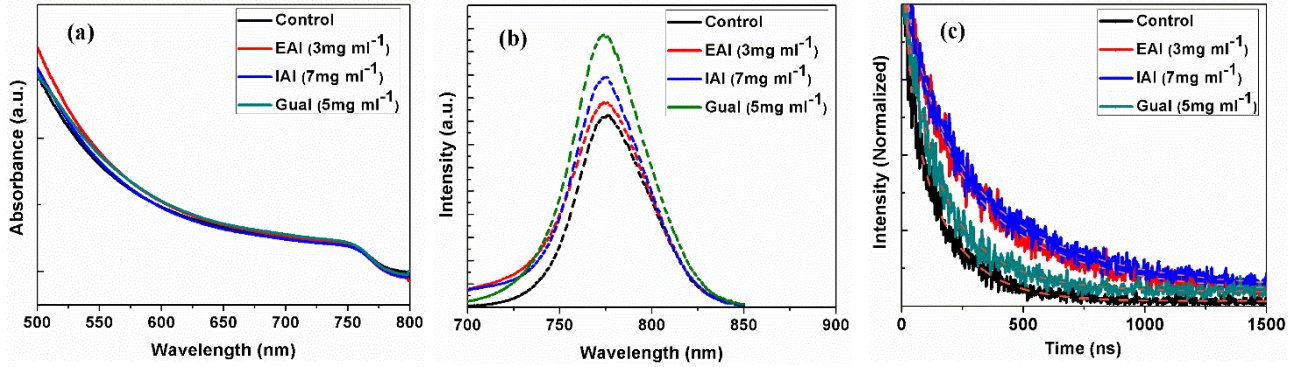


Figure 3.4: Optical properties of perovskite films: a) Absorbance, b) steady-state photoluminescence, and c) time-resolved photoluminescence spectra of treated and untreated perovskite films; dashed lines in the present the fitting curves.

We carried out time-resolved photoluminescence (TRPL) on glass/Al₂O₃/perovskite samples with and without surface treatment. We excited the sample the from the perovskite side using 670 nm wavelength light. By fitting the luminescence decays in Figure 3.4c according to our previously reported procedure²⁷, we derived lifetimes $\tau_1 = 1/k_1$ for the pseudo-first-order trap mediated (Shockley–Read–Hall) non-radiative PL decay process. From TRPL data in Figure 4c, the decay lifetime increased with the application of our surface treatment from 250 ns for the control to 560 ns, 625 ns, and 333 ns for EAI (3mg ml⁻¹), IAI (7mg ml⁻¹), and Gual (5mg ml⁻¹), respectively.

3.2.3 Photovoltaic device and performance. We examined the effect of surface passivation by ammonium salts on the photovoltaic performance for complete devices in a FTO/c-TiO₂/m-TiO₂/perovskite/spiro-OMeTAD/Au configuration (for more details see Methods). The data are shown in Figure 3.5a in comparison to a control device without

passivation (see Supplementary Table S3.1 for a comparison of all treatments with different concentrations).

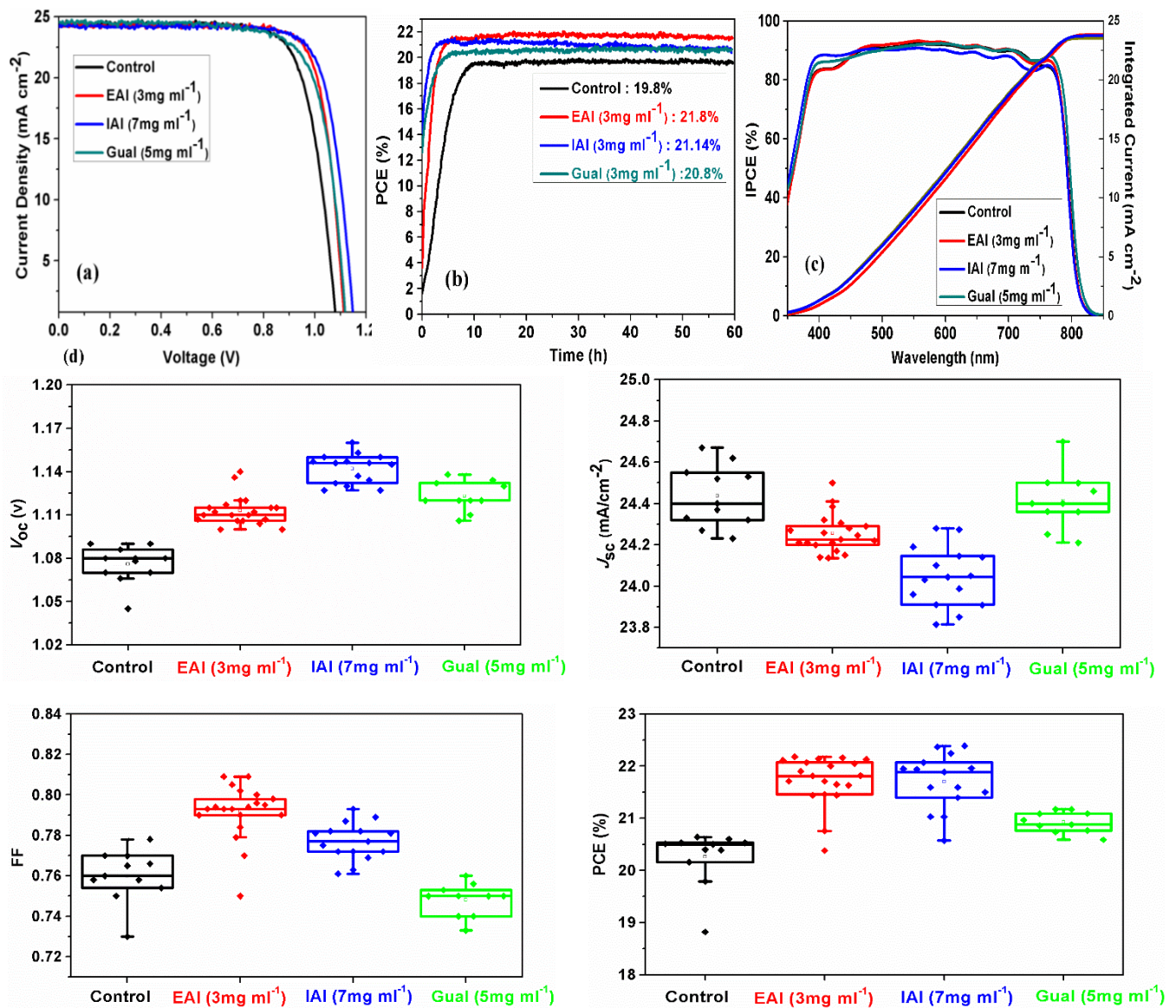


Figure 3.5: Photovoltaic characterization: a) $J-V$ curves of the devices with different passivation layers in comparison to the control device without any treatment, with a scan rate of 10 mV/s b) Maximum power tracking of the same device, c) IPCE spectra and calculated photocurrent integrated over the standard AM 1.5G solar emission.. In agreement to the $J-V$ data, no change in the spectra is observed and d) $J-V$ metrics of perovskite devices with different treatment in comparison to the control.

The open-circuit voltages of all treated devices are significantly increased with an average improvement of 30 mV, 70 mV, and 40 mV, for EAI, IAI, and GuaI, respectively (see Figure 3.5d). While the GuaI-treated devices showed an average reduction of the FF by 2% absolute, the FF increased by 3.5% and 2% for EAI and IAI-treated devices, respectively, reaching up to 81% on the best performing EAI device without significant loss of the short circuit current (J_{sc}). The short circuit photo-current densities are barely modified with a maximum average decrease of 0.4 mAcm^{-2} for the IAI-treated devices. Overall, the mean efficiency increased from 20.5% for the control device to the 22.3%, 22.1%, and 21.0% for EAI, IAI, and GuaI-treated devices, respectively, with the champion device treated via EAI achieving up to 22.3% PCE. Figure 3.5b further confirms stable power output for all treated devices during maximum power point tracking under one sun illumination for one minute. The incident photon-to-current efficiency (IPCE) and integrated current density as a function of wavelength are shown in Figure 3.5c. In agreement with UV-Vis, no shift in the onset of the IPCE spectra is detected for treated devices while integrated current densities agree well with the J_{sc} -values derived from the JV measurements. Moreover, Supplementary Figure S3.6 a-d and Supplementary Table 3.2 show that the use of these ammonium salts as surface treatment is capable of reducing the hysteresis. To further analyze the effect of these buffer layers on the electrical properties we performed intensity-modulated voltage spectroscopy (IMVS). The data shown in Supplementary Figure S3.6e agrees with the trend found for V_{oc} , i.e. the devices showing higher V_{oc} show a longer electron lifetime at V_{oc} .

3.2.4 Operational stability of perovskite solar cells. We also investigated is the operational stability of our PSCs under working conditions. This remains a major concern for PSC which needs to be urgently addressed³³. Best performing devices were subjected to full

sunlight intensity with maximum power tracking for 550 h at room temperature in a nitrogen atmosphere.

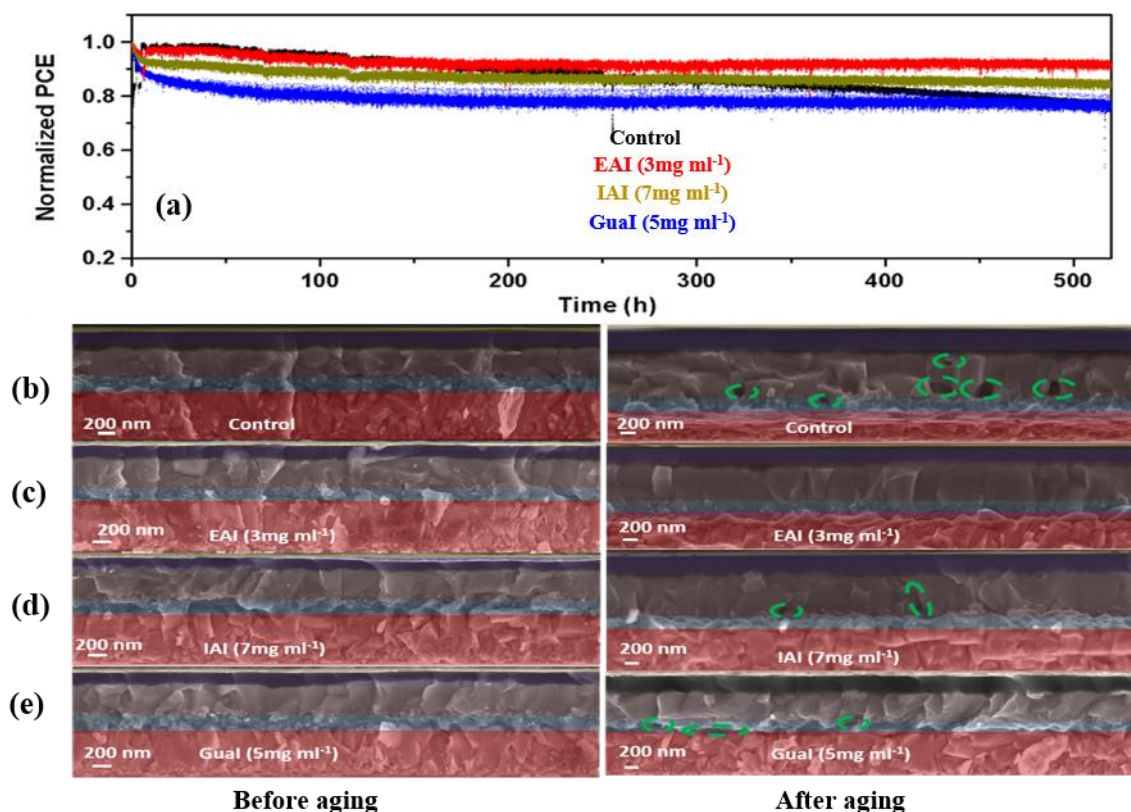


Figure 3.6. Stability data and cross-section before and after aging for control and treated devices: a) A comparison of operational stability of control and treated perovskite devices. The devices were measured under a nitrogen environment at room temperature under constant illumination (LED source, approximated 1 Sun) at a maximum power point of 550 h. b), c), d) and e) Cross-sectional SEM images of the control and modified perovskite devices before and after aging at room temperature under constant illumination (LED source, approximated 1 Sun) for 550 h. Images show perovskite absorber and covering HTL.

We note the good stability of the control device preserving 80% of its initial PCE value. This is attributed to the perovskite composition employed in this work that has an extremely low content of MAI and contains a small addition of cesium iodide (CsI) to stabilize the predominately formamidinium lead iodide perovskite phase. From Figure 3.6a, the passivated devices show a different behavior, a small initial performance drop is followed by stable power output. Remarkably for the EAI-treated device, the overall loss in PCE is only 5%. By contrast,

the control device shows a small but constant drop over the whole duration of the test. It is well-established that this behavior is due to the migration of ions from the HTM (LiTFSI) and gold from the gold electrode into the perovskite layer and to the TiO₂ working electrode³⁴. The fact that the efficiency loss for the passivated devices ceases after an initial decrease, it is reasonable to assume that the passivating layer introduces a barrier at the HTM/perovskite interface that prevents the diffusion of HTM additives and gold diffusion into the perovskite layer. From cross-sectional SEM images (Figure 3.6b-e) we can see that before aging both control and modified devices appeared to have compact absorber layers. After 550 h or MPP testing, however, the appearance of voids at the interface between the mesoporous TiO₂ and perovskite in the control and few voids also in the IAI- and GuaI-treated perovskites is visible. These voids, stemming from the degradation of the perovskite absorber, may affect the photon absorption and act as recombination centers to hinder charge carrier collection during the operation of the solar cell. Confirming this trend, EAI showed good stability at MPP under constant illumination with a decrease of only 5% and the absence of voids in the cross-section SEM image of the aged devices shown in Figure 3.6c.

3.3 Discussion

In summary, we investigated the effect of different ammonium salts (i.e. EAI, IAI, and GuaI) as surface passivation agents on mixed-cation and mixed-halide perovskite films. Solid-state NMR has evidenced that they form a tightly adhering low-dimensionality passivation layer on the preexisting perovskite grains. The introduction of these buffer layers showed a significant enhancement of the open-circuit voltage by 30 mV (EAI), 70 mV (IAI), and 40 mV (GuaI), leading to the realization of PCEs as high as 22.3%, 22.1%, and 21.0% for EAI, IAI, and GuaI-treated devices, respectively. EAI and IAI showed an improvement also on the FF (+3.5% and +2%, respectively) with EAI reaching a FF of 81% on the best performing device. In contrast

to the control sample, all passivated devices, after an initial drop, stabilized their efficiency with the EAI-treated device only losing 5% of its initial value after 550 h of MPP tracking. This work exemplifies the importance of interface engineering for perovskite solar cells and should stimulate other successful developments in the future.

3.4 Methods

3.4.1 Materials: All materials were purchased from Sigma-Aldrich and used as received unless stated otherwise.

3.4.2 Solar cell preparation: Fluorine-doped tin oxide (FTO)-glass substrates (TCO glass, NSG 10, Nippon sheet glass, Japan) were cleaned by ultrasonication in Hellmanex (2%, deionized water), rinsed thoroughly with de-ionized water and ethanol, and then treated in oxygen plasma for 15 min. 30 nm blocking layer (TiO_2) was sprayed on the cleaned FTO by at 450 °C using a commercial titanium diisopropoxide bis(acetylacetonate) solution (75% in 2-propanol, Sigma-Aldrich) diluted in anhydrous ethanol (1:9 volume ratio). A 150 nm mesoporous TiO_2 layer (diluted paste (1:6 wt. ratio) (Dyesol 30NRD: ethanol)) spin-coated at 5000 rpm for 15 s, and then sintered at 450 °C for 30 min in dry air.

Synthesis of perovskite films: The perovskite films were deposited using a single-step deposition method from the precursor solution which was prepared in Argon atmosphere and containing 1.35 M of FAI, FABr, MAI, CsI, PbI_2 and PbBr_2 in anhydrous dimethylformamide/dimethylsulphoxide (4:1 (volume ratio)) to achieve the desired composition: $\text{FA}_{0.9}\text{Cs}_{0.07}\text{MA}_{0.03}\text{Pb}(\text{I}_{0.92}\text{Br}_{0.08})_3$ (3% PbI_2 excess). The device fabrication, including the surface treatment step, was carried out inside a dry air box, under controlled atmospheric conditions with humidity <2%. Perovskite solution was spin-coated in a two-step program at 1000 and 6000 rpm, respectively. 200 μl of chlorobenzene was dropped on the spinning

substrate. This was followed by annealing the films at 150 °C for 30 to 40 min. After preparing the initial perovskite layer (control) as described above, the film was cooled down at room temperature. Then, the surface treatment was performed by spin-coating a EAI, IAI, and GuaI solution in isopropanol at different concentrations of 0mg ml⁻¹, 3mg ml⁻¹, 5mg ml⁻¹, 7mg ml⁻¹ and 10mg ml⁻¹ at 6000 rpm for 30 sec, followed by annealing at 70 °C for 10~15 min. For completing the fabrication of devices, 85 mg of 2,2',7,7'-tetrakis(*N,N*-di-*p*-methoxyphenylamine)-9,9-spirobifluorene (spiro-OMeTAD) was dissolved in 1 ml of chlorobenzene as a hole-transporting material (HTM). The HTM was spin coated at 4000 rpm for 20 s. The HTM was doped with bis(trifluoromethylsulfonyl)imide lithium salt (17.8 µl prepared by dissolving 520 mg LiTFSI in 1 ml of acetonitrile), and 28.8 µl of 4-tert-butylpyridine. Finally, a ~80 nm gold (Au) layer was thermally evaporated.

3.4.3 Device characterization: The current-voltage (*J-V*) characteristics of the perovskite devices were recorded under ambient temperature and air conditions with a digital source meter (Keithley model 2400, USA). A 450 W xenon lamp (Oriel, USA) was used as the light source for photovoltaic (*J-V*) measurements. The spectral output of the lamp was filtered using a Schott K113 Tempax sunlight filter (Präzisions Glas & Optik GmbH, Germany) to reduce the mismatch between the simulated and actual solar spectrum to less than 2%. The photo-active area of 0.16 cm² was defined using a dark-colored metal mask.

3.4.4. Incident photon-to-current efficiency (IPCE): was recorded under a constant white light bias of approximately 5 mW cm⁻² supplied by an array of white light emitting diodes. The excitation beam coming from a 300 W Xenon lamp (ILC Technology) was focused through a Gemini- 180 double monochromator (Jobin Yvon Ltd) and chopped at approximately 2 Hz. The signal was recorded using a Model SR830 DSP Lock-In Amplifier (Stanford Research Systems).

3.4.5 Scanning electron microscopy (SEM): was performed on a ZEISS Merlin HR-SEM.

3.4.6 Atomic force microscopy (AFM): AFM images were obtained using a Bruker Dimension Icon Atomic Force Microscope in tapping mode.

3.4.7 X-ray powder diffractions: were recorded on an X'Pert MPD PRO (Panalytical) equipped with a ceramic tube (Cu anode, $\lambda = 1.54060 \text{ \AA}$), a secondary graphite (002) monochromator, and a RTMS X'Celerator (Panalytical).

3.4.8 UV–Vis measurements (Uv-Vis): were performed on a Varian Cary 5.

3.4.9 Photoluminescence spectra (PL) were obtained with a Florolog 322 (Horiba Jobin Yvon Ltd) in the wavelength range from 500 nm to 850 nm by exciting at 460 nm.

3.4.10 Time-resolved photoluminescence (TRPL): was measured with a spectrometer (FluoroLog-3, Horiba) working in a time-correlated single-photon counting mode with less than ns time resolution. A picosecond pulsed diode laser head NanoLED N-670L (Horiba) emitting less than 200 ps duration pulses at 670 nm with a maximum repetition rate of 1 MHz was used as an excitation source. The measurements were carried out under ambient conditions and no change in PL was observed during the course of the measurements (several hours) indicating no appreciable decomposition.

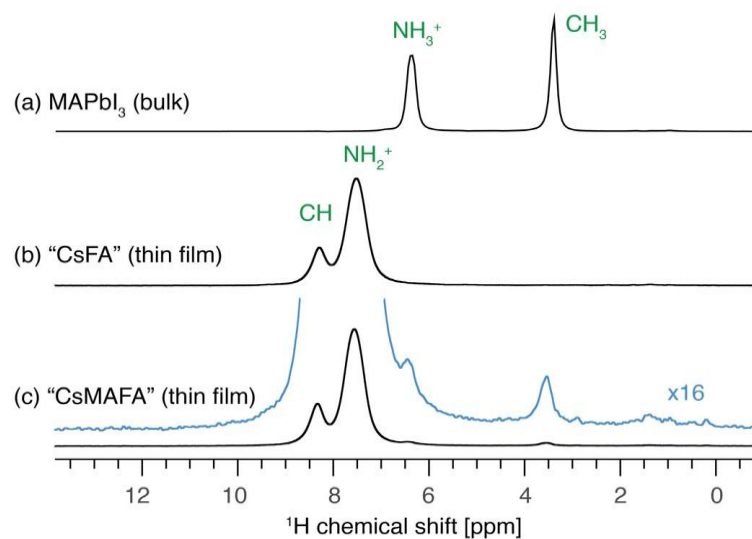
3.4.11 Solid-state NMR measurements: Room temperature ^1H (900.0 MHz) NMR spectra were recorded on a Bruker Avance Neo 21.1 T spectrometer equipped with a 3.2 mm and 1.3 mm CPMAS probe. ^1H chemical shifts were referenced to solid adamantane ($\delta=1.91$ ppm). Quantitative ^1H spectra were acquired with a recycle delay of 150 s. The CsFA and CsMAFA samples were prepared as thin films on glass slides using the same deposition technique as for PSC fabrication and scratched off the slides into a rotor. EAPbI_3 and $\text{FA}_{0.9}\text{EA}_{0.10}\text{PbI}_3$ were prepared using mechanosynthesis, according to previously published

procedures^{21,26,35-37}. ^1H - ^1H spin diffusion measurements at 20 kHz MAS were carried out using a mixing period of 50 ms and a recycle delay of 1 s ($\text{FA}_{0.90}\text{EA}_{0.10}\text{PbI}_3$). ^1H - ^1H spin diffusion measurements at 60 kHz MAS used a mixing period of 4 s and a recycle delay of 3 s ($\text{CsFA}(\text{I})$ thin-film).

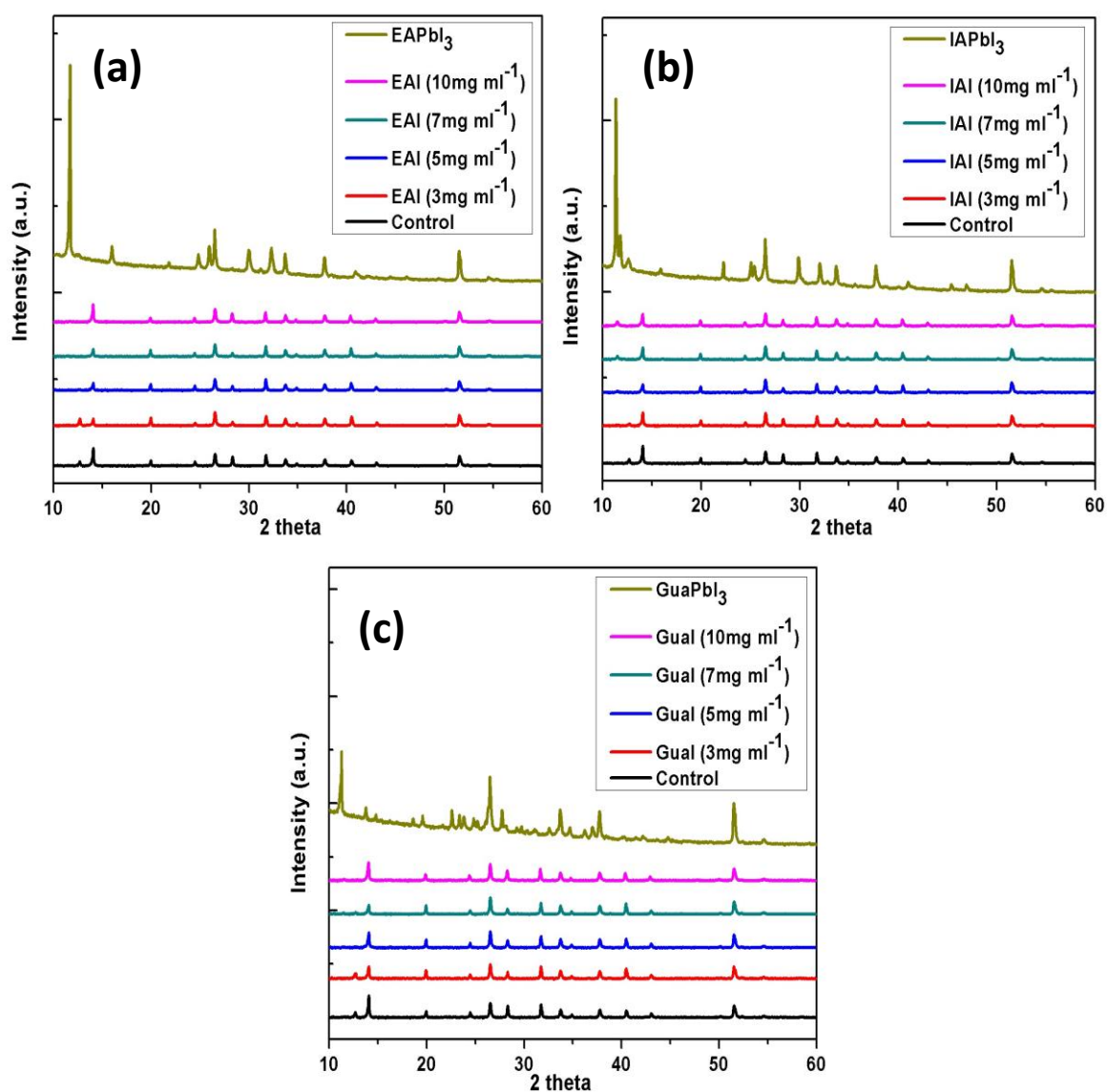
3.4.12 IMVS measurements: were performed by Bio-Logic SP300 in combination with the Galvano Staircase Spectroscopy routine from EC-Lab Software. Further description of the technique is provided in Supplementary Note 2.

3.4.13 Long-term light soaking test: Stability measurements were performed with a Biologic MPG2 potentiostat under a full AM 1.5 Sun-equivalent white LED lamp. The devices were measured with a maximum power point (MPP) tracking routine under continuous illumination at room temperature. The MPP was updated every 10 s by a standard perturb and observe method. Every minute a *JV* curve was recorded in order to track the evolution of individual *JV* parameters.

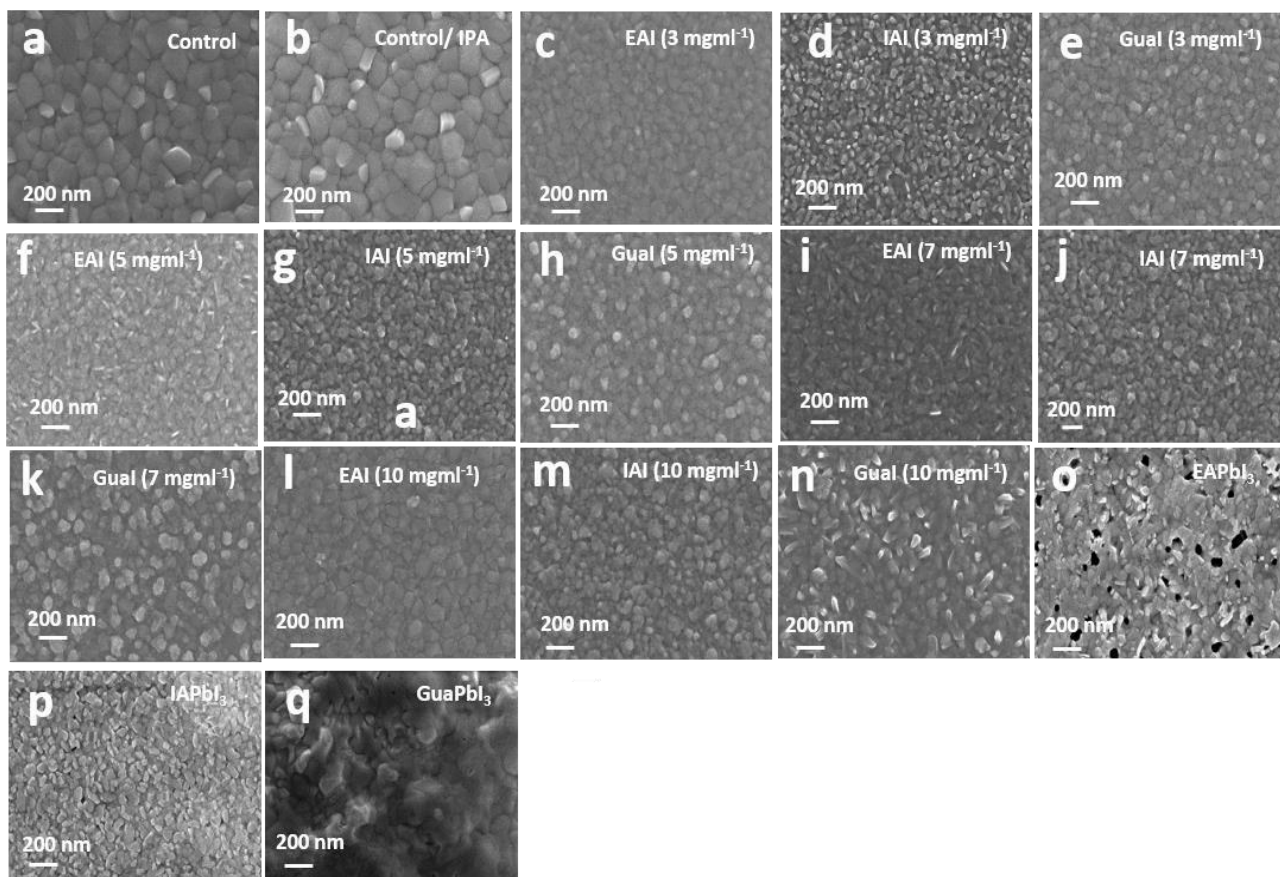
3.5 Supporting information



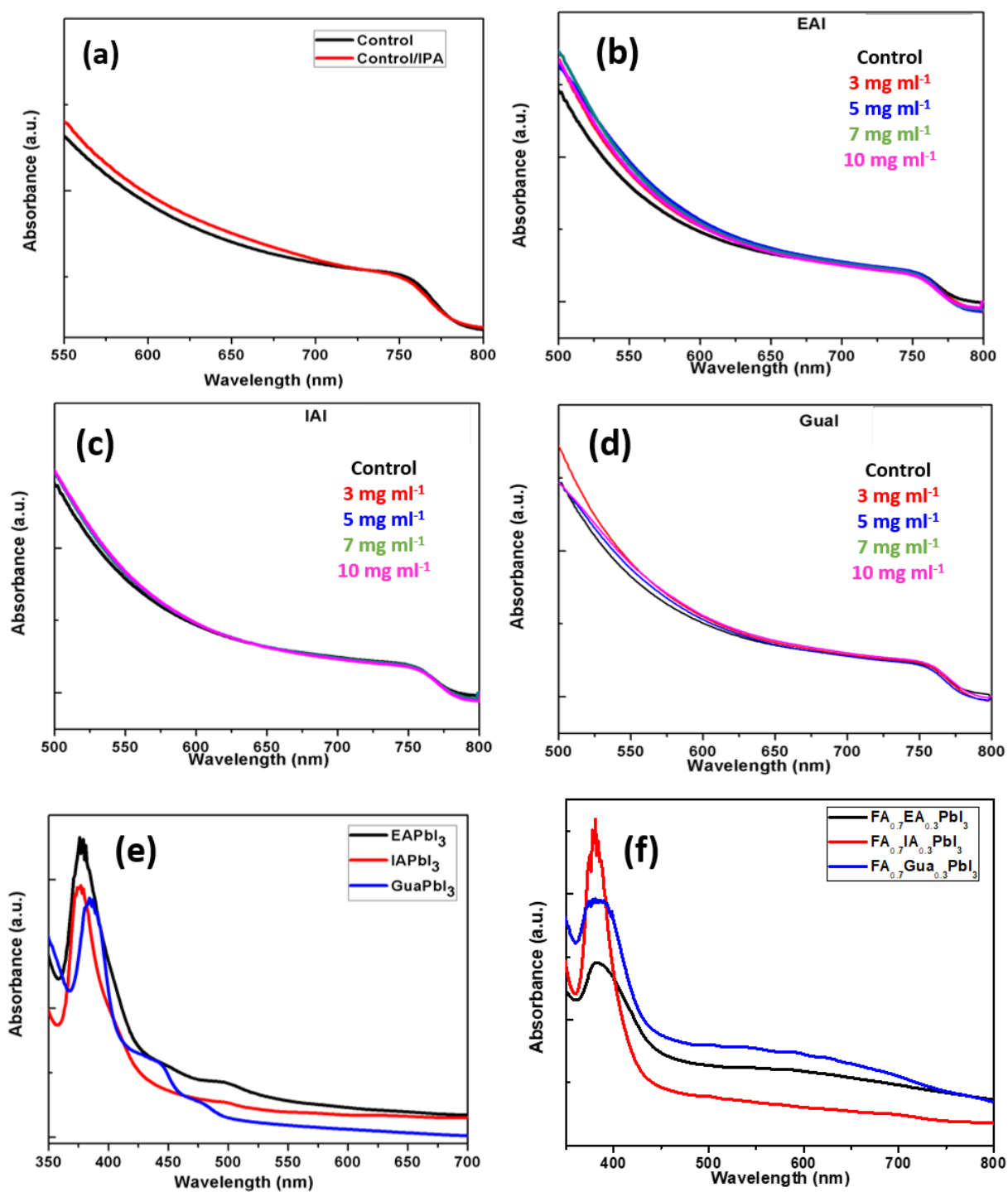
Supplementary Figure S3.1. ^1H solid-state MAS NMR spectra at 21.1 T, 298 K and 20 kHz MAS of (a) bulk mechanochemical MAPbI₃, (b) the $\text{FA}_{0.93}\text{Cs}_{0.07}\text{Pb}(\text{I}_{0.92}\text{Br}_{0.08})_3$ ("CsFA(I,Br)") composition prepared as a thin film, (c) the $\text{FA}_{0.9}\text{Cs}_{0.07}\text{MA}_{0.03}\text{Pb}(\text{I}_{0.92}\text{Br}_{0.08})_3$ ("CsMAFA") composition prepared as a thin film (bottom: normalized intensity, top: intensity multiplied by 16 to evidence the MA signals).



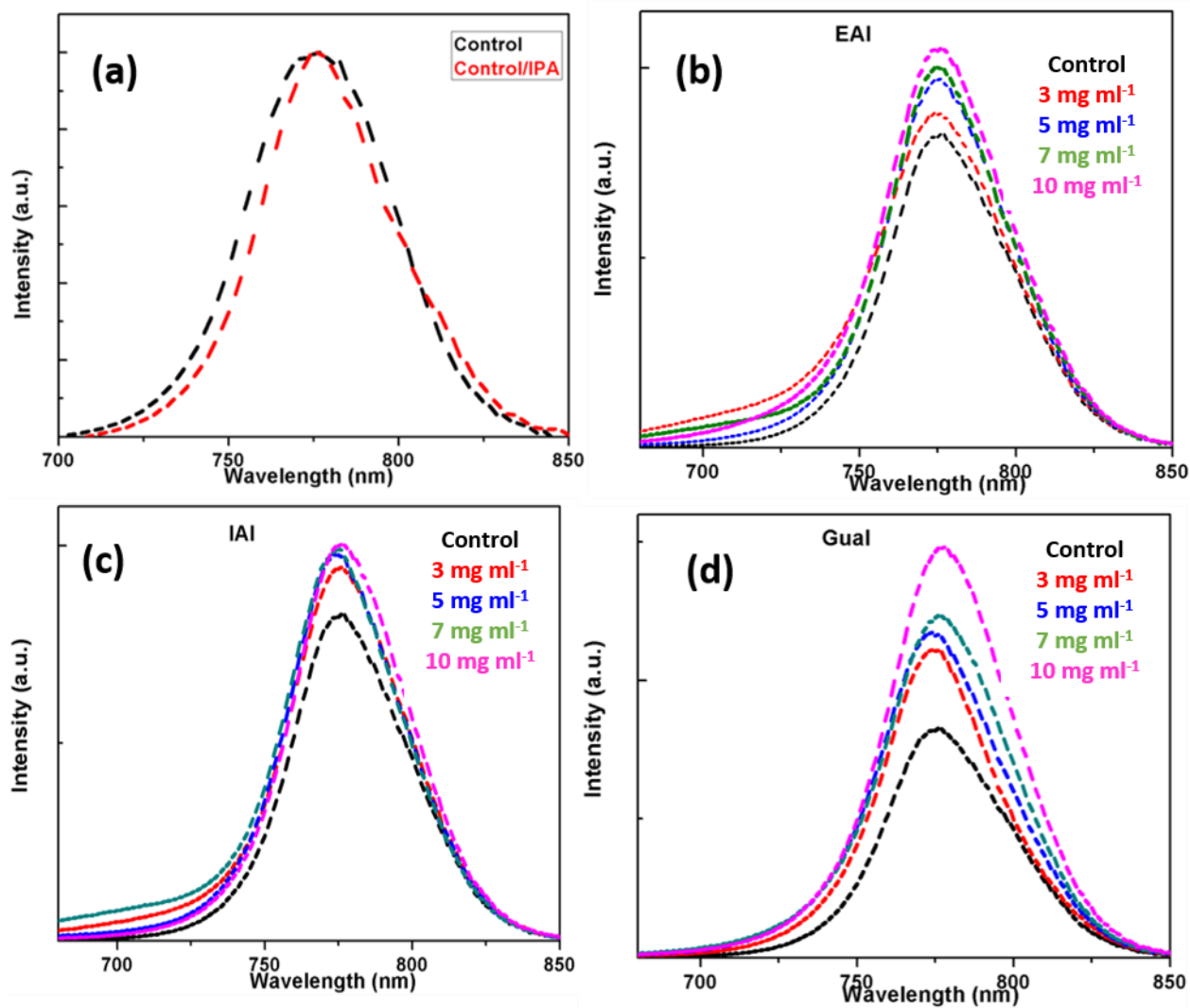
Supplementary Figure S3.2. XRD patterns of a) EAI, b) IAI and c) Gual (Control film and EAPbI₃, IAPb₃, and GuaPbI₃ including with each accordingly).



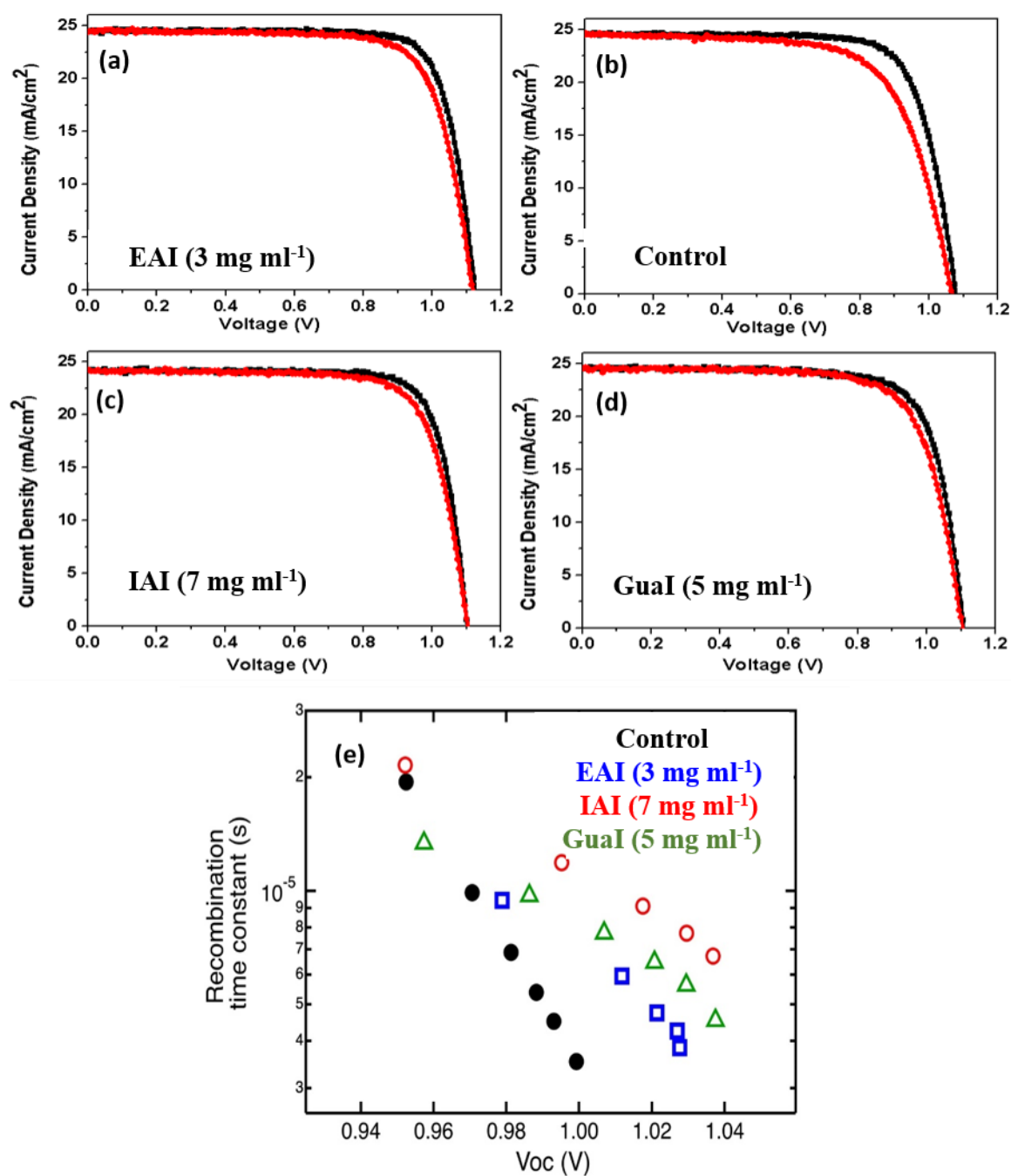
Supplementary Figure S3.3. Top view SEM micrographs of Control, EAI, IAI and Gual respectively, at different concentration (from 0-10 mg/ml) and EAPbI₃, IAPb₃ and GuaPbI₃.



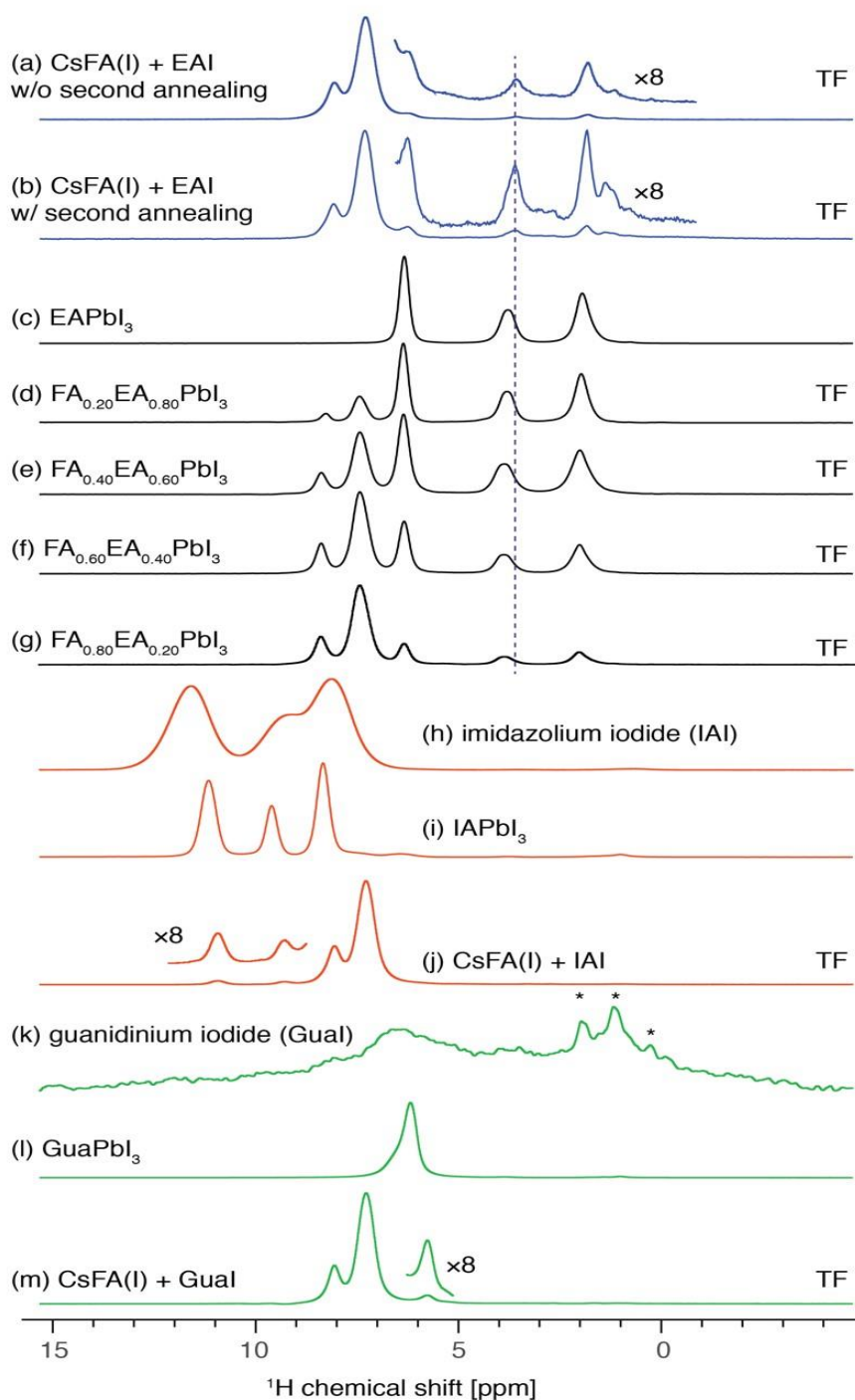
Supplementary Figure S3.4. A comparison of UV-Vis of a)Control/IPA b) EAI, c) IAI, d) Gual, e) EAPbI₃, IAPbI₃ and GuaPbI₃ and (f) FA_{0.70}X_{0.30}PbI₃ (X=EAI, IAI and Gual).



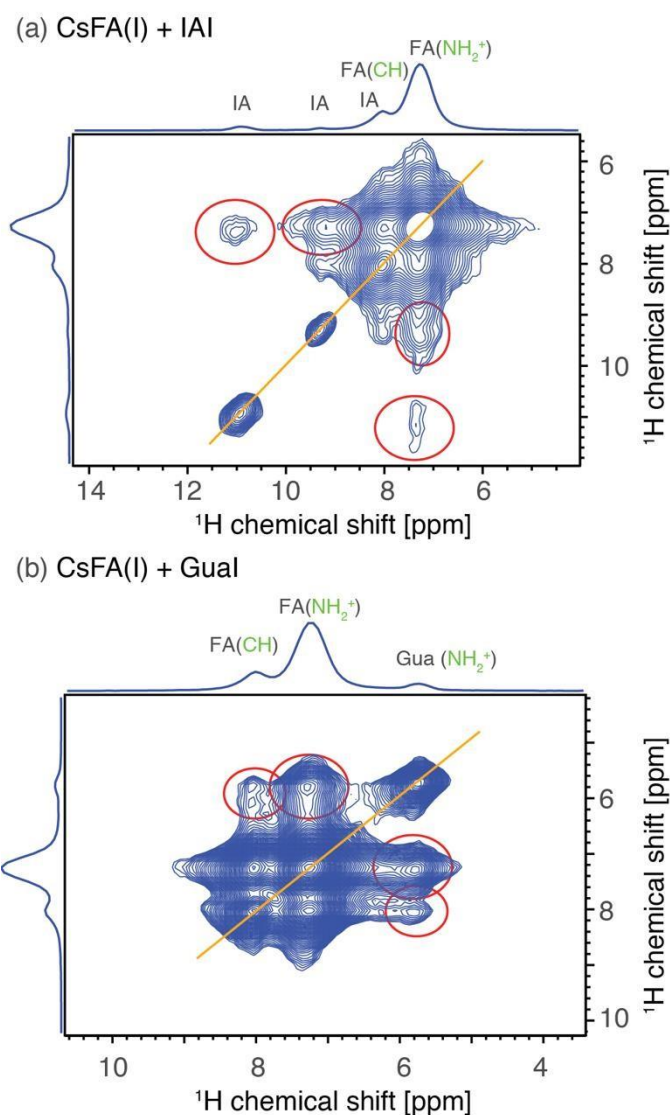
Supplementary Figure S3.5. Photoluminescence studies of a) Control/IPA b) EAI, c) IAI and d) Gual.



Supplementary Figure S3.6: Forward (black) and reverse scans (red) for a) control, and b) EAI, c) IAI, and d) Gual modified devices with a scan rate of 10 mV/s, (e) Recombination time constants for various solar cells with and without surface treatments.



Supplementary Figure S3.7. ¹H solid-state MAS NMR spectra at 21.1 T, 298 K and 20 kHz MAS of bulk mechanochemical perovskite powders and thin films (indicated as “TF”). FA_{0.93}Cs_{0.07}PbI₃ thin film treated with 5 mg/ml EAI (a) without the second annealing step, (b) with the second annealing step. FA_{1-x}EA_xPbI₃ phases: (c) x=1.00 (bulk mechanochemical EAPbI₃), (d) x=0.80 (thin film), (e) x=0.60 (thin film), (f) x=0.40 (thin film), (g) x=0.20 (thin film), (h) neat imidazolium iodide, (i) imidazolium lead iodide, (j) FA_{0.93}Cs_{0.07}PbI₃ thin film treated with 7 mgml⁻¹ IAI, (k) neat guanidinium iodide, (l) guanidinium lead iodide, (m) FA_{0.93}Cs_{0.07}PbI₃ thin film treated with 5 mgml⁻¹ Gual.



Supplementary Figure S3.8. ^1H solid-state MAS NMR spectra at 21.1 T, 298 K and 20 kHz MAS. ^1H - ^1H spin diffusion experiments evidencing atomic-level proximity between FA, IAI and Gual in a $\text{FA}_{0.93}\text{Cs}_{0.07}\text{PbI}_3$ thin film treated with (a) 7 mg/ml IAI (FA/IAI cross-peaks in red circles) and (b) 5 mg/ml¹ Gual (FA/Gual cross-peaks in red circles).

Supplementary Table S3.1. Summarized *J-V* characteristics of the best devices with varying EAI, IAI and Gual contents in comparison to the control device:

| | V _{oc} (V) | J _{sc} (mA/cm ²) | FF (%) | PCE (%) |
|---|---------------------|---------------------------------------|-------------|--------------|
| Control | 1.08 | 24.50 | 76 | 20.52 |
| Control/IPA | 1.10 | 23.96 | 76 | 20.44 |
| EAI | | | | |
| 3 mg ml⁻¹ | 1.12 | 24.14 | 81 | 22.40 |
| 5 mg ml⁻¹ | 1.15 | 24.60 | 77 | 22.23 |
| 7 mg ml⁻¹ | 1.15 | 23.50 | 68 | 18.75 |
| 10 mg ml⁻¹ | 1.17 | 23.00 | 63 | 17.30 |
| IAI | | | | |
| 3 mg ml⁻¹ | 1.12 | 24.29 | 77 | 21.40 |
| 5 mg ml⁻¹ | 1.13 | 24.03 | 79 | 21.90 |
| 7 mg ml⁻¹ | 1.15 | 23.85 | 79 | 22.11 |
| 10 mg ml⁻¹ | 1.16 | 23.40 | 74 | 20.50 |
| Gual | | | | |
| 3 mg ml⁻¹ | 1.10 | 24.46 | 76 | 20.68 |
| 5 mg ml⁻¹ | 1.12 | 24.50 | 75 | 21.00 |
| 7 mg ml⁻¹ | 1.14 | 23.72 | 71 | 19.60 |
| 10 mg ml⁻¹ | 1.16 | 23.00 | 70 | 19.06 |
| Mixed Cation | | | | |
| EAI (mg ml⁻¹)/IAI (7 mg ml⁻¹) | | | | |
| | 1.14 | 21.97 | 0.71 | 18.1 |
| EAI (3 mg ml⁻¹)/Gual (7 mg ml⁻¹) | | | | |
| | 1.11 | 22.09 | 0.60 | 14.8 |

Supplementary Table S3.2. Summarized J-V characteristics of the devices at forward and reverse scans at scan rate 10 mV/s⁻¹ with varying EAI, IAI and Gual contents in comparison to the control device:

| | Scan direction | J _{sc} (mA/Cm ²) | V _{oc} (V) | FF(%) | PCE(%) |
|------------------------------------|----------------|---------------------------------------|---------------------|-------------|---------------|
| Control | Forward | 24.32 | 1.063 | 70.3 | 18.54 |
| | Backward | 24.38 | 1.071 | 77.8 | 20.72 |
| EAI (3 mg ml⁻¹) | Forward | 24.35 | 1.117 | 76.4 | 21.20 |
| | Backward | 24.36 | 1.123 | 80.4 | 22.30 |
| IAI (7 mg ml⁻¹) | Forward | 24.23 | 1.102 | 75.2 | 20.50- |
| | Backward | 24.14 | 1.103 | 79.4 | 21.60 |
| Gual (5 mg ml⁻¹) | Forward | 24.39 | 1.102 | 72.3 | 20.03 |
| | Backward | 24.45 | 1.106 | 75.3 | 20.90 |

Supplementary Note 3.1: We have recently shown that solid-state magic angle spinning (MAS) NMR can be used to probe the atomic-level microstructure of multi-component lead halide perovskites [21] [26] [36] [37]. In particular, high-resolution ^1H NMR makes it possible to quantify the amount of organic cations in the final solid perovskite material. In order to establish whether or not annealing at 150 °C leads to evaporation of MA from the “CsMAFA” thin films, we have carried out ^1H solid-state MAS NMR measurements on the material prepared as a thin film (fig. S6). The reference ^1H spectrum of bulk mechanochemical MAPbI_3 exhibits two signals corresponding to the CH_3 (3.40 ppm) and NH_3^+ (6.38 ppm) groups of the MA cation (fig. 1a) while the “CsFA” material prepared as a thin film exhibits two signals corresponding to the CH (8.30 ppm) and NH_2^+ (7.53 ppm) groups of the FA cation. The “CsMAFA” composition exhibits two sets of signals, corresponding to FA (8.34 and 7.58 ppm) and MA (6.44 and 3.54 ppm). Quantification of the corresponding resonances yields 0.97 mol % FA and 0.03 mol % MA which is in perfect agreement with the stoichiometry of the precursor solution, indicating that MA is fully preserved in the final perovskite composition despite the relatively high annealing temperature.

Supplementary Note 3.2: quantification of the passivation layer thickness.

The thickness of the 1D passivation layer can be quantified based on the quantitative ^1H MAS NMR spectrum of $(\text{CH}_5\text{N}_2)_{0.93}\text{Cs}_{0.07}\text{PbI}_3$ and simple geometrical considerations.

Perovskite layer thickness: 350 nm

Passivation layer thickness: 27 nm (by NMR), as detailed below.

Film dimensions: 2.5 cm x 1.75 cm (identical for both layers, this dimension will reduce in the final result)

Material density: 4.2 g/cm^3 (value for $\alpha\text{-FAPbI}_3$)

Perovskite volume: $350 \text{ nm} * 2.5 \text{ cm} * 1.75 \text{ cm} = 1.53125 \times 10^{-7} \text{ dm}^3$

Perovskite mass: 0.643 mg

Perovskite molecular weight: 639 g/mol (where H: 4.7 g/mol)

Perovskite number of moles: $1.006 \text{ } \mu\text{mol}$ (where H: μmol)

Integrals in the quantitative ^1H NMR spectrum of $(\text{CH}_5\text{N}_2)_{0.93}\text{Cs}_{0.07}\text{PbI}_3$ passivated with 5 mg/ml EAI:

$(\text{CH}_5\text{N}_2)_{0.93}\text{Cs}_{0.07}\text{PbI}_3$: 0.90 --- corresponding to ---

$0.0074 \text{ } \mu\text{mol}$ EAPbI₃ ($\text{C}_2\text{H}_8\text{NPbI}_3$): 0.10 ---

corresponding to --- x mol x = $0.00082 \text{ } \mu\text{mol}$ of
hydrogen in the 1D passivation layer.

EAPbI₃ molecular weight: 634 g/mol (where H: 8 g/mol)

Number of moles of EAPbI₃ in the film: $0.00082 \text{ } \mu\text{mol} / (8/634) = 0.06499 \text{ } \mu\text{mol}$

Mass of EAPbI₃ in the film: $0.06499 \text{ } \mu\text{mol} * 634 \text{ g/mol} = 41.2 \text{ } \mu\text{g}$

Taking density of EAPbI₃ as $d=3.5 \text{ g/cm}^3$ (typical value for 1D haloplumbate phases, cf. e.g. APL Materials, **2018**, 6, 114202, DOI: 10.1063/1.5046404) this yields the volume of the passivation layer: $1.17714286 \times 10^{-8} \text{ dm}^3$. Dividing by the film dimensions ($2.5 \text{ cm} * 1.75 \text{ cm} = 0.0004375 \text{ m}^2$), **the passivation layer thickness is: 27 nm.**

Supplementary Note 3.3: Description of Intensity Modulated Photovoltage Spectroscopy (IMVS)

Intensity Modulated Photovoltage Spectroscopy is an optoelectronic technique extremely useful in Solar cell technology to measure recombination time constants inside a device. The technique makes use of a potentiostat equipped with frequency response analyzer and an LED for stimulating the device under test (DUT). The potentiostat controls and monitors the LED and the Solar Cell, respectively.

The solar cell is at open circuit and is illuminated by the LED at a bias constant light. The LED is controlled in Galvanostatic mode at different bias currents. A small-amplitude sinusoidal current stimulus is added on top of the bias current sourcing the LED. The frequency of the sinusoidal stimulus is varied, thus probing the frequency response of the DUT for a defined spectral range.

The bias light defines the V_{oc} of the device and therefore the working point around which the small amplitude Voltage frequency response of the DUT is measured.

The transfer function is a complex function whose Imaginary and Real parts can be expressed as a function of frequency.

The Lifetime of the carriers τ inside the DUT is related to the frequency corresponding to the peak of the imaginary part by the following equation: $\tau = (2\pi f_{min})^{-1}$.

3.6 References

1. Burschka, J. *et al.* Sequential deposition as a route to high-performance perovskite-sensitized solar cells. *Nature* **499**, 316–319 (2013).
2. Saliba, M. *et al.* Cesium-containing triple cation perovskite solar cells: improved stability, reproducibility and high efficiency. *Energy Environ. Sci.* **9**, 1989–1997 (2016).
3. Park, N.-G., Gratzel, M., Miyasaka, T., Zhu, K. & Emery, K. Towards stable and commercially available perovskite solar cells. *Nat. Energy* **1**, 16152 (2016).
4. Tsai, H. *et al.* High-efficiency two-dimensional Ruddlesden–Popper perovskite solar cells. *Nature* **536**, 312–316 (2016).
5. Bi, D. *et al.* Efficient luminescent solar cells based on tailored mixed-cation perovskites. *Sci. Adv.* **2**, e1501170–e1501170 (2016).
6. chart, NREL. http://www.nrel.gov/ncpv/images/efficiency_chart.jpg. (2019).
7. Zheng, X. *et al.* Defect passivation in hybrid perovskite solar cells using quaternary ammonium halide anions and cations. *Nat. Energy* **2**, 17102–9 (2017).
8. Dar, M. I. *et al.* Function Follows Form: Correlation between the Growth and Local Emission of Perovskite Structures and the Performance of Solar Cells. *Adv. Funct. Mater.* **27**, 1701433–9 (2017).
9. Dualah, A. *et al.* Impedance Spectroscopic Analysis of Lead Iodide Perovskite-Sensitized Solid-State Solar Cells. *ACS Nano* **8**, 362–373 (2013).
10. Arora, N. *et al.* Intrinsic and Extrinsic Stability of Formamidinium Lead Bromide Perovskite Solar Cells Yielding High Photovoltage. *Nano Lett.* **16**, 7155–7162 (2016).
11. Chen, J., Seo, J.-Y. & Park, N.-G. Simultaneous Improvement of Photovoltaic Performance and Stability by In Situ Formation of 2D Perovskite at (FAPbI₃)_{0.88}(CsPbBr₃)_{0.12}/CuSCN Interface. *Adv. Energy Mater.* **8**, 1702714–15 (2018).
12. R. J. S. *et al.* Enhancing Defect Tolerance and Phase Stability of High-Bandgap Perovskites via Guanidinium Alloying. *ACS Energy Lett.* **3**, 1261–1268 (2018).
13. Cho, K. T. *et al.* Highly efficient perovskite solar cells with a compositionally engineered perovskite/hole transporting material interface. *Energy Environ. Sci.* **10**, 621–627 (2017).
14. Hawash, Z. *et al.* Interfacial Modification of Perovskite Solar Cells Using an Ultrathin MAI Layer Leads to Enhanced Energy Level Alignment, Efficiencies, and Reproducibility. *J. Phys. Chem. Lett.* **8**, 3947–3953 (2017).

15. Wang, F. *et al.* Phenylalkylamine Passivation of Organolead Halide Perovskites Enabling High-Efficiency and Air-Stable Photovoltaic Cells. *Adv. Mater.* **28**, 9986–9992 (2016).
16. Han, G. *et al.* Additive Selection Strategy for High Performance Perovskite Photovoltaics. *J. Phys. Chem. C* **122**, 13884–13893 (2018).
17. Wang, Q., Dong, Q., Li, T., Gruverman, A. & Huang, J. Thin Insulating Tunneling Contacts for Efficient and Water-Resistant Perovskite Solar Cells. *Adv. Mater.* **28**, 6734–6739 (2016).
18. De Marco, N. *et al.* Guanidinium: A Route to Enhanced Carrier Lifetime and Open-Circuit Voltage in Hybrid Perovskite Solar Cells. *Nano Lett.* **16**, 1009–1016 (2016).
19. Hou, X. *et al.* Effect of guanidinium on mesoscopic perovskite solar cells. *J. Mater. Chem. A* **5**, 73–78 (2017).
20. Jodlowski, A. D. *et al.* Large guanidinium cation mixed with methylammonium in lead iodide perovskites for 19% efficient solar cells. *Nat. Energy* 1–8 (2017).
21. Kubicki, D. J. *et al.* Formation of Stable Mixed Guanidinium–Methylammonium Phases with Exceptionally Long Carrier Lifetimes for High-Efficiency Lead Iodide-Based Perovskite Photovoltaics. *J. Am. Chem. Soc.* **140**, 3345–3351 (2018).
22. Hsu, H.-L. *et al.* High-performance and high-durability perovskite photovoltaic devices prepared using ethylammonium iodide as an additive. *J. Mater. Chem. A* **3**, 9271–9277 (2015).
23. Poorkazem, K. & Kelly, T. L. Compositional Engineering To Improve the Stability of Lead Halide Perovskites: A Comparative Study of Cationic and Anionic Dopants. *ACS Appl. Energy Mater.* **1**, 181–190 (2017).
24. Wang, Q. *et al.* Enhancing efficiency of perovskite solar cells by reducing defects through imidazolium cation incorporation. *Mater. Today Energy* **7**, 161–168 (2018).
25. Zhang, Y. *et al.* Auto-passivation of crystal defects in hybrid imidazolium/methylammonium lead iodide films by fumigation with methylamine affords high efficiency perovskite solar cells. *Nano Energy* **58**, 105–111 (2019).
26. Kubicki, D. J. *et al.* Cation Dynamics in Mixed-Cation (MA) x (FA) $1-x$ PbI₃ Hybrid Perovskites from Solid-State NMR. *J. Am. Chem. Soc.* **139**, 10055–10061 (2017).
27. Tavakoli, M. M. *et al.* Adamantanes Enhance the Photovoltaic Performance and Operational Stability of Perovskite Solar Cells by Effective Mitigation of Interfacial Defect States. *Adv. Energy Mater.* **8**, 1800275–7 (2018).

28. Bi, D. *et al.* Multifunctional molecular modulators for perovskite solar cells with over 20% efficiency and high operational stability. *Nat. Comms.* 1–10 (2018).
29. Jeong-Hyeok Im, Jaehoon Chung, Seung-Joo Kim and Nam-Gyu Park, Synthesis, structure, and photovoltaic property of a nanocrystalline 2H perovskite-type novel sensitizer (CH₃CH₂NH₃)PbI₃ *Nanoscale res. lett.* 7:353, (2012).
30. Fan, J. *et al.* Thermodynamically Self-Healing 1D-3D Hybrid Perovskite Solar Cells. *Adv. Energy Mater.* **8**, 1703421–8 (2018).
31. Chen, Y. *et al.* 2D Ruddlesden-Popper Perovskites for Optoelectronics. *Adv. Mater.* **30**, 1703487–15 (2017).
32. Elena, B., Pintacuda, G., Mifsud, N. & Emsley, L. Molecular Structure Determination in Powders by NMR Crystallography from Proton Spin Diffusion. *J. Am. Chem. Soc.* **128**, 9555–9560 (2006).
33. Domanski, K., Alharbi, E. A., Hagfeldt, A., Gratzel, M. & Tress, W. Systematic investigation of the impact of operation conditions on the degradation behaviour of perovskite solar cells. *Nat. Energy* 1–7 (2018).
34. Domanski, K. *et al.* Not All That Glitters Is Gold: Metal-Migration-Induced Degradation in Perovskite Solar Cells. *ACS Nano* **10**, 6306–6314 (2016).
35. Prochowicz, D. *et al.* Mechano-synthesis of the hybrid perovskite CH₃NH₃PbI₃: characterization and the corresponding solar cell efficiency. *J. Mater. Chem. A* **3**, 20772–20777 (2015).
36. Kubicki, D. J. *et al.* Phase Segregation in Cs-, Rb- and K-Doped Mixed-Cation (MA)_x(FA)_{1–x}PbI₃ Hybrid Perovskites from Solid-State NMR. *J. Am. Chem. Soc.* **139**, 14173–14180 (2017).
37. Kubicki, D. J. *et al.* Phase Segregation in Potassium-Doped Lead Halide Perovskites from ³⁹K Solid-State NMR at 21.1 T. *J. Am. Chem. Soc.* **140**, 7232–7238 (2018).

Chapter 4.

Methylammonium triiodide for holistic defect engineering of α -FAPbI₃ perovskite solar cells

This work has been Submitted.

4.1 Introduction

Metal halide perovskites have emerged as one of the most attractive light-harvesting materials for next-generation solar cells. Within a decade of the first report, the certified power conversion efficiency (PCE) of perovskite solar cells (PSCs) has reached as high as 25.5%¹⁻⁴. However, before bringing PSCs to an industrial scale-up process and using perovskites in other optoelectronic applications, some critical issues need to be carefully addressed, such as Pb and solvent toxicities, and, most importantly, the intrinsic material and device instability. Lattice defects have been identified as one of the main sources of instability and performance loss via charge recombination through non-radiative channels^{5,6}. Perovskite crystals, in particular, FAPbI₃ contain several types of point defects such as interstitials (FA_i, Pb_i, I_i), vacancies (V_{FA}, V_{Pb}, V_I) antisites (FA_{Pb}, Pb_{FA}, FA_I, Pb_I, I_{FA}, I_{Pb}), grain boundaries, and mobile ions which have been identified as predominant sources for non-radiative recombination⁷. Most of these point defects only result in shallow traps or tail states; however, the ionic nature of hybrid perovskites leads to a large population of mobile ions. The vacancies, in particular iodide vacancies, provide a diffusion pathway for halide ions. In particular, iodide migrates to perovskite interfaces under an electric field, thus compromising photovoltaic performance and long-term operational stability. Apart from point defects, perovskite crystals also contain undercoordinated Pb²⁺ and lattice I⁻ ions susceptible to reduction and oxidation (redox) reactions, respectively⁸. The reduction of undercoordinated Pb²⁺ leads to metallic Pb (Pb⁰)

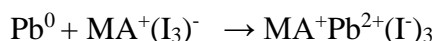
which critically acts as a center for non-radiative recombination and source of degradation. Lattice I^- ions can be oxidized by hole trapping to interstitial I^0 , which can cause irreversible decomposition of the perovskite by dimerizing to volatile I_2 triggering the perovskite degradation⁹. Therefore, it is imperative to suppress these deleterious reaction channels. The ionic nature of the perovskite lattice allows for the molecular passivation of these defects. Various strategies, such as compositional engineering^{10–13}, iodine management, 2D/3D perovskite heterostructures^{14,15}, bulk, and surface/interface passivation via small organic molecules¹⁶, ammonium salts¹⁷, and ionic additives¹⁸ have been used for defect mitigation. Nevertheless, there are ongoing efforts to develop novel facile defect passivation strategies as well as to improve our fundamental understanding of the mechanisms involved.

Herein, we investigate methylammonium triiodide (MAI_3) as an additive for holistic defect mitigation in a perovskite semiconductor. MAI_3 has a low melting point and large dipole moment and a cation bearing an ammonium head group,, which allows it to form numerous H-bonds for ensuring strong interaction with anions, as well as neutralizing charged vacancies¹⁹. Our results show that MAI_3 passivates a combination of defects such as A-site vacancies, halide vacancies, and Pb^0 clusters. As a result, perovskite solar cells treated with MAI_3 exhibit reduced non-radiative recombination and improved charge transport, leading to stabilized PCEs of over 23% with a high fill factor (FF) of over 80% and improved device stability under different stress conditions.

4.2 Results and discussion

We employ a perovskite with FAPbI₃ rich composition of (FAPbI₃)_{0.98}(MAPbBr₃)_{0.02}, (FA⁺ = formamidinium = CH(NH₂)₂⁺; MA⁺ = methylammonium = CH₃NH₃⁺). The additives were added to the perovskite precursor solution and perovskite films were deposited by spin-coating onto the mesoporous TiO₂ (mp-TiO₂) layer by a one-step method using chlorobenzene as antisolvent. To begin with, we prepared the additive solutions of I₂, MAI, and MAI+I₂ by dissolving them in isopropyl alcohol (IPA) at 60 °C. We recorded the absorption spectra as a function of time (Figure S 4.1a,b,c). In the case of the mixture of MAI and I₂, we observed two absorption bands at 291 nm and 358 nm immediately after preparation which corresponds to I₃⁻²⁰, thus confirming the formation of methylammonium triiodide (MAI₃). Furthermore, these absorption bands did not change with time, and no other bands appeared as shown in Figure S1a,b,c. In the case of iodine (I₂) dissolved in IPA, we observe the formation of triiodide as confirmed by weak absorption bands at 291 nm and 358 nm, and an additional absorption peak related to I₂, at 443 nm. After 72h and 220h, the formation of I₃⁻ becomes clearer, however, the absorption band relating to I₂ at 443 nm was still observed (Figure S4.1a,b,c). Thus, it is evident that a mixture of MAI+I₂ in IPA leads to the formation of a stable MAI₃ solution whereas I₂ in IPA results in a mixture of I₃⁻ and I₂. Typically, due to the soft nature of the perovskite material, in particular, the weak bond of Pb-I, metallic lead (Pb⁰), and iodine (I⁰) can be easily formed which are known as a source of recombination and degradation⁸. We hypothesize that MAI₃ can stop the formation Pb⁰, and therefore reduce this degradation. To verify our hypothesis, we performed X-ray photoelectron spectroscopy (XPS) of pristine perovskite and with the additives of I₂(I₃), MAI, and MAI+I₂(MAI₃). We observe the formation of Pb⁰ in the pristine perovskite (control) and the perovskite with MAI and I₃ as additives, while there was no presence of Pb⁰ in the perovskite with MAI₃ as shown in Figure 4.1a,b,c. This confirms that the MAI₃ additive completely reacted with the Pb⁰, which is a well-

known source of non-radiative recombination and degradation. To further verify our hypothesis, we performed density functional theory (DFT) calculations to investigate possible reactions occurring when MAI₃ approaches a slab of FAPbI₃ containing a cluster of three surface defects namely two halide vacancies sharing a common neighboring metallic Pb. Formally, such a Pb has oxidation state 0 serving as suitable starting point for a formal redox reaction of the kind:



A simple energetic estimate (SI) based on the involved ionisation energies, electron affinities, and dissociation energies with respect to the lattice energy predicts that such a reaction is highly exothermic.

In fact, we find that when the MAI₃ approaches the surface from different starting configurations within a distance of 3.0 – 3.5 Å to the halide vacancies, it invariably dissociates with simultaneous incorporation of iodides into the vacant anion sites and a third I⁻ coordinating to an undercoordinated Pb ion at the surface (Figure 4.1b). In the gas phase, this process is calculated to be exothermic by about -5eV per stoichiometric unit. In order to assess the underlying redox character, we computed Bader charges on reactants and products (SI) demonstrating indeed that a significant transfer of electronic charge from the Pb atoms of the surface to the I₃⁻ occurs. Therefore, we conclude that MAI₃ can be fully converted to perovskite with the simultaneous elimination of notorious Pb⁰ defects as well as iodide and MA⁺ vacancies. We carried out a systematic investigation on the effect of these additives (MAI₃, MAI, and I₃⁻) (see methods for more information) on the photovoltaic performance. We fabricated solar cells with *n-i-p* architecture. The champion device using (I₂) I₃⁻ showed a PCE of 21.43% with a J_{SC} of 25.20 mA·cm⁻², a V_{oc} of 1.05 V and FF of 79.5% and while using MAI as an additive produced a PCE of 21.08% with a J_{SC} of 25.03 mA·cm⁻², a V_{oc} of 1.08 V and FF

of 77.0%. In contrast, the MAI₃ showed a dramatic improvement with champion PCE of 23.46%, a J_{SC} of 25.20 mA·cm⁻², and a clear improvement in the V_{oc} and FF to 1.13 V and 81.4% respectively. In comparison, the control device showed a PCE of 20.32% with a J_{SC} of 25.06 mA·cm⁻², a V_{oc} of 1.04 V, and FF of 76.7% as shown in Figure 1c. The photovoltaic results and data are shown and summarized in Figure S4.2a,b,c, and Table S4.1.

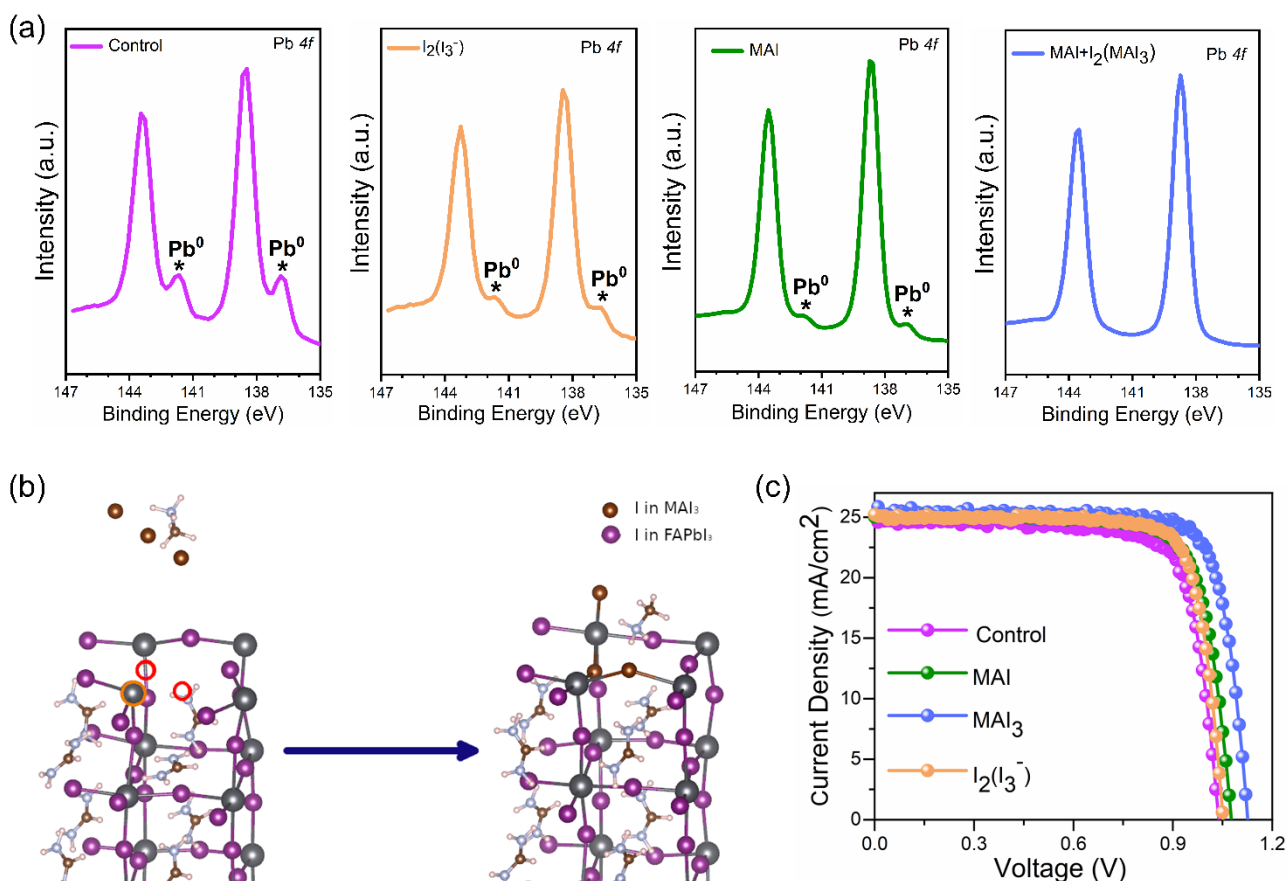


Figure 4.1. (a) High-resolution XPS spectra of Pb 4f with and without additives, (b) Gas-phase optimized initial and final state for the addition reaction of MAI₃ onto a FAPbI₃ surface with two halide vacancy defects (red circles) located next to Pb⁰ (orange circle) and (c) J-V curves of the devices with and without additives.

After screening the additives, we can see that the best results are obtained with MAI₃. From here on, we performed an in-depth investigation on the impact of the MAI₃ additive using multi-characterization techniques to unravel its effect on the device photophysics and determine the impact on device stability. Hereafter, the pristine perovskite is referred to as the Control, and perovskite with 5 mM and 10 mM of MAI₃ are referred to as the Target and Target-ex, respectively. We performed the backward and forward scans to examine the hysteresis in the Control and Target devices (Fig. 4.2a). The Control device shows a PCE of 19.77 % in the backward scan and 17.28% in the forward scan, whereas the Target shows a PCE of 23.10% in the backward and 22.67% in the forward scan which translated to a hysteresis index ($HI = [(PCE_{backward} - PCE_{forward}) / (PCE_{backward})] \times 100$) of 12.60% and 1.86% for the Control and Target device respectively. Figure 4.2b shows the stabilized power output (SPO) for the best performing devices during maximum power point tracking (MPP) in ambient air (15-25% RH (relative humidity)) under one sun illumination for 300 sec. The SPO upon MPP tracking for the Control and Target is 18.55% and 22.97% respectively. The statistical distribution of the photovoltaic characteristics (J_{sc} , V_{oc} , FF, and PCE) is presented in Figure 2c, which shows improvement in all device parameters. Furthermore, the incident photon-to-current efficiency (IPCE) spectra and integrated current density (Figure 4.2d) of the target device show almost no change in the onset of the IPCE spectra and the inflection point as compared to the Control which shows a bandgap of 1.555 eV. The cross-section morphology of the Control and Target PSC (Figure 4.2e) was characterized by scanning electron microscopy (SEM). The cross-sectional SEM images showed a well-stacked perovskite layer thickness of ~ 500nm.

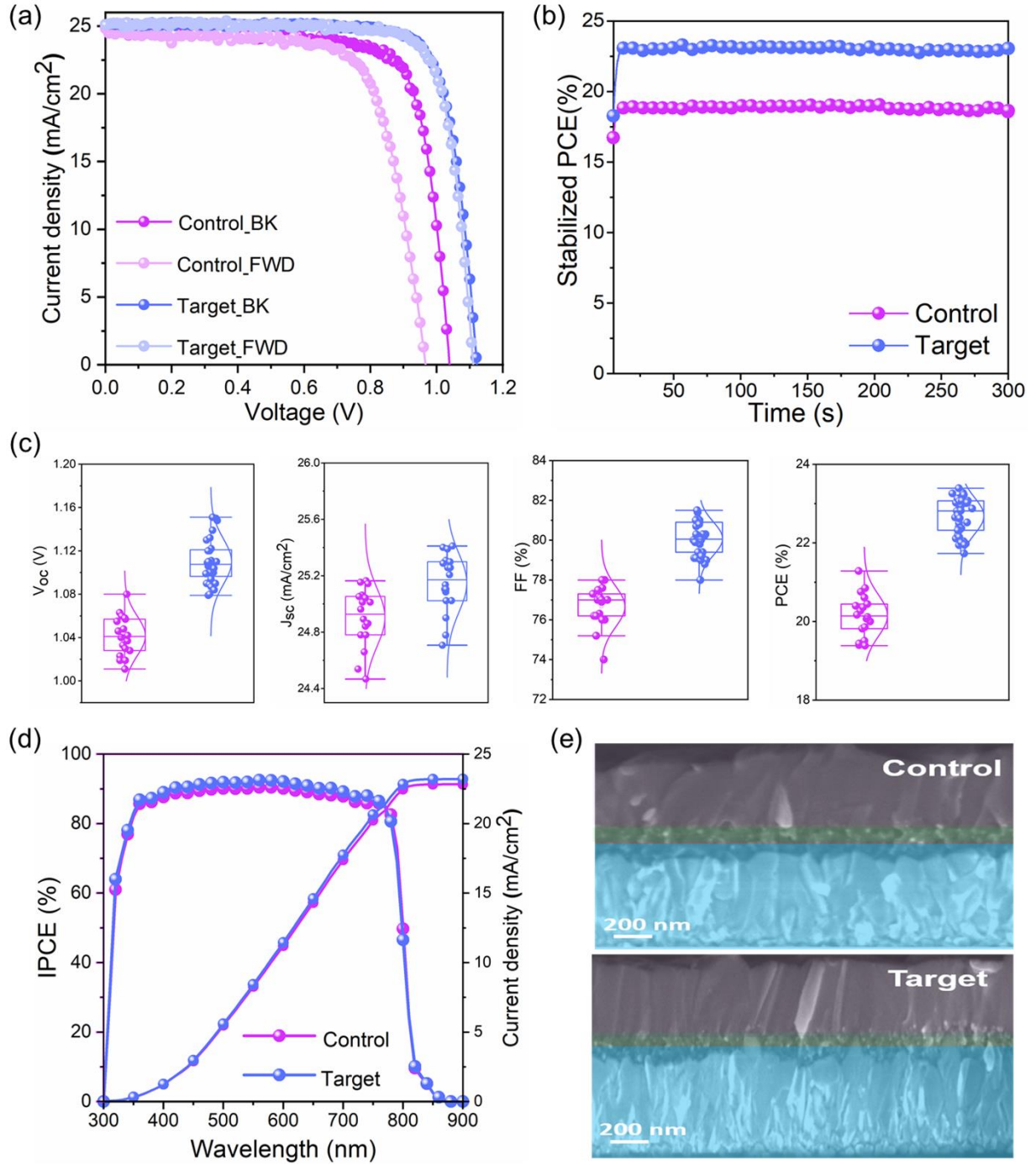


Figure 4.2. (a) J-V curves of the devices at backward and forward scan, (b) maximum power point tracking, (c) for Control and Target, (c) Statistical distribution J-V parameters of Control and Target devices, and (d) IPCE spectra and photocurrent integrated over the standard AM 1.5G solar spectrum, and (e) Cross-sectional SEM images of Control and Target devices, respectively.

The crystallinity and structural properties of perovskite films were analyzed by X-ray diffraction (Figure 4.3a, S4.5a,b). We found that the presence of a PbI_2 peak at 12.5° remains in all films which originate from the use of 3% excess of PbI_2 in the perovskite precursor solution. Upon the addition of MAI_3 as 5mM (Target) and 10 mM (Target-ex) into the Control perovskite $((\text{FAPbI}_3)_{0.98} (\text{MAPbBr}_3)_{0.02})$, we observe that the incorporation of MA^+ was successfully integrated into the crystal lattice of FAPbI_3 via a clear shift to a higher angle as shown in Figure 4.3a and Figure S4.5b. Also, we calculated the lattice cell parameters with and without the addition of MAI_3 , and it was found that the structure is tetragonal with ($a = 8.9655 \text{ \AA}$, $c = 12.6891 \text{ \AA}$), ($a = 8.9608 \text{ \AA}$, $c = 12.6872 \text{ \AA}$), ($a = 8.9596 \text{ \AA}$, $c = 12.6866 \text{ \AA}$) for the Control, Target and Target-ex, respectively. To quantify the incorporation of MA^+ into the lattice of FAPbI_3 , we used solid-state nuclear magnetic resonance (ssNMR) as shown in Figure S4.6. From ssNMR, we quantify that the Control film has only 1.3% of MA^+ , whereas the Target and Target-ex contain 3.2% and 3.8% of MA^+ , respectively, which confirms the incorporation of MA^+ in the lattice as suggested by XRD. Furthermore, this allows the composition to be redefined as Control $(\text{FAPbI}_3)_{0.987} (\text{MAPbBr}_3)_{0.013}$, Target $(\text{FAPbI}_3)_{0.986} (\text{MAPbBr}_3)_{0.032}$, and Target-ex as $(\text{FAPbI}_3)_{0.962} (\text{MAPbBr}_3)_{0.038}$. We further performed MD simulations to check the impact of the MAI_3 on the phase stability of cubic FAPbI_3 . We performed qualitative energy barrier calculations between cubic- FAPbI_3 and delta- FAPbI_3 for three cases: (a) without any iodide vacancy (b) having 3 iodide vacancies (out of 72 iodines in 288 atoms supercell), and (c) having 6 iodide vacancies. For these calculations, we use classical molecular dynamics (MD) simulations^{21,22}, the computational details of which are discussed in the methods section. We find a systematic decrease in the energy barrier from the cubic to the delta phase with an increasing number of iodide vacancies as shown in Figure S4.5c. This behavior shows that iodide vacancies in the bulk might also act as nucleation centers for the formation of delta- FAPbI_3 providing a further rationalization for the observed substantial increase in the stability

of the Target as compared to the Control sample. The surface morphology in the SEM images (Figure 4.3b) shows that both Control and Target perovskite films are uniform and highly crystalline with similar compact textures and grain sizes of hundreds of nanometers.

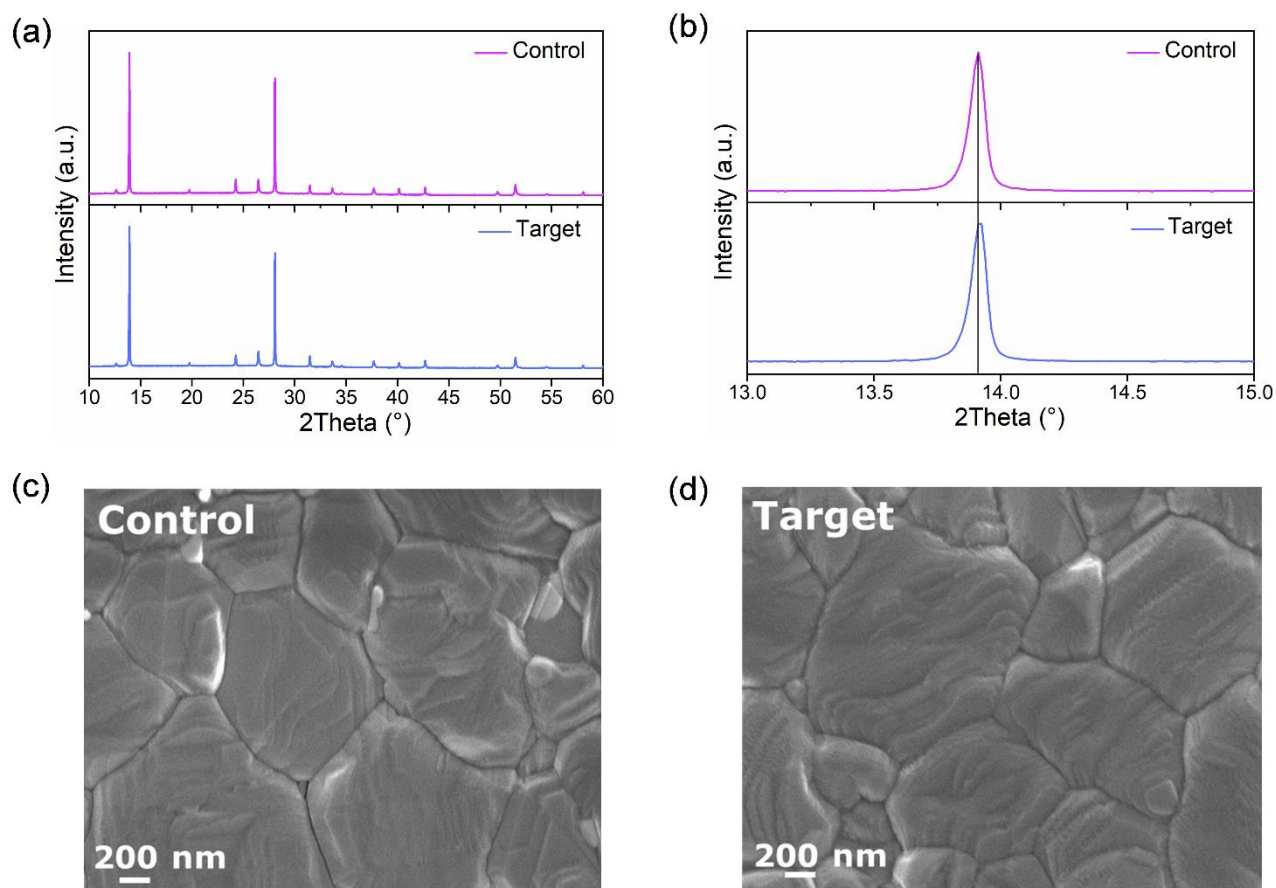


Figure 4.3. (a), (b) XRD patterns, and (c) top view SEM images of Control and Target films.

Next, we carried out an in-depth investigation of the optoelectronic properties of the Control and Target films. We performed time-resolved terahertz spectroscopy (TRTS) to get insights into the intrinsic charge carrier mobility and conductivity. The spectra and kinetics are shown in Figure S4.7 and S4.8, respectively. The spectra for both the Control and Target are predominantly flat and so we can conclude that there is no phase shift taking place which can lead to artifacts in the kinetic measurements. We can clearly see that the mobility (Figure 4.4a) and photoconductivity (Figure 4.4b) improved upon the addition of MAI₃ as compared to the

Control film at different fluences. This enhancement of mobility and photoconductivity could be one of the factors for the increase of the FF in the Target devices. To further verify this, we analyzed the devices in terms of diode characteristics. In figure 4.4c, we measured the ideality factor (n_{id}) by taking the dependence of V_{OC} as a function of incident light intensity. Upon the addition of 5 mM of MAI_3 (Target) the n_{id} decreases from 1.89 to 1.36, which indicates a substantial reduction of non-radiative recombination. Then, we fitted the J – V curves of the champion Control and Target devices to a two-diode equivalent circuit model²³ (Fig. S4.9a,b). Following the analysis proposed by Guillemoles et al.²⁴ and Stolterfoht et al.²⁵ the losses can be calculated and broken down into separate contributions (Figure 4.4d). First, the Shockley–Queisser limit is calculated from the bandgap, which we determined from the inflection point of the IPCE spectrum (Figure S4.4). A bandgap of 1.555 eV was obtained for both the Control and the Target device, which is expected due to the small amount of MA^+ being incorporated, thus having a limited effect on the bandgap. The performance losses related to the radiative limit with respect to the Shockley–Queisser limit account for 0.21% (V_{OC} loss) + 9.3% (J_{SC} loss) = 9.51% for the control and 0.16% (V_{OC} loss) + 7.0% (J_{SC} loss) = 7.16% for the target device, The J_{SC} losses are mainly due to nonideal and parasitic absorption. Substantially lower nonradiative losses are observed upon the addition of MAI_3 , decreasing from 17.9% (V_{OC} loss) + 8.1% (FF loss) = 26% in the control device to 11.1% (V_{OC} loss) + 7% (FF loss) = 18.1% in the target device. Transport losses manifest themselves in a further reduction of FF. These transport-related FF losses of the Control and Target samples are 4.8% and 3.5%, respectively. These improvements in FF are consistent with the enhanced charge carrier mobility in the Target.

To further confirm the role of nonradiative recombination, we measured absolute photoluminescence (PL) photon fluxes Φ_{PL} (\mathcal{E}) of Control and Target films (Figure 4e). Following established methods²⁶, the photoluminescence quantum yields (PLQY) were

calculated as 1.53% and 0.61% for Target and Control samples, respectively. The enhancement in the PLQY for the Target films indicates suppression of non-radiative recombination centers in the bulk of the perovskite. To gain further insights into the charge carrier dynamics we performed time-resolved photoluminescence spectroscopy (TRPL) using laser excitation pulses of low fluences ($<5\text{ nJ/cm}^2$) so that bimolecular and Auger recombination are negligible²⁷. The signal after $t > 200\text{ ns}$ is dominated by a monoexponential decay (Figure 4.4f). Since it is impossible to distinguish between surface and bulk recombination, we modeled two extreme cases for the interpretation of the TRPL data in Figure 4.4f and Tables S4.3, and S4.4. In the first case, we assumed zero surface recombination, which means the decay is attributed solely to the bulk recombination with a fitted monomolecular recombination constant $k_1 = 2.0 \cdot 10^6\text{ s}^{-1}$ (TRPL decay time or charge carrier lifetime: $\tau = 1/(2 \cdot k_1) = 250\text{ ns}$) for the Control and $k_1 = 1.0 \cdot 10^6\text{ s}^{-1}$ ($\tau = 500\text{ ns}$) for the Target sample. Also, we estimated the lower limit of diffusion length (L_D) via $L_D = \sqrt{\frac{\mu k T \tau}{e}}$ where μ is the mobility, and k , T , e , and τ are the Boltzmann constant, temperature, elementary charge, and charge carrier lifetime, respectively. The charge carrier mobility was calculated to be $39.5\text{ cm}^2\text{V}^{-1}\text{S}^{-1}$ for the control and $45.5\text{ cm}^2\text{V}^{-1}\text{S}^{-1}$ for the target at an excitation fluence of $16.91\text{ }\mu\text{Jcm}^{-2}$. From these mobilities values, we derive $L_D = 0.72\text{ }\mu\text{m}$ for the control device and $L_D = 1.07\text{ }\mu\text{m}$ for the target. In the second case, we assumed that the TRPL decays of both samples are dominated by surface recombination, with a surface recombination velocity S fitted as 120 cm/s for the control and 62 cm/s for the target sample. Both cases show that there is an enhancement of the charge carrier lifetime and suppression of non-radiative recombination in the Target sample. Overall, these results, acquired from TRTS, PV device loss analysis, n_{id} , PLQY, and TRPL measurements indicate that the addition of MAI₃ simultaneously reduces the non-radiative recombination rate and increases the charge carrier mobility, leading to the observed improvements in both V_{OC} and FF.

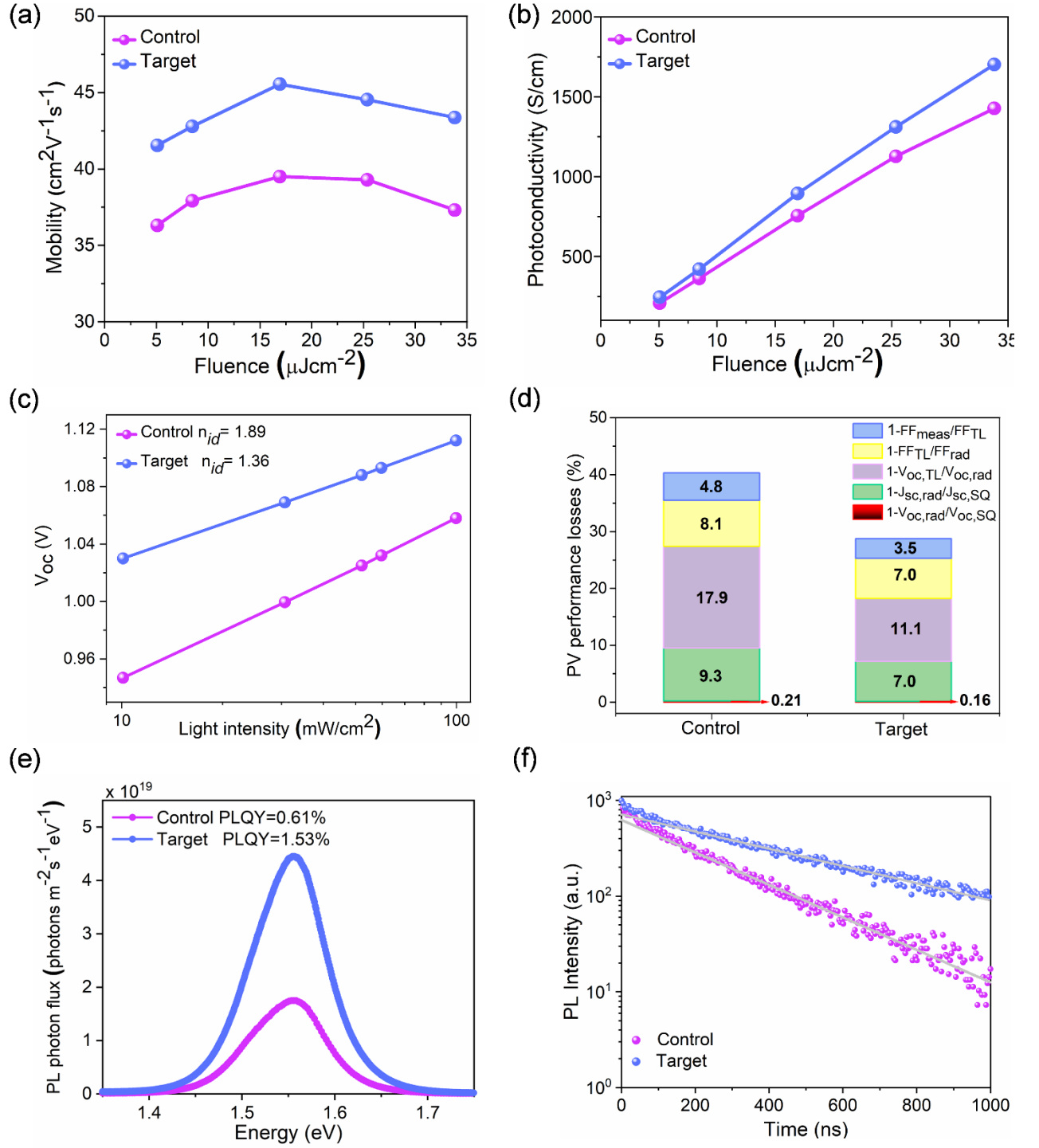


Figure 4.4. (a) and (b) THz carrier mobility and material photoconductivity as a function of pulsed excitation energy fluence at $\lambda = 580$ nm, (c) Open circuit voltage (V_{oc}) at a different light intensity, (d) PV performance losses evolution, (e) Absolute photon flux measurements of complete devices at 1 sun excitation from which the PLQY is determined. (f) Time-resolved photoluminescence (TRPL) measurements of Control and Target, respectively.

Thermal and operational stability remains a major concern in perovskite solar cells²⁸⁻³⁰. Therefore, we carried out the stability test on the Control and Target by subjecting them to different stress conditions. Firstly, we carried out a shelf-life test by keeping the devices in the dark under 10% RH. The Control and Target retained 74% and 93% of the initial performance after 800 hours, respectively (Figure 4.5a). Secondly, we carried out a thermal stability test by keeping the devices at 50-55 °C in ambient conditions (25-35% RH). The Control and Target retained 28% and 60% of the initial performance after 300 hours, respectively (Figure 4.5b). Lastly, we performed operational stability tests at MPP for 350 hours under continuous one sun illumination. The Control and Target devices retained 57 % and 89 % of the initial performance respectively. Typically, the defects are known to be responsible for the instability hence the improvement in the stability is likely the result of improved optoelectronic properties and reduction in defects. This showed that our strategy with perovskite bulk engineering via MAI₃ not only improves the performance of PCSs but also enhances the device stability under standard stress conditions.

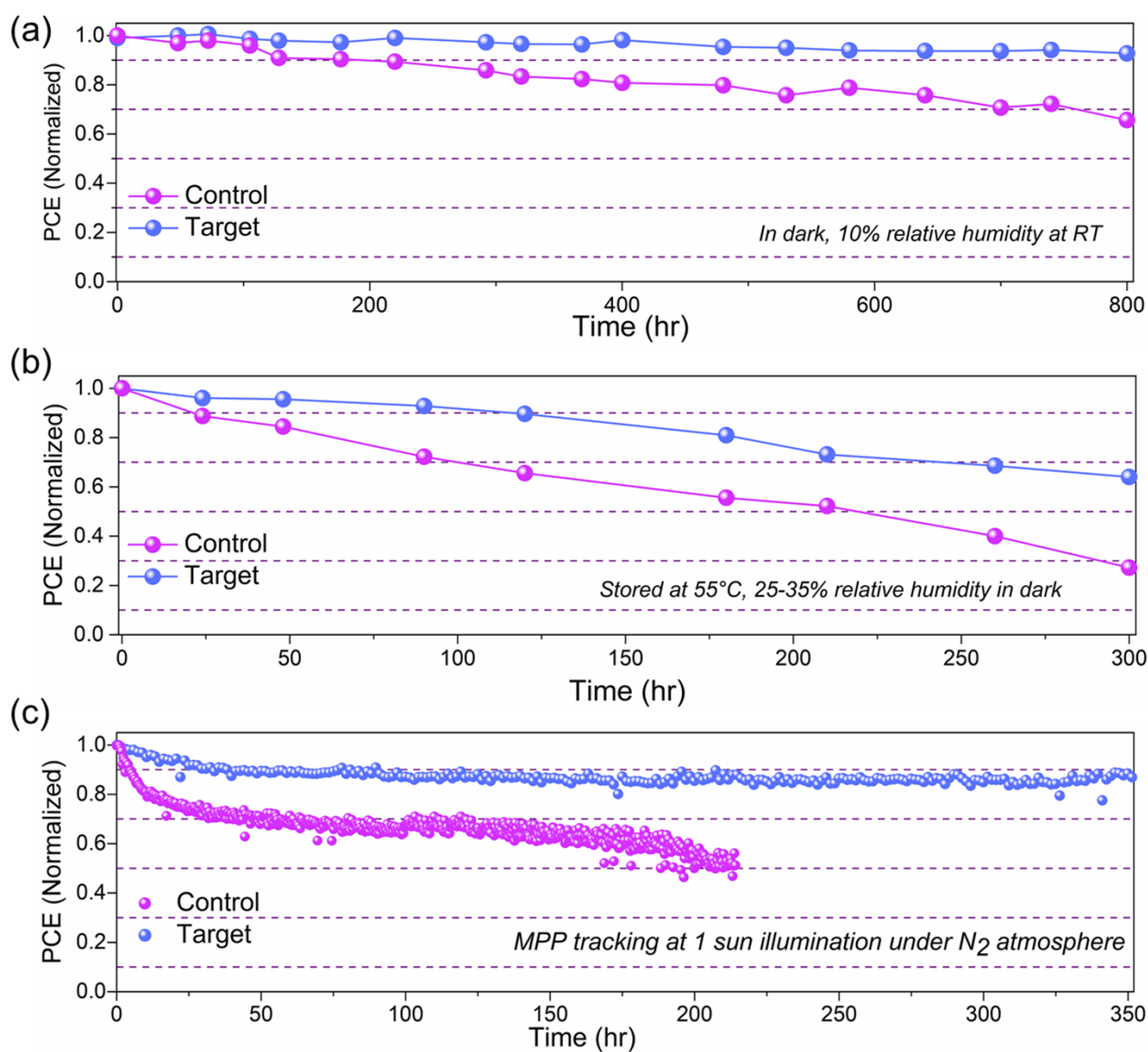


Figure 4.5. Long term stability (a) Shelf-life at RT, in dark with 10-30% relative humidity, (b) Devices were stored at 55 °C with a relative humidity of ~ 10 - 15% in dark, and (c) Operational stability in a nitrogen environment at room temperature under continuous illumination (White LED, 1 Sun) at maximum power point for Control and Target, respectively.

4.3 Conclusion

In summary, we employed MAI₃ as an additive in the perovskite precursor solution of metal halide perovskite absorber, affording passivation of Pb⁰ and charged defects leading to suppression of non-radiative recombination and enhanced charge carrier mobility. As a result, we achieve a PCE exceeding 23% with the MAI₃ modulated Target which also exhibits a remarkable improvement in stability with respect to the Control regardless of the external aging conditions (high temperature, ambient, MPP). The facile strategy provided in this work has the potential to stimulate other successful developments in the future.

4.4 Experimental Methods

4.4.1 Device fabrication: Fluorine-doped tin oxide (FTO)-glass substrates (TCO glass, NSG 10, Nippon sheet glass, Japan) were etched and cleaned by ultrasonication in Hellmanex (2%, deionized water), rinsed thoroughly with de-ionized water and ethanol, and then treated in oxygen plasma for 30 min. Approximately, 30 to 25 nm blocking layer (TiO₂) was sprayed on the cleaned FTO at 450 °C using a commercial titanium diisopropoxide bis(acetylacetonate) solution (75% in 2-propanol, Sigma-Aldrich) diluted in anhydrous ethanol (1:10 volume ratio). A 150 nm mesoporous TiO₂ layer (diluted paste (1:6.5 wt. ratio) (Dyesol 30NRD: ethanol)) spin-coated at 5000 rpm for 15 s and then sintered at 450 °C for 30 min in dry air. The perovskite films were deposited using a single-step deposition method from the precursor solution which was prepared in Argon atmosphere and containing 1.45 M of FAI, MABr, PbI₂, and PbBr₂ in anhydrous dimethylformamide/ dimethylsulphoxide (4:1 (volume ratio)) to achieve the desired composition: FA_{0.98}MA_{0.02}Pb(I_{0.98}Br_{0.02})₃ (3% PbI₂ excess). For the additives, three stock solutions of 0.1 M were prepared of I₂, MAI, and MAI+I₂ by dissolving in IPA and stirred at 70°C at different times. Then, each of them was added to the perovskite composition at different concentrations. The device fabrication was carried out inside a dry air box, under controlled atmospheric conditions. Perovskite solution was spin-coated in a two-

step program at 1000 and 5000 rpm, respectively. 270 μ l of chlorobenzene was dropped on the spinning substrate. This was followed by annealing the films at 150 °C for 35 to 40 min. After cooling down the substrate all films (control film included) passivated by EAI (3mgml⁻¹)¹⁷. For completing the fabrication of devices, 90 mg of 2,2',7,7'-tetrakis(*N,N*-di-*p*-methoxyphenylamine)-9,9-spirobifluorene (spiro-OMeTAD) was dissolved in 1 ml of chlorobenzene as a hole-transporting material (HTM). The HTM was spin-coated at 5000 rpm for 30 s. The HTM was doped with bis(trifluoromethylsulfonyl)imide lithium salt (23.2 μ l prepared by dissolving 520 mg LiTFSI in 1 ml of acetonitrile), and 36 μ l of 4-tert-butylpyridine. Finally, a ~80 nm gold (Au) layer was thermally evaporated.

4.4.2 Device characterization: The current-voltage (*J-V*) characteristics of the perovskite devices were recorded under ambient temperature and air conditions with a digital source meter (Keithley model 2400, USA). A 450 W xenon lamp (Oriol, USA) was used as the light source for photovoltaic (*J-V*) measurements. The spectral output of the lamp was filtered using a Schott K113 Tempax sunlight filter (Präzisions Glas & Optik GmbH, Germany) to reduce the mismatch between the simulated and actual solar spectrum to less than 2%. The light intensity was ranging between 0.98 to 1Sun. The photo-active area of 0.158 cm² was defined using a dark-colored metal mask.

4.4.3 Incident photon-to-current efficiency (IPCE): was recorded under a constant white light bias of approximately 5 mW cm⁻² supplied by an array of white light-emitting diodes. The excitation beam coming from a 300 W Xenon lamp (ILC Technology) was focused through a Gemini- 180 double monochromator (Jobin Yvon Ltd) and chopped at approximately 2 Hz. The signal was recorded using a Model SR830 DSP Lock-In Amplifier (Stanford Research Systems).

4.4.4 Scanning electron microscopy (SEM): SEM was performed on a ZEISS Merlin HR-SEM.

4.4.5 X-ray photoelectron spectroscopy (XPS): XPS measurements were carried out on an Axis Supra (Kratos Analytical) using the monochromated Ka X-ray line of an Aluminium anode. The pass energy was set to 20eV with a step size of 0.1eV. The samples were electrically grounded through the FTO substrate to limit charging effects.

4.4.6 X-ray powder diffractions: X-ray patterns were recorded on a Bruker D8 Discover (Cu anode, $\lambda = 1.54060 \text{ \AA}$) in Bragg Brentano geometry, equipped with a Johansson $K\alpha_1$ monochromator and a Lynxeye XE detector. Lattice parameters were extracted from profile fitting using Topas 5.

4.4.7 Time-resolved photoluminescence (TRPL): The photoluminescence lifetime was measured via time-correlated single-photon counting (TCSPC) using a LifeSpec II (Edinburgh Instruments) fluorescence spectrometer with a picosecond pulsed diode laser (EPL-510, Edinburgh Instruments) at 510 nm wavelength, 85 ps pulse width, and 4.5 nJ/cm² fluence.

4.4.8 Solid-state NMR measurements. Solid-state NMR ¹H measurements were carried out at 900.14 MHz using a Bruker Avance Neo console and a 1.3 mm variable temperature CPMAS probe at a spin rate of 60 kHz. The measurements were taken using a standard echo sequence with an echo delay of one rotor period with 100 kHz RF power. A delay time of 5 times T₁ was used in order to obtain quantitative results. The spectra were baseline corrected and the areas were extracted using the multipeak fit tool in Origin Lab.

4.4.9 Long-term light soaking test: Stability measurements were performed with a Biologic MPG2 potentiostat under a full AM 1.5 Sun-equivalent white LED lamp. The devices were measured with a maximum power point (MPP) tracking routine under continuous illumination at room temperature. The MPP was updated every 10 s by a standard perturb and

observe method. Every minute a *JV* curve was recorded in order to track the evolution of individual *JV* parameters.

4.4.10 Photoluminescence quantum yield (PLQY): PLQY was acquired following the procedure suggested by de Mello²⁶. The samples were excited using a continuous-wave laser (OBIS LX, 660 nm) whose power was adjusted to match the photogeneration rate under 1Sun illumination (0.324 mW, 0.786mm effective beam FWHM). Signal was collected using an integrating sphere (Gigahertz Optik, UPB-150-ARTA) connected via a multimode, 400 μ m diameter optical fiber (Thorlabs BFL44LS01) to a spectrometer (Andor, Kymera 193i). The system was spectrally calibrated using an irradiance calibration standard lamp (Gigahertz Optik, BN-LH250-V01).

4.4.11 Time-resolved Terahertz Spectroscopy (TRTS): TRTS measurements were conducted using a femtosecond visible pump-THz probe setup based on an amplified Ti: Sapphire laser (Libra, Coherent) delivering 800 nm pulses with a pulse duration of 45 fs and a 1 kHz repetition rate. The fundamental output was split into three beams. The first was used to pump a white-light seeded optical parametric amplifier (OPerA Solo, Coherent), yielding the 580 nm pump beam. The second fundamental beam was used to generate the THz probe through a two-color plasma method³¹. The beam was focused, using a fused silica lens ($f = 75$ mm), and passed through a 100 μ m beta-barium borate (BBO) crystal to generate the second harmonic. The electric field of the two-color beam was strong enough, at the focal point, to form a plasma that radiates THz pulses (200 fs, 1-20 THz), which were subsequently collimated and focused onto the sample. The transmitted beam was subsequently detected using a homemade ABCD detector (Air Based Coherent Detection)³². The final portion of the fundamental was used as the gate beam and was used to generate a second harmonic signal proportional to that of the THz electric field measured with a photomultiplier tube (PMM01,

Thorlabs). The SHG process took place inside an enclosed box with a butane atmosphere³³, allowing for increased sensitivity when measuring the dynamics.

4.4.12 Computational Methods

Structural relaxation: All computations related to structural relaxation were done on the DFT level of theory using Quantum ESPRESSO v6.6^{34–36}. Apart from variable-cell relaxations, all relaxations applied the Perdew-Burke-Ernzerhof (PBE) functional using ultrasoft pseudopotentials from the pslibrary 1.0.0, a wavefunction cutoff of 60 Ry, a charge density cutoff of 480 Ry, a 6x6x1 k-point Monkhorst-Pack grid without offset, Gaussian spreading of 0.01 Ry and the semiempirical Grimme 's DFT-D3 vdW correction. For the variable-cell relaxations PBEsol was applied and the remaining parameters chosen the same as above. The structural relaxation of the initial and final state for the addition reaction of MAI₃ onto FAPbI₃ was done in multiple steps. Initially, a 2x2x6 supercell of pure FAPbI₃ (without defects) was optimized using variable cell relaxation. Next, 42 Å of empty space was introduced along the z-direction in order to generate a realistic surface model Pb-I as terminating layer. Furthermore, two iodides next to a common Pb located at the surface were removed, two electrons were added and the structure was reoptimized. Upon relaxation of an isolated MAI₃, this molecule was added in various orientations at distances of 3.0-3.5 Å with respect to the halide vacancies. After undergoing another relaxation, this gave a set of seven final states, each with the two initial defects filled by iodides and the third iodide attached to one of the Pb ions on the surface (SI). The initial reference state was constructed in a similar manner, by placing the optimized MAI₃ at a distance of 9-12 Å from the surface with three different orientations each of which underwent a relaxation. For both the initial and final states, the lowest energy structure was used for the charge analysis.

Bader charge analysis: A Gaussian CUBE file was generated based on the optimized density using the *PostProc* package from Quantum ESPRESSO. From the Gaussian CUBE file, the Bader charges were computed using the program developed by Henkelman's group³⁷.

Simulations of phase transition: Classical MD simulations were performed in isothermal-isobaric ensemble similar to our previous studies^{38,39}. All simulations were performed with the Large-scale Atomic/Molecular Massively Parallel Simulator (LAMMPS) code (31 Mar 2017)³⁸. We used a 1.0 nm cutoff for nonbonded interactions, SHAKE³⁹ for constraints and particle-particle-particle-mesh Ewald for electrostatic interactions. We used a velocity rescaling thermostat⁴⁰ with a relaxation time of 0.1 ps and a Parrinello-Rahman barostat⁴¹ to keep the pressure at atmospheric pressure with a relaxation time of 10 ps.

4.5 Reference

- 1 A. Kojima, K. Teshima, Y. Shirai and T. Miyasaka, *J. Am. Chem. Soc.*, 2009, **131**, 6050–6051.
- 2 J. J. Yoo, G. Seo, M. R. Chua, T. G. Park, Y. Lu, F. Rotermund, Y. K. Kim, C. S. Moon, N. J. Jeon, J. P. Correa-Baena, V. Bulović, S. S. Shin, M. G. Bawendi and J. Seo, *Nature*, 2021, **590**, 587–593.
- 3 W. Hui, L. Chao, H. Lu, F. Xia, Q. Wei, Z. Su, T. Niu, L. Tao, B. Du, D. Li, Y. Wang, H. Dong, S. Zuo, B. Li, W. Shi, X. Ran, P. Li, H. Zhang, Z. Wu, C. Ran, L. Song, G. Xing, X. Gao, J. Zhang, Y. Xia, Y. Chen and W. Huang, *Science*, 2021, **371**, 1359–1364.
- 4 Best Research-Cell Efficiency Chart | Photovoltaic Research | NREL, <https://www.nrel.gov/pv/cell-efficiency.html>, (accessed 13 April 2021).
- 5 Y. Zhao, P. Zhu, S. Huang, S. Tan, M. Wang, R. Wang, J. Xue, T. H. Han, S. J. Lee, A. Zhang, T. Huang, P. Cheng, D. Meng, J. W. Lee, J. Marian, J. Zhu and Y. Yang, *J. Am. Chem. Soc.*, 2020, **142**, 20071–20079.
- 6 J. Xue, R. Wang and Y. Yang, *Nat. Rev. Mater.*, 2020, **5**, 809–827.
- 7 N. Liu and C. Y. Yam, *Phys. Chem. Chem. Phys.*, 2018, **20**, 6800–6804.
- 8 L. Wang, H. Zhou, J. Hu, B. Huang, M. Sun, B. Dong, G. Zheng, Y. Huang, Y. Chen, L. Li, Z. Xu, N. Li, Z. Liu, Q. Chen, L. D. Sun and C. H. Yan, *Science*, 2019, **363**, 265–270.
- 9 G. Y. Kim, A. Senocrate, T. Y. Yang, G. Gregori, M. Grätzel and J. Maier, *Nat. Mater.*, 2018, **17**, 445–449.
- 10 E. A. Alharbi, T. P. Baumeler, A. Krishna, A. Y. Alyamani, F. T. Eickemeyer, O. Ouellette, L. Pan, F. S. Alghamdi, Z. Wang, M. H. Alotaibi, B. Yang, M. Almalki, M. D. Mensi, H. Albrithen, A. Albadri, A. Hagfeldt, S. M. Zakeeruddin and M. Grätzel, *Adv. Energy Mater.*, 2021, 2003785.
- 11 E. A. Alharbi, M. I. Dar, N. Arora, M. H. Alotaibi, Y. A. Alzhrani, P. Yadav, W. Tress, A. Alyamani, A. Albadri, S. M. Zakeeruddin and M. Grätzel, *Research*, 2019, **2019**, 1–9.
- 12 P. Yadav, M. I. Dar, N. Arora, E. A. Alharbi, F. Giordano, S. M. Zakeeruddin and M. Grätzel, *Adv. Mater.*, 2017, **29**, 1701077.
- 13 T. Baumeler, N. Arora, A. Hinderhofer, S. Akin, A. Greco, M. Abdi-Jalebi, R. Shivanna, R. Uchida, Y. Liu, F. Schreiber, S. M. Zakeeruddin, R. H. Friend, M. Graetzel and M. I. Dar, *J. Phys. Chem. Lett.*, 2020, **11**, 10188–10195.
- 14 H. Zhu, Y. Liu, F. T. Eickemeyer, L. Pan, D. Ren, M. A. Ruiz-Preciado, B. Carlsen, B. Yang, X. Dong, Z. Wang, H. Liu, S. Wang, S. M. Zakeeruddin, A. Hagfeldt, M. I. Dar, X. Li and M. Grätzel, *Adv. Mater.*, 2020, **32**, 1907757.
- 15 Y. Liu, S. Akin, L. Pan, R. Uchida, N. Arora, J. V. Milić, A. Hinderhofer, F. Schreiber, A. R. Uhl, S. M. Zakeeruddin, A. Hagfeldt, M. Ibrahim Dar and M. Grätzel, *Sci. Adv.*, 2019, **5**, eaaw2543.
- 16 Y. Li, H. Wu, W. Qi, X. Zhou, J. Li, J. Cheng, Y. Zhao, Y. Li and X. Zhang, *Nano Energy*,

- 2020, **77**, 105237.
- 17 E. A. Alharbi, A. Y. Alyamani, D. J. Kubicki, A. R. Uhl, B. J. Walder, A. Q. Alanazi, J. Luo, A. Burgos-Caminal, A. Albadri, H. Albrithen, M. H. Alotaibi, J. E. Moser, S. M. Zakeeruddin, F. Giordano, L. Emsley and M. Grätzel, *Nat. Commun.*, 2019, **10**, 1–9.
 - 18 Y. H. Lin, N. Sakai, P. Da, J. Wu, H. C. Sansom, A. J. Ramadan, S. Mahesh, J. Liu, R. D. J. Oliver, J. Lim, L. Aspitarte, K. Sharma, P. K. Madhu, A. B. Morales-Vilches, P. K. Nayak, S. Bai, F. Gao, C. R. M. Grovenor, M. B. Johnston, J. G. Labram, J. R. Durrant, J. M. Ball, B. Wenger, B. Stannowski and H. J. Snaith, *Science*, 2020, **369**, 96–102.
 - 19 I. Turkevych, S. Kazaoui, N. A. Belich, A. Y. Grishko, S. A. Fateev, A. A. Petrov, T. Urano, S. Aramaki, S. Kosar, M. Kondo, E. A. Goodilin, M. Graetzel and A. B. Tarasov, *Nat. Nanotechnol.*, 2019, **14**, 57–63.
 - 20 M. Afrooz and H. Dehghani, *RSC Adv.*, 2015, **5**, 50483–50493.
 - 21 P. Ahlawat, M. I. Dar, P. Piaggi, M. Grätzel, M. Parrinello and U. Rothlisberger, *Chem. Mater.*, 2020, **32**, 529–536.
 - 22 P. Ahlawat, A. Hinderhofer, E. A. Alharbi, H. Lu, A. Ummadisingu, H. Niu, M. Invernizzi, S. M. Zakeeruddin, M. I. Dar, F. Schreiber, A. Hagfeldt, M. Grätzel, U. Rothlisberger and M. Parrinello, *Sci. Adv.*, 2021, **7**, eabe3326.
 - 23 C. Zhang, J. Zhang, Y. Hao, Z. Lin and C. Zhu, *J. Appl. Phys.*, 2011, **110**, 064504.
 - 24 J. F. Guillemoles, T. Kirchartz, D. Cahen and U. Rau, *Nat. Photonics*, 2019, **13**, 501–505.
 - 25 M. Stollerfoht, M. Grischek, P. Caprioglio, C. M. Wolff, E. Gutierrez-Partida, F. Peña-Camargo, D. Rothhardt, S. Zhang, M. Raoufi, J. Wolansky, M. Abdi-Jalebi, S. D. Stranks, S. Albrecht, T. Kirchartz and D. Neher, *Adv. Mater.*, 2020, **32**, 2000080.
 - 26 J. C. de Mello, H. F. Wittmann and R. H. Friend, *Adv. Mater.*, 1997, **9**, 230–232.
 - 27 T. Kirchartz, J. A. Márquez, M. Stollerfoht and T. Unold, *Adv. Energy Mater.*, 2020, **10**, 1904134.
 - 28 W. Tress, K. Domanski, B. Carlsen, A. Agarwalla, E. A. Alharbi, M. Graetzel and A. Hagfeldt, *Nat. Energy*, 2019, **4**, 568–574.
 - 29 P. Yadav, D. Prochowicz, E. A. Alharbi, S. M. Zakeeruddin and M. Grätzel, *J. Mater. Chem. C*, 2017, **5**, 7799–7805.
 - 30 K. Domanski, E. A. Alharbi, A. Hagfeldt, M. Grätzel and W. Tress, *Nat. Energy*, 2018, **3**, 61–67.
 - 31 K. Y. Kim, A. J. Taylor, J. H. Glowina and G. Rodriguez, *Nat. Photonics*, 2008, **2**, 605–609.
 - 32 N. Karpowicz, J. Dai, X. Lu, Y. Chen, M. Yamaguchi, H. Zhao, X. C. Zhang, L. Zhang, C. Zhang, M. Price-Gallagher, C. Fletcher, O. Mamer, A. Lesimple and K. Johnson, *Appl. Phys. Lett.*, 2008, **92**, 011131.
 - 33 X. Lu and X. C. Zhang, *J. Infrared, Millimeter, Terahertz Waves*, 2011, **32**, 562–569.
 - 34 P. Giannozzi, S. Baroni, N. Bonini, M. Calandra, R. Car, C. Cavazzoni, D. Ceresoli, G. L.

- Chiarotti, M. Cococcioni, I. Dabo, A. Dal Corso, S. De Gironcoli, S. Fabris, G. Fratesi, R. Gebauer, U. Gerstmann, C. Gougoussis, A. Kokalj, M. Lazzeri, L. Martin-Samos, N. Marzari, F. Mauri, R. Mazzarello, S. Paolini, A. Pasquarello, L. Paulatto, C. Sbraccia, S. Scandolo, G. Sclauzero, A. P. Seitsonen, A. Smogunov, P. Umari and R. M. Wentzcovitch, *J. Phys. Condens. Matter*, 2009, **21**, 395502.
- 35 P. Giannozzi, O. Andreussi, T. Brumme, O. Bunau, M. Buongiorno Nardelli, M. Calandra, R. Car, C. Cavazzoni, D. Ceresoli, M. Cococcioni, N. Colonna, I. Carnimeo, A. Dal Corso, S. De Gironcoli, P. Delugas, R. A. Distasio, A. Ferretti, A. Floris, G. Fratesi, G. Fugallo, R. Gebauer, U. Gerstmann, F. Giustino, T. Gorni, J. Jia, M. Kawamura, H. Y. Ko, A. Kokalj, E. Küçükbenli, M. Lazzeri, M. Marsili, N. Marzari, F. Mauri, N. L. Nguyen, H. V. Nguyen, A. Otero-De-La-Roza, L. Paulatto, S. Poncé, D. Rocca, R. Sabatini, B. Santra, M. Schlipf, A. P. Seitsonen, A. Smogunov, I. Timrov, T. Thonhauser, P. Umari, N. Vast, X. Wu and S. Baroni, *J. Phys. Condens. Matter*, 2017, **29**, 465901.
- 36 P. Giannozzi, O. Baseggio, P. Bonfà, D. Brunato, R. Car, I. Carnimeo, C. Cavazzoni, S. De Gironcoli, P. Delugas, F. Ferrari Ruffino, A. Ferretti, N. Marzari, I. Timrov, A. Urru and S. Baroni, *J. Chem. Phys.*, 2020, **152**, 154105.
- 37 G. Henkelman, A. Arnaldsson and H. Jónsson, *Comput. Mater. Sci.*, 2006, **36**, 354–360.
- 38 S. Plimpton, *J. Comput. Phys.*, 1995, **117**, 1–19.
- 39 J. P. Ryckaert, G. Ciccotti and H. J. C. Berendsen, *J. Comput. Phys.*, 1977, **23**, 327–341.
- 40 G. Bussi, D. Donadio and M. Parrinello, *J. Chem. Phys.*, 2007, **126**, 14101.
- 41 M. Parrinello and A. Rahman, *J. Appl. Phys.*, 1981, **52**, 7182–7190.

4.5 Supplementary information

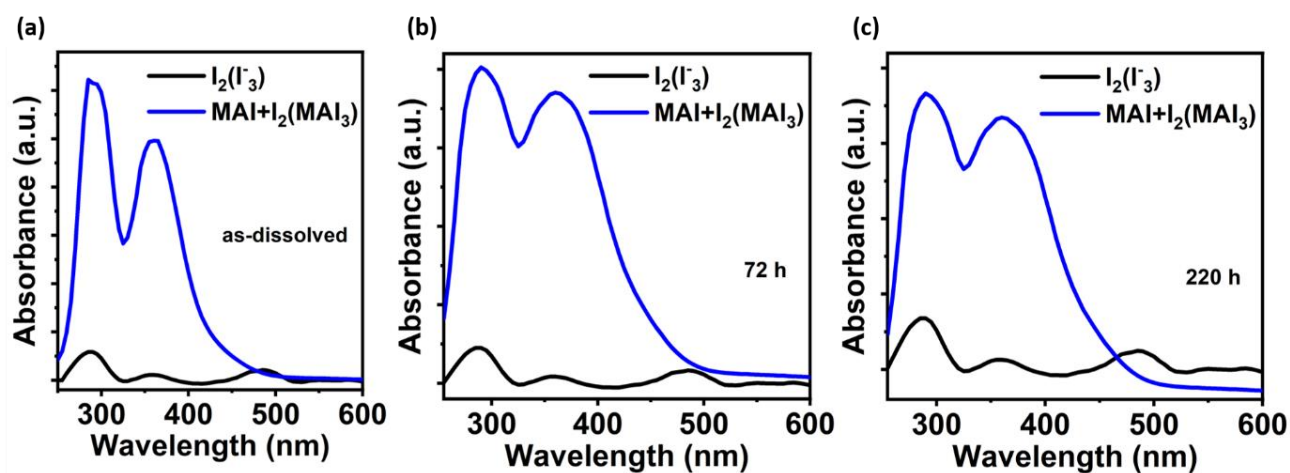
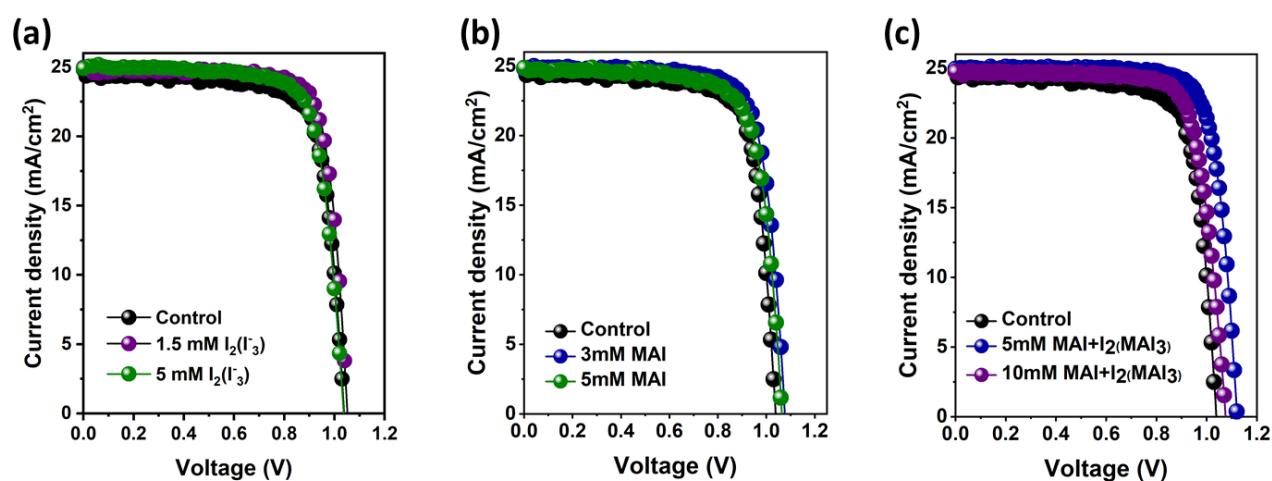


Figure S4.1. (a), (b) and (c) UV-Vis absorbance of I_2 , MAI and MAI+ I_2 at different time.



(d)

| V_{oc} (V) | J_{sc} (mA/cm ²) | FF(%) | PCE(%) | V_{oc} (V) | J_{sc} (mA/cm ²) | FF(%) | PCE(%) |
|------------------------|-----------------------------------|-------|--------|-------------------------------------|-----------------------------------|-------|--------|
| Control | | | | 3mM MAI | | | |
| 1.045 | 25.06 | 76.7 | 20.32 | 1.08 | 25.03 | 77.2 | 21.08 |
| 1.5 mM (I_2) I_3 | | | | 5mM MAI | | | |
| 1.052 | 25.20 | 79.5 | 21.43 | 1.064 | 25.08 | 75.0 | 20.02 |
| 5mM (I_2) I_3 | | | | 5mM (MAI+ I_2) MAI ₃ | | | |
| 1.037 | 25.16 | 76.6 | 20.24 | 1.13 | 25.20 | 81.4 | 23.46 |
| | | | | 10mM (MAI+ I_2) MAI ₃ | | | |
| | | | | 1.07 | 24.97 | 77.0 | 20.61 |

Figure S4.2. (a), (b) and (c) J-V curve of the optimized devices for each additive and (d) summarized J-V results for each additive.

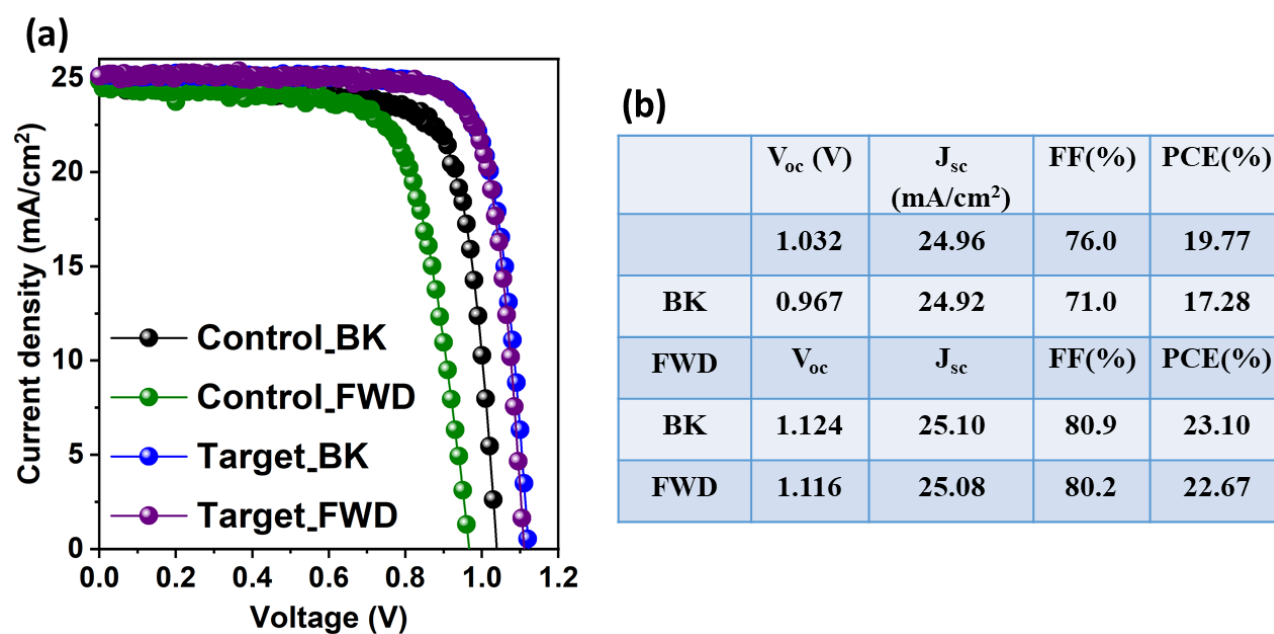


Figure S4.3. J-V curves and (b) Summarized result J-V of the Control and target at backward and forward scan.

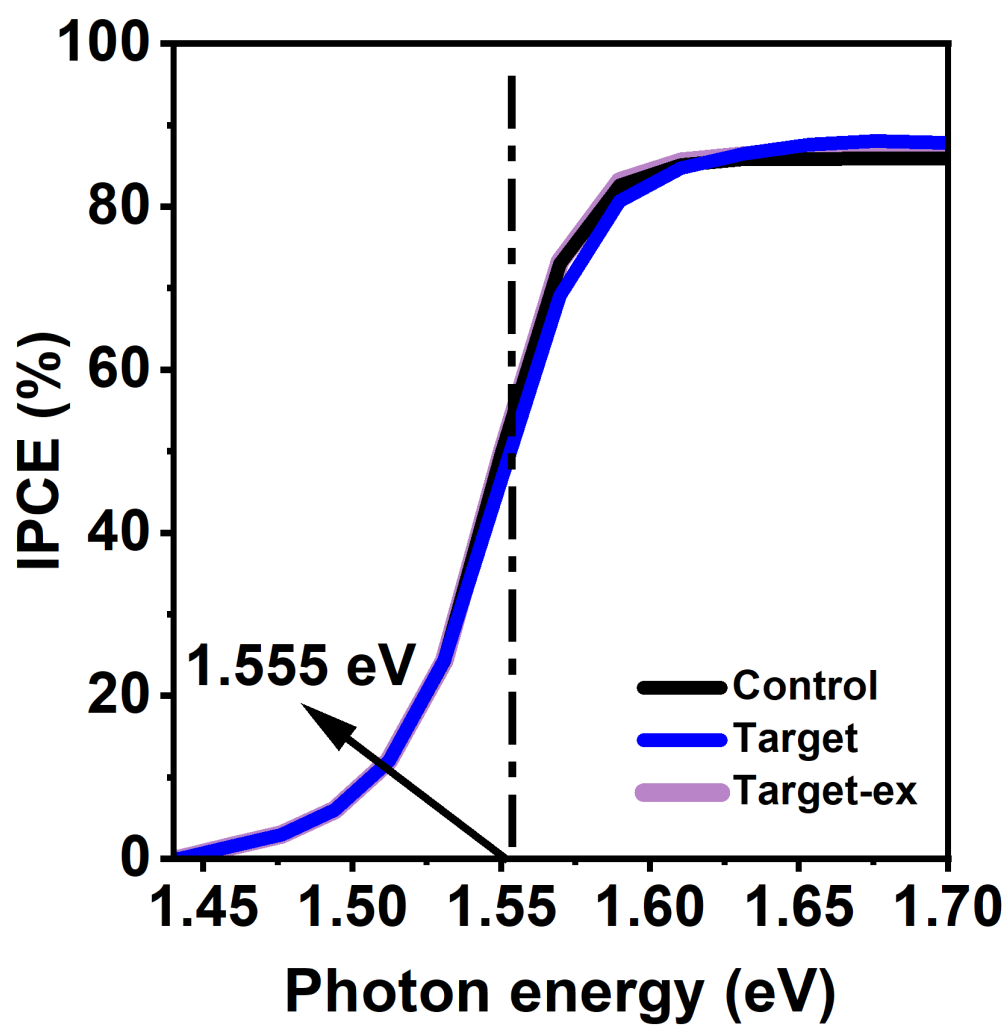


Figure S4.4. Bandgap extracted from IPCE of solar cells by taking the inflection point.

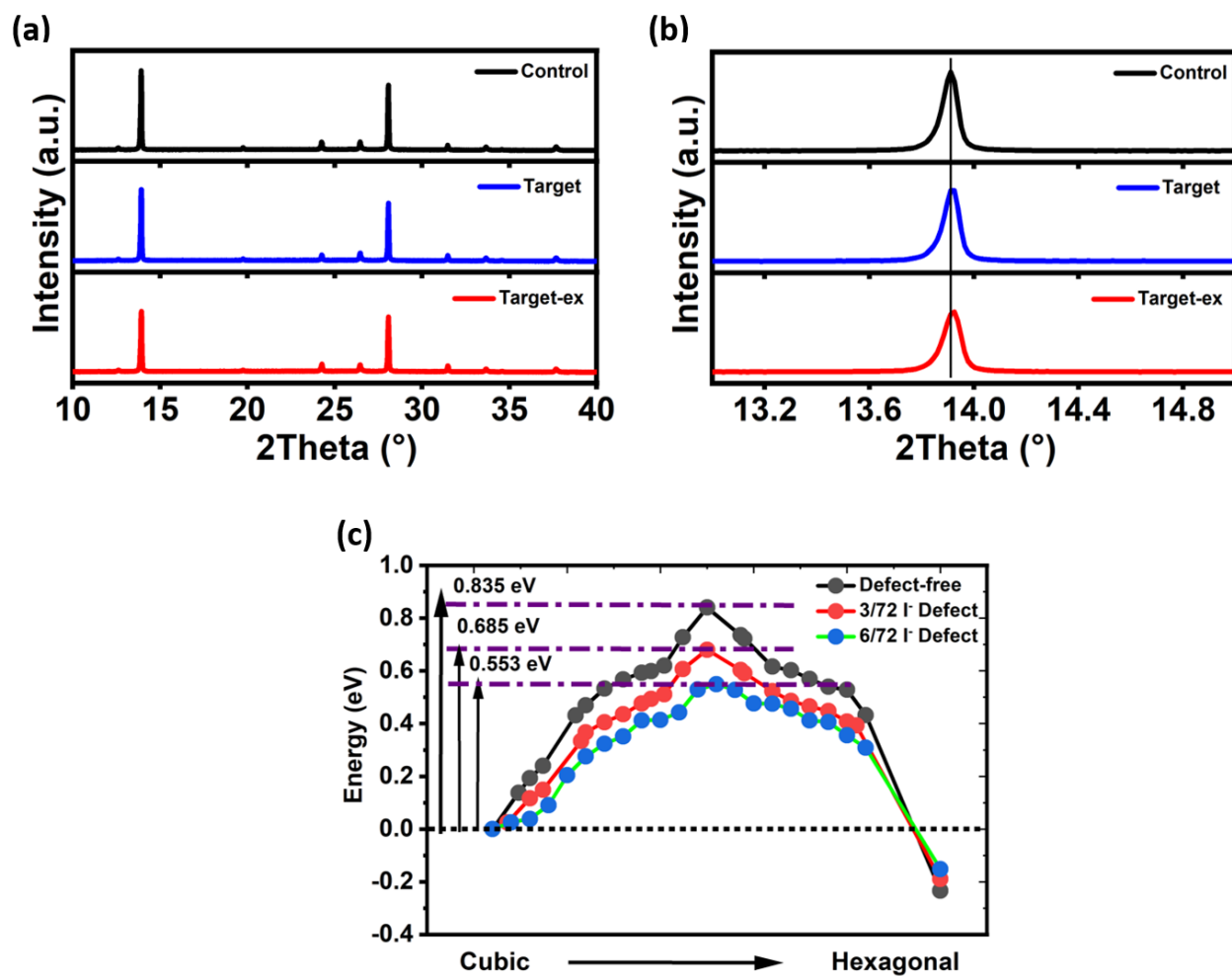


Figure S4.5. (a) and (b) XRD of Control, Target and Target-ex; (c) Effect of V_I defects on the computed energy pathway for the phase transition from the cubic-to-hexagonal phase. These simulations are performed with classical force fields modified from earlier reported studies¹.

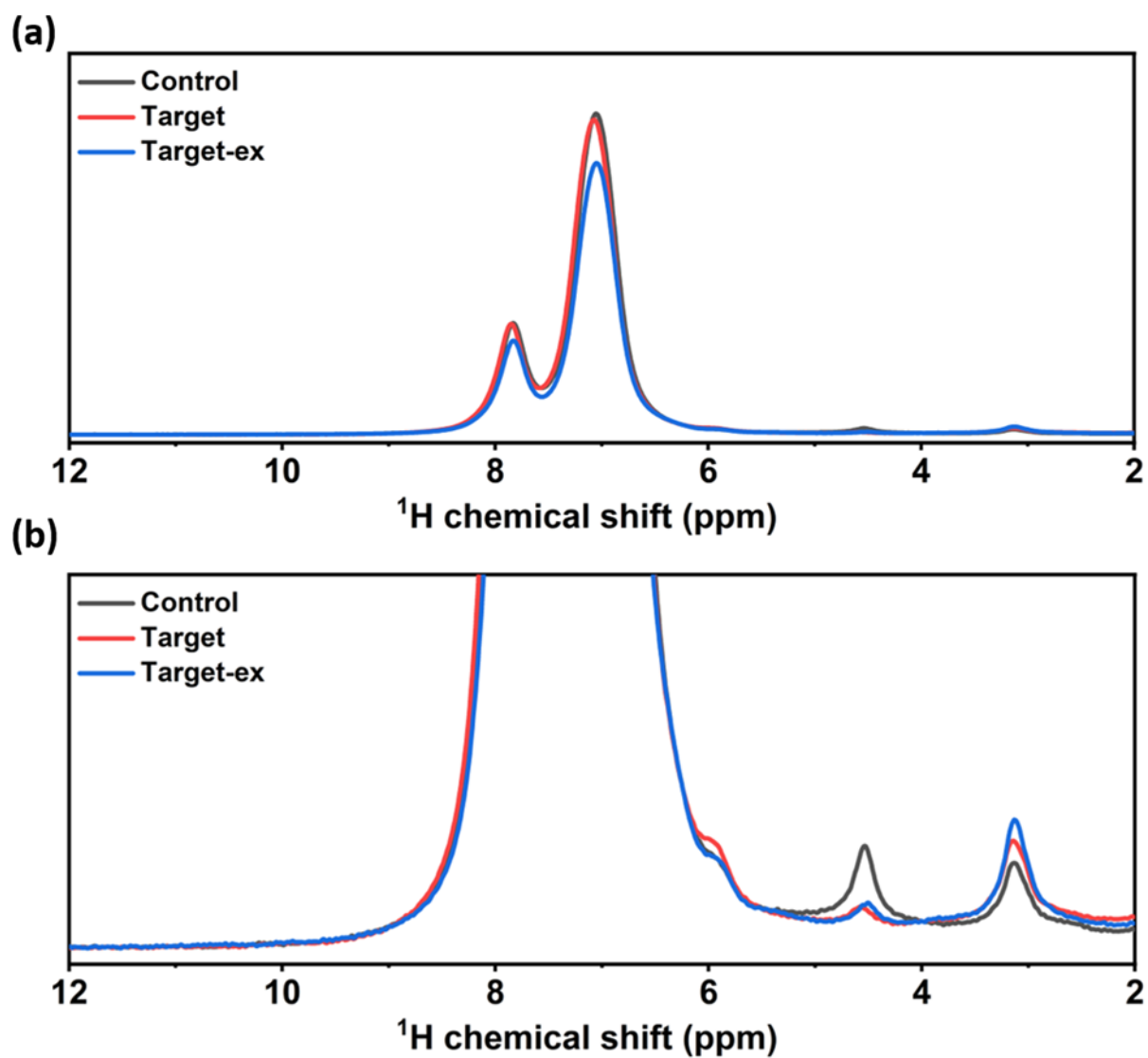


Figure S4.6. Solid-state ^1H MAS NMR measurements at 21.1 T, 300 K and 60 kHz MAS of Control, Target and Target-ex.

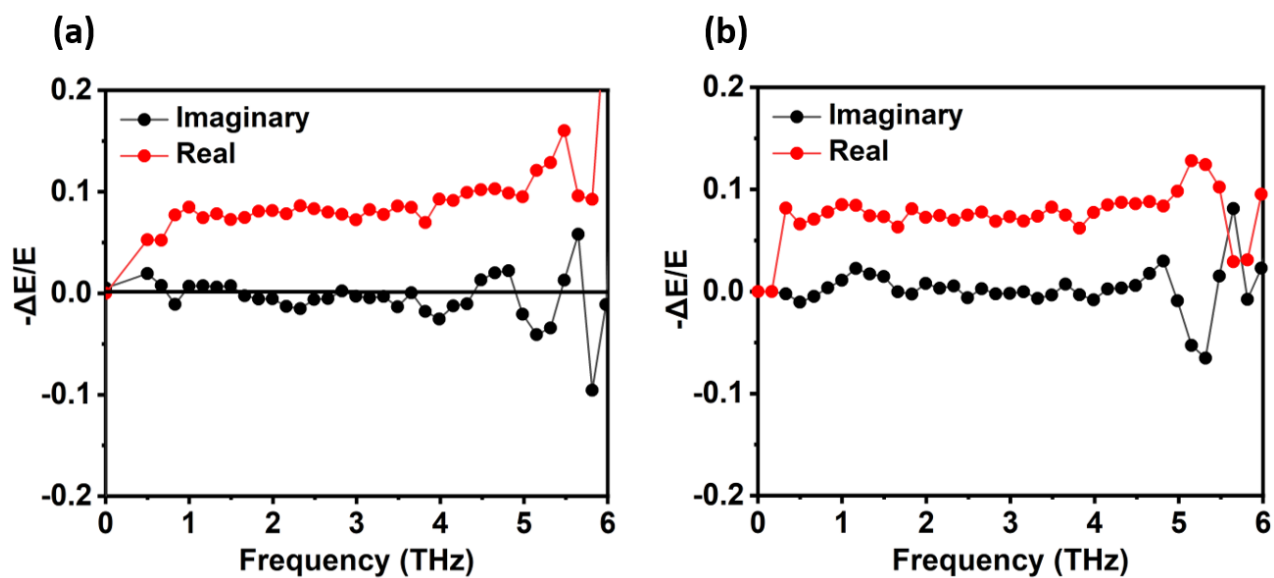


Figure S4.7. The spectra of TRTS for both the control and Target.

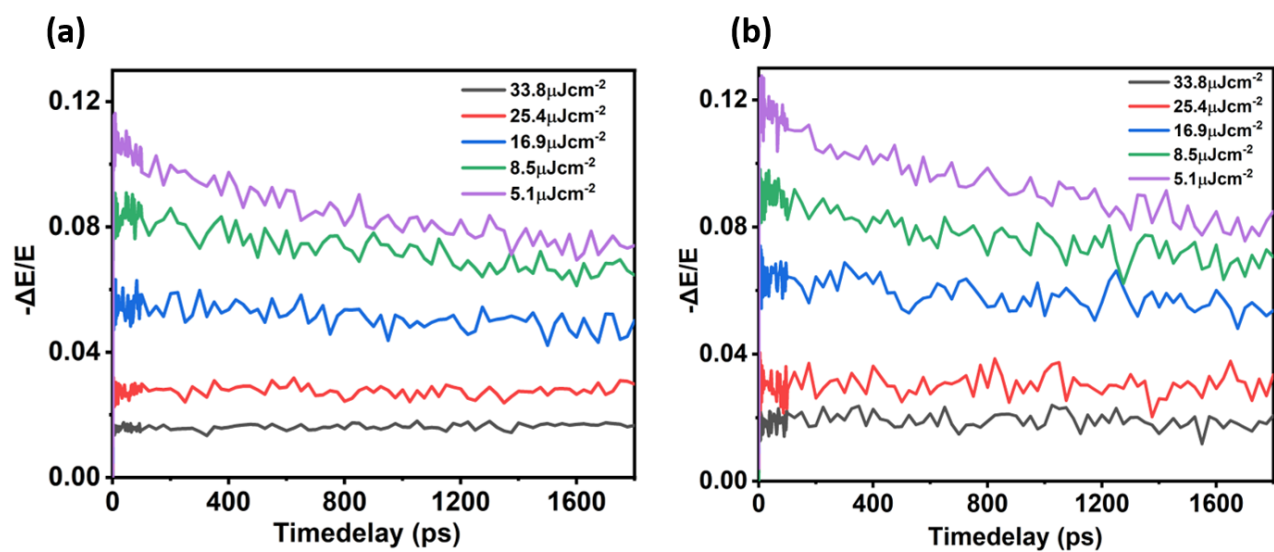


Figure S4.8. The spectra of TRTS for both the control and Target at different fluence.

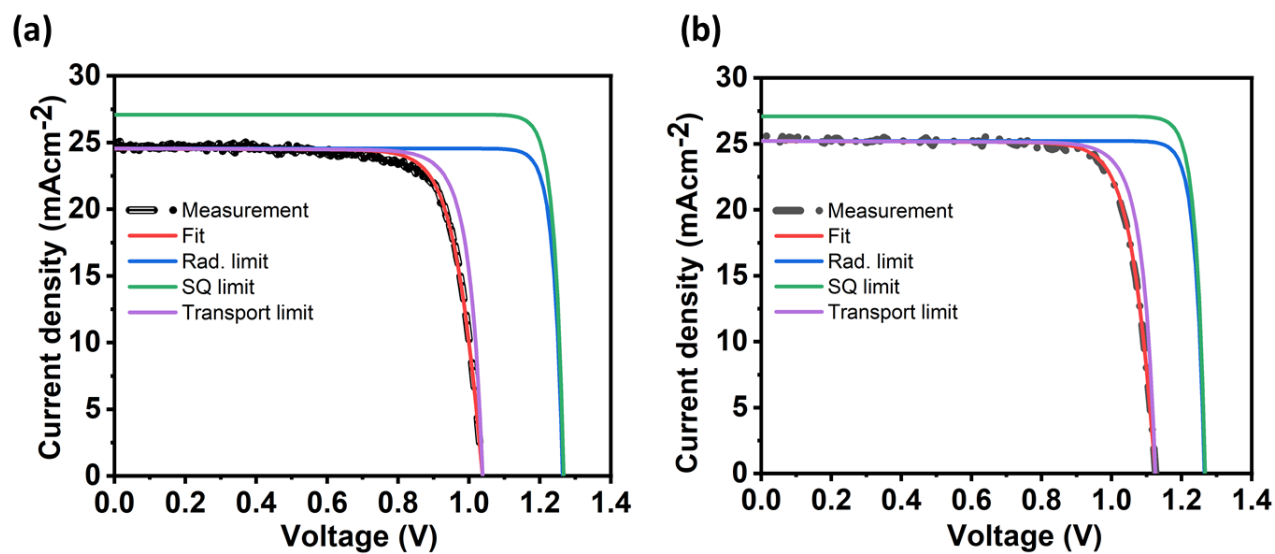


Figure S4.9. J-V curves of measured and simulated devices (a) Control and (b) Target.

Table S4.1. Bulk recombination: TRPL summarized results.

| Condition | τ (ns) | $K1(1/s)$ | L_D (μm) |
|-----------|-------------|-----------|-------------------|
| Control | 2.65 e+02 | 1.95 e+06 | 0.721 |
| Target 1 | 4.84 e+02 | 1.03 e+06 | 1.065 |
| Target 2 | 2.74 e+02 | 1.83 e+06 | 0.779 |

Table S2. Surface recombination: TRPL summarized results.

| Condition | S (cm/s) |
|-----------|------------|
| Control | 118 |
| Target 1 | 62.3 |
| Target 2 | 110 |

Note 1. Calculating the photoconductivity and mobility from TRTS measurements.

THz absorption is typically reported as $-\Delta E/E$, where ΔE is the change in the modulus of the THz field after transmission through the sample and E is the modulus of the incident field. For thin films, where ΔE is typically much smaller than E , this ratio is proportional to the photoconductivity, which itself is proportional to the mobility².

Therefore, by using the following equations, we can calculate the photoconductivity and subsequently the mobility, from the TRTS results.

The photoconductivity, $\Delta\sigma$, can be calculated using the following equation:

$$\Delta\sigma = \frac{-(n_{air} + n_{quartz})\epsilon_0 c}{L} \cdot \frac{\Delta E}{E}$$

Where n_{air} and n_{quartz} are the refractive indices of air and quartz, respectively, ϵ_0 is the vacuum permittivity, c is the speed of light, L is the sample thickness and $\Delta E/E$ is the THz absorption as measured using TRTS.

The photoconductivity can then be used to calculate the mobility, using the following equation:

$$\mu = \frac{\Delta\sigma}{N \cdot e}$$

Where e is the charge of an electron and N is the carrier density. The carrier density, N , is calculated using the following equation:

$$N = f_{ll} N_p \phi$$

Where f_{abs} is the absorptance, measured using an integrating sphere, at the excitation wavelength subtracting the absorptance at 850 nm, N_p is the average photon density on the sample volume and ϕ is the carrier generation yield, assumed to be equal to 2.

Note 2. Estimation of the redox reaction energy

A first rough estimate about the feasibility of the redox reaction between MAI_3 and defect sites in FAPbI_3 discussed in the main text can be obtained from:

$$\Delta E = E_{\text{FAPbI}_3}^{\text{lat}} - E_{\text{Pb}}^{\text{IP}} - E_{\text{I}_3}^{\text{diss}} - E_{\text{I}_2}^{\text{diss}} - 2E_{\text{I}}^{\text{EA}} \text{ where}$$

$E_{\text{FAPbI}_3}^{\text{lat}} = -29.7$ eV/cell is the lattice energy of FAPbI_3 taken from Ref. ³

$E_{\text{Pb}}^{\text{IP}} = E(\text{Pb}^{2+}) - E(\text{Pb}^0) = 7.4 \text{ eV} + 15.0 \text{ eV} = 22.4 \text{ eV}$ ⁴ is the ionisation energy of lead

$E_{\text{I}_3}^{\text{diss}}$ is the dissociation energy of $\text{I}_3^- \Rightarrow \text{I}_2 + \text{I}^- = -1.3 \text{ eV}$ ⁵

$E_{\text{I}_2}^{\text{diss}} = \text{I}_2 \rightarrow 2\text{I}(0) = 1.54 \text{ eV}$ is the dissociation energy of a iodine dimer⁶

and

$E_{\text{I}}^{\text{EA}} = E(\text{I}^-) - E(\text{I}^0) = -3.06 \text{ eV}$ is the electron affinity of iodine⁷.

From this one obtains $\Delta E = -13.2 \text{ eV}$, i.e. the reaction is exothermic.

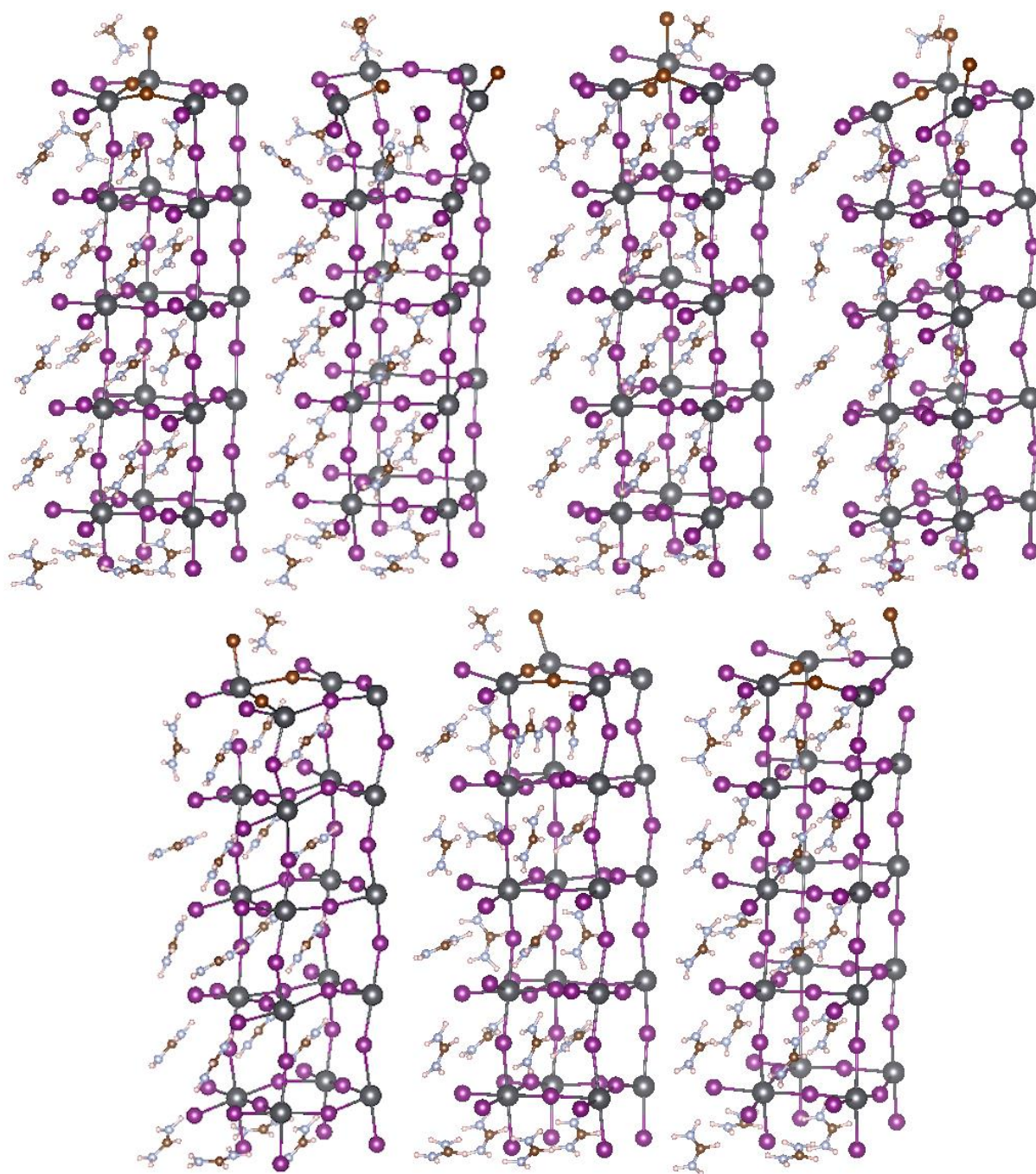


Figure S4.10: The seven obtained relaxed structures starting from different initial configuration of MAI_3 approaching a surface slab of FAPbI_3 with defects. The lowest energy structure is the bottom middle one and is used for the computation of the reaction energy and the Bader charges.

Table S4.3: Bader charges of the four lead atoms on the surface and the three-iodide atoms involved in the addition reaction of MAI_3 to FAPbI_3 , showing that the I atoms originating from MAI_3 transfer in total a charge of 0.87e during the redox reaction.

| | Pb#1 | Pb#2 | Pb#3 | Pb#4 | I#1 | I#2 | I#3 |
|---------------|--------------|--------------|--------------|--------------|---------------|---------------|---------------|
| Initial State | 0.653 | 0.751 | 0.862 | 0.896 | -0.438 | -0.048 | -0.298 |
| Final State | 0.936 | 0.916 | 0.916 | 0.917 | -0.572 | -0.516 | -0.574 |

4.6 Supplementary reference

- 1 A. Mattoni, A. Filippetti, M. I. Saba and P. Delugas, *J. Phys. Chem. C*, 2015, **119**, 17421–17428.
- 2 S. L. Dexheimer, Ed., *Terahertz Spectroscopy: Principles and Applications*, CRC Press, 1st edn., 2008.
- 3 J. M. Frost, K. T. Butler, F. Brivio, C. H. Hendon, M. Van Schilfgaarde and A. Walsh, *Nano Lett.*, 2014, **14**, 2584–2590.
- 4 Lead (Pb) - Chemical properties, Health and Environmental effects, <https://www.lenntech.com/periodic/elements/pb.htm>, (accessed 4 May 2021).
- 5 I3 anion, <https://webbook.nist.gov/cgi/cbook.cgi?ID=B227&Mask=28F>, (accessed 4 May 2021).
- 6 R. J. Leroy, *J. Chem. Phys.*, 1970, **52**, 2678–2682.
- 7 Iodine atom, <https://webbook.nist.gov/cgi/cbook.cgi?ID=C14362448&Mask=20>, (accessed 4 May 2021).

Chapter 5.

Reconfiguring the molecular design for the engineering of bulk and interface enables high efficiency and stable perovskite photovoltaics.

This work still going on.

5.1 Introduction of Designing the ammonium Halide as Passivators.

Ammonium halides have shown great potential as passivators for the interface between metal halide perovskites and HTMs, capable of improving both the quality of the prepared perovskite thin films as well the performance and stability of final devices¹. In this class of small organic passivators, the most commonly used design features an ammonium cation ($R-NH_3^+$) derived from a primary amine ($R-NH_2$) with R representing an alkyl substituent and an I^- counter anion. Their structure is easily tuneable, and they benefit from low production costs and excellent solution processability. Owing to their charged nature, these compounds can form strong interactions with the ionic perovskite material and especially with charged surface defects. The ammonium component is capable of healing negatively charged defects via electrostatic interactions like ionic and hydrogen bonding², whereas the I^- anion serves to passivate halide vacancies³. The combination of these effects leads to significantly reduced charge carrier recombination and therefore improved performances. Alternatively to the formation of a pristine layer of the passivators on the perovskite grains, the use of ammonium halides with the general formula $R-NH_3X$ has also been associated with the formation of 2D perovskite passivation layers on top of the 3D bulk material⁴. Using Cl^- and Br^- instead of I^- has been demonstrated to lead to larger grains with improved morphologies due to slower crystallization rates^{5,6} and increased V_{OC} due to band bending at the interfaces respectively.

However, there's a lack of systematic studies into the molecular design of organic ammonium halide passivators with studies generally focussing on just one or two compounds. Especially

the use of ammonium cations obtained from secondary ($R_1-N(H)-R_2$) and tertiary amines ($R_1-N(R_2)-R_3$) as well as of F^- as counter anion has not received much attention in the past. In this study, we are addressing both these gaps in the current literature following a systematic approach starting from the commonly used passivator octylammonium iodide (OAI; Figure 5.1, first panel)⁷⁻⁹.

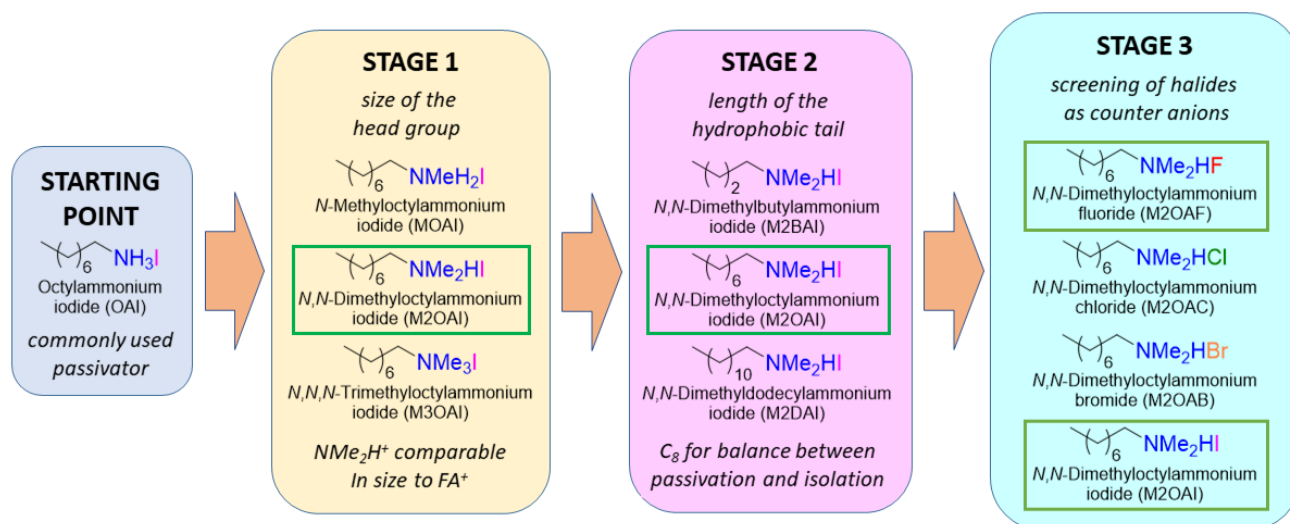


Figure 5.1 Systematic optimization of the organic ammonium halide passivation used in this study starting from the commonly used octylammonium iodide (first panel). At first, the size of the head group was optimized by consecutively replacing all the proton substituents of the ammonium head with methyl groups (second panel). This was followed up with a variation of the length of the hydrophobic tail (third panel) and finally a screening of halide counter anions (fourth panel).

5.2 Photovoltaic performance of the ammonium halide-treated perovskites

Based on what was mentioned in the previous section (octylammonium iodide (OAI; Figure 1, first panel)), we set out to systematically alter its structure in order to improve its properties as a passivator for metal halide perovskites. We employ the state-of-the-art α -FAPbI₃ perovskite with the *n-i-p* device architecture of FTO/c-TiO₂/m-TiO₂/perovskite/spiro-OMeTAD/Au. The molecular strategy at different stages is summarized in Figure 5.1. To begin with, we tested each additive as shown in Fig. 4.1 in the PSCs. For testing of each additive, we incorporated

the additive in the perovskite (α -FAPbI₃) precursor solution which is abbreviated as bulk and we also used the additive for post-treatment of perovskite films which is abbreviated as surface. The best performing additive from each bulk and surface treatment was used together to create a synergistic passivation effect to maximize the performance, and this is abbreviated as bulk/surface. The devices without any additives are referred to as a control. As a starting point (OAI abbreviated as Me0) and during the first stage (Figure 4.1, second panel), we consecutively replaced the proton substituents of the ammonium cation with methyl groups, thereby increasing the size of the head group. The introduction of the first two methyl groups (MOAI abbreviated as Me1, M2OAI abbreviated as Me2) led to a continuous improvement in device performance as shown in Figure 5.2, whereas the Me2 showed a PCE as high as 22.82% and 22.10% in the bulk and surface, respectively, as compared to the 21.16% PCE of the control. This was a highly unexpected result, as it was previously thought that a tertiary ammonium head group would be too large to effectively passivate surface defects of perovskite thin films. Replacing the third proton with a methyl group (M3OAI abbreviated as Me3), however, had a detrimental effect on the performance (Figure 5.2). Two interpretations of this observation are possible; either the further increased size of the ammonium head group was now preventing it from efficiently interacting with the perovskite or the presence of at least one proton is critical for strong interaction with the perovskite via hydrogen bonding (*vide infra*). After having determined the ideal head group composition (Me2), we systematically varied the length of the hydrophobic tail from a C₄ (M2BAI) to a C₁₂ carbon chain (M2DAI; Figure 1, third panel). This screening was intended to find a balance between the enhanced hydrophobicity that comes with a longer carbon chain leading to improved moisture resistance of the passivated thin films on one hand and the increasing barrier for charge carrier transfer to the HTM on the other. In line with earlier results from the literature, we found the C₈ chain in Me2 (Figure 5.2) to give the best results⁷. In the final step of our study, we screened F⁻

(M2OAF), Cl^- (M2OAC) and Br^- (M2OAB) in addition to I^- (M2OAI) to study the effect of the halide counter anion on thin-film morphology as well as device performance and stability. This revealed M2OAI to be the best performing passivator in the case of subsequent application onto the as-prepared $\alpha\text{-FAPbI}_3$ films (bulk). However, when premixing these compounds directly with the perovskite precursor, M2OAF gave superior results compared to M2OAI as surface passivated perovskite (Figure 5.2) with a PCE of 23.0%.

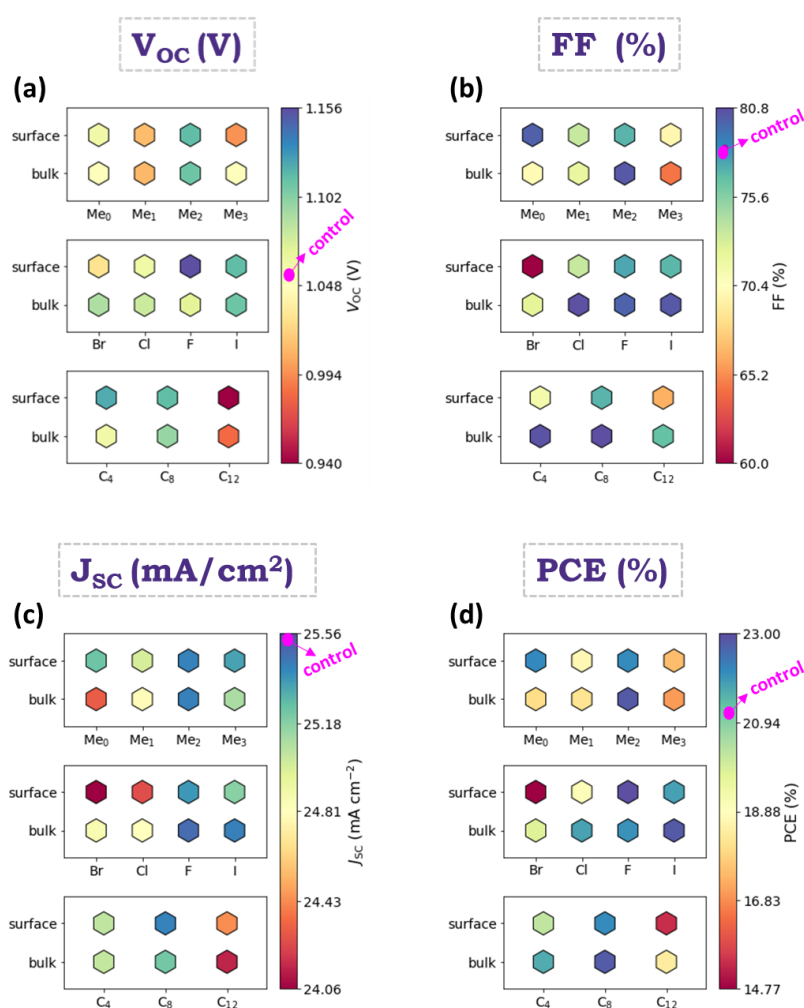


Figure 5.2 (a), (b), (c), and (d) Summary of J - V results of control, surface, and bulk for the optimization with different molecules.

Finally, we combined the best performing bulk and surface additives, i.e M2OAI additive in the bulk and the post-treatment of the surface with M2OAF. This synergistic combination of bulk and surface passivation led to a significant improvement in the performance with a PCE of 24.91% with a remarkable FF of 84.6% as shown in Table 5.1 and Figure 5.3a. After screening the additives, we can see that the best results are obtained with M2OAX (X=I and F). From here on, we performed in-depth investigations to unravel the mechanism behind performance enhancement with these additives.

Table 5.1 Summary of the best performance of Control and Target in backward scan (BK) and forward scans (FWD)

| Control | | | | |
|----------------|--------------|--------------------------------|--------|---------|
| | V_{oc} (V) | J_{sc} (mA/cm ²) | FF (%) | PCE (%) |
| BK | 1.055 | 25.52 | 78.50 | 21.16 |
| FWD | 0.984 | 25.48 | 78.00 | 19.68 |
| Target | | | | |
| | V_{oc} (V) | J_{sc} (mA/cm ²) | FF (%) | PCE (%) |
| BK | 1.146 | 25.62 | 84.60 | 24.91 |
| FWD | 1.134 | 25.60 | 82.00 | 24.04 |

We performed the backward and forward scans to examine the hysteresis in the Control and Target devices (Fig. 5.3a). The Control device shows a PCE of 21.16 % in the backward scan and 19.68% in the forward scan, whereas the Target shows a PCE of 24.91% in the backward and 24.04% in the forward scan. Figure 5.3a shows the devices during maximum power point tracking (MPP) in ambient air (15-25% RH (relative humidity)) under one sun illumination for 300 sec. The MPP tracking for the Control and Target is 20.28% and 24.45% respectively (Fig. 5.3b). Overall, there was a significant decrease in the hysteresis in the Target devices. The incident photon-to-current efficiency (IPCE) spectra and integrated current density (Fig. 5.3c) of the target device show almost no change in the onset of the IPCE spectra. In addition, the statistical distribution of the photovoltaic characteristics (J_{sc} , V_{oc} , FF, and PCE) is presented in Figure 5.3d, which shows improvement in all device parameters. The cross-section morphology of the Control and Target (Figure 5.3e) was characterized by scanning electron microscopy (SEM). The SEM images showed a well-stacked perovskite layer with a thickness of ~ 620 nm.

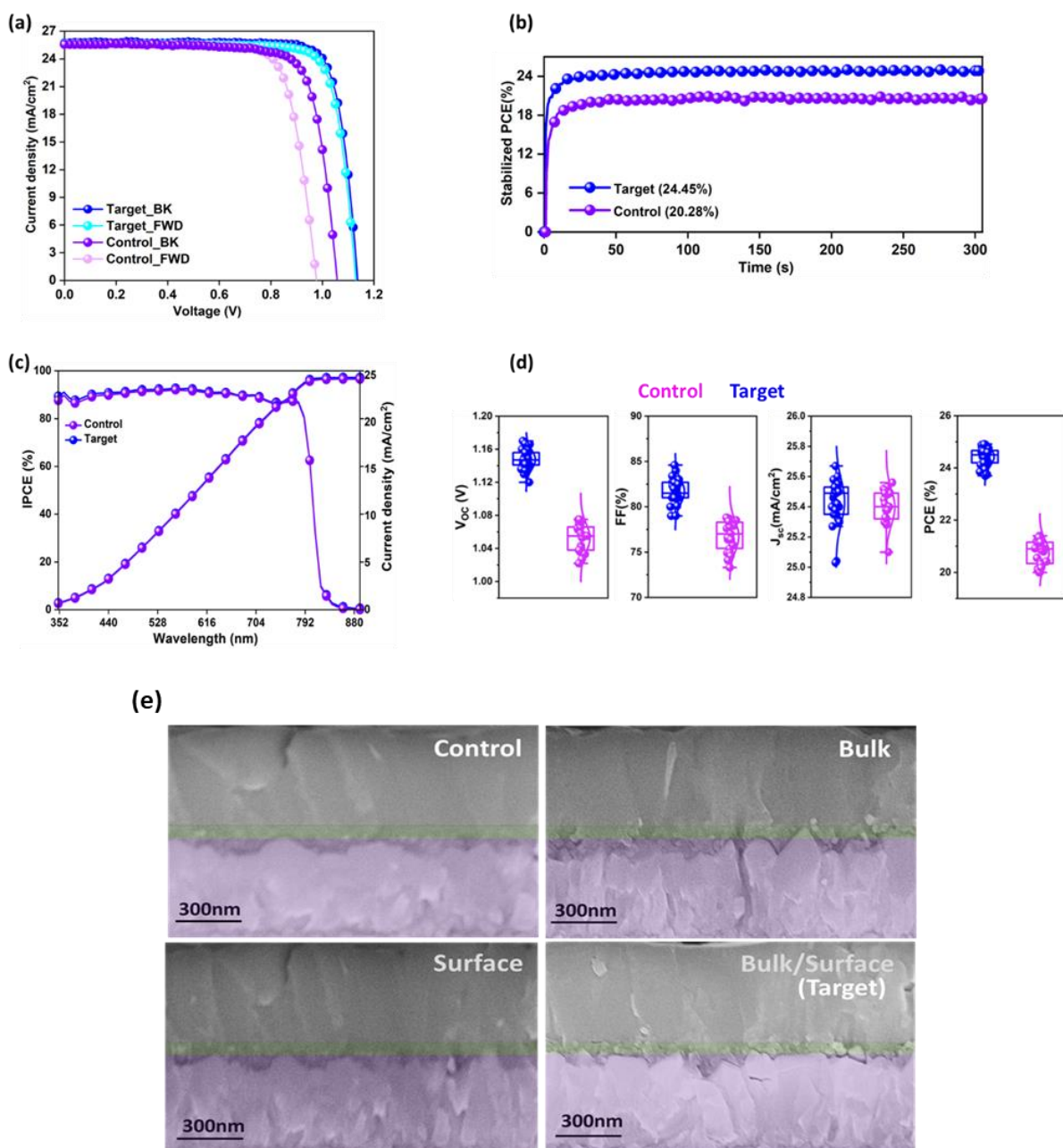


Figure 5.3 (a) J-V curves of the devices at backward and forward scan, (b) maximum power point tracking for Control and Target (c) IPCE spectra and photocurrent integrated over the standard AM 1.5G solar spectrum, (d) J-V metrics of Control and Target devices, respectively, (e) Cross-sectional SEM images of Control, bulk, surface, and Target devices, respectively.

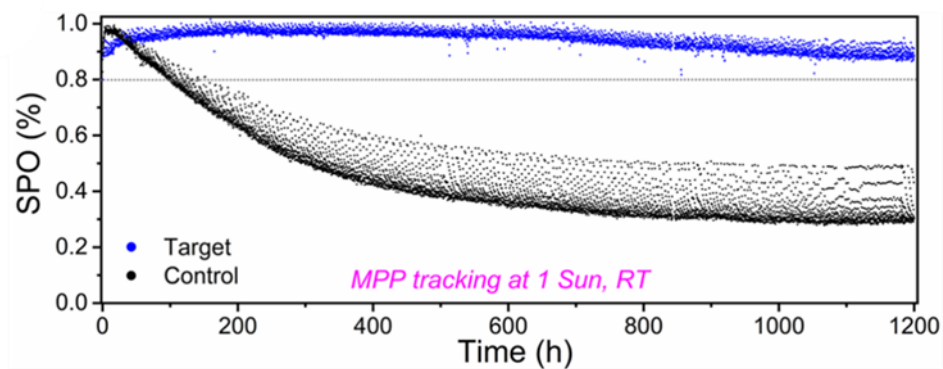


Figure 5.4 (a) Operational stability in a nitrogen environment at room temperature under continuous illumination (White LED, 1 Sun) at maximum power point for Control and Target, respectively.

Operational stability remains a major concern in perovskite solar cells. The operational stability of the Control and Target was studied by subjecting them to under full illumination in a nitrogen atmosphere at RT for 1200 h with continuous maximum power point tracking (MPPT). The Control and Target retained 25% and 85% of the initial performance after 1200 hours, respectively (Figure 5.4).

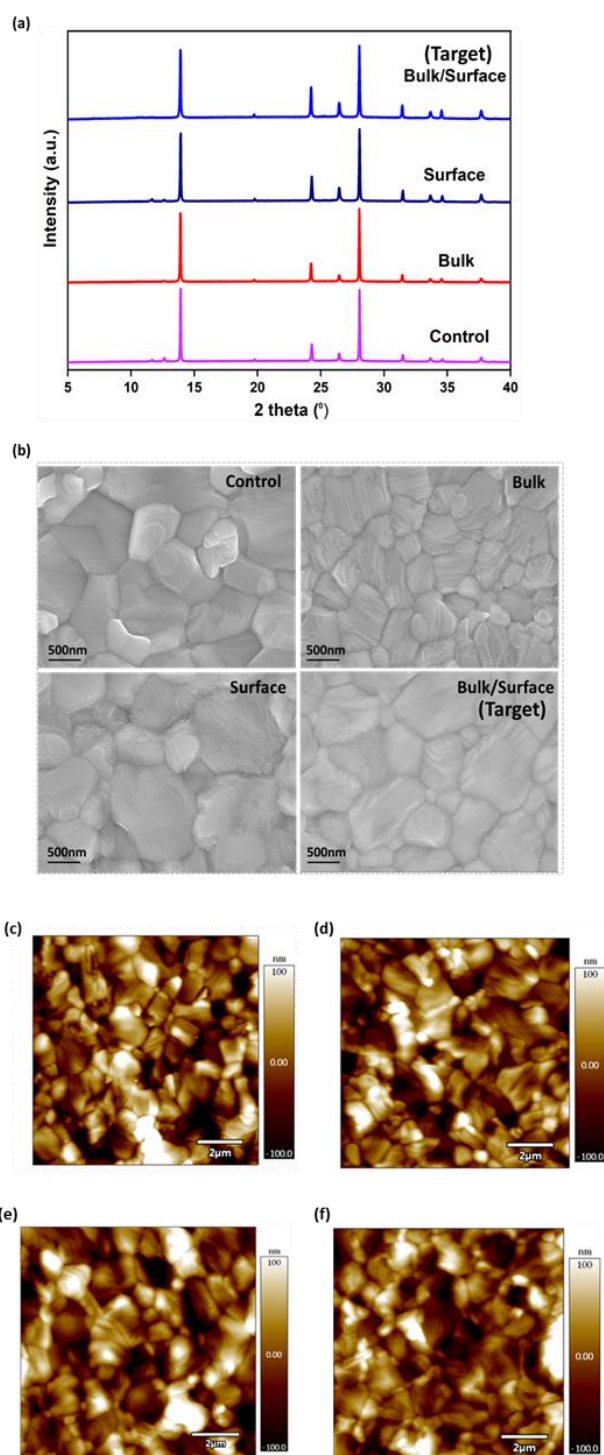


Figure 5.5 (a) XRD patterns, and (b) top view SEM images of Control, bulk, surface, and Target films, respectively, (c-f) AFM images for Control, bulk, surface, and Target films, respectively,

The effect of the additives on the structure of perovskite films was analyzed by X-ray diffraction (Figure 5.5a). We find that the PbI_2 peak at 12.5° preserved in control, bulk and surface but when incorporating the bulk and surface treatment to the perovskite film (Target) together, the PbI_2 peak completely disappeared which indicates that PbI_2 has been fully reacted with perovskite despite the perovskite precursor has a 3% PI_2 excess. The control film shows the peak at 11° which corresponds to the photo-inactive delta phase. Upon the addition of M2OAI (bulk) and bulk/surface (Target), the delta phase has disappeared as compared to control and surface. This means indeed the addition of M2OAI into the precursor solution improved the phase and the crystallinity of perovskite film. The surface morphology in the SEM images (Figure 5.5b) shows that both Control, bulk, surface, and Target perovskite films are uniform and highly crystalline with similar compact textures and grain sizes of hundreds of nanometers, whereas the surface perovskite film showed a clear characteristic of the coating layer. We then investigate the surface roughness of the perovskite films with and without the additives using atomic force microscopy (AFM) (Figure 5.5c-f). The control film showed a surface roughness of 54.5 nm whereas all the treated samples showed a lower roughness viz., 48.2 nm, 40.9 nm, and 47.1 nm for control, bulk, surface, and Target, respectively. The lowest surface roughness is observed in the case of the surface-treated film which indicates that surface passivation makes the surface smoother which can be beneficial for improving the interfacial contact with the adjacent layer¹⁰.

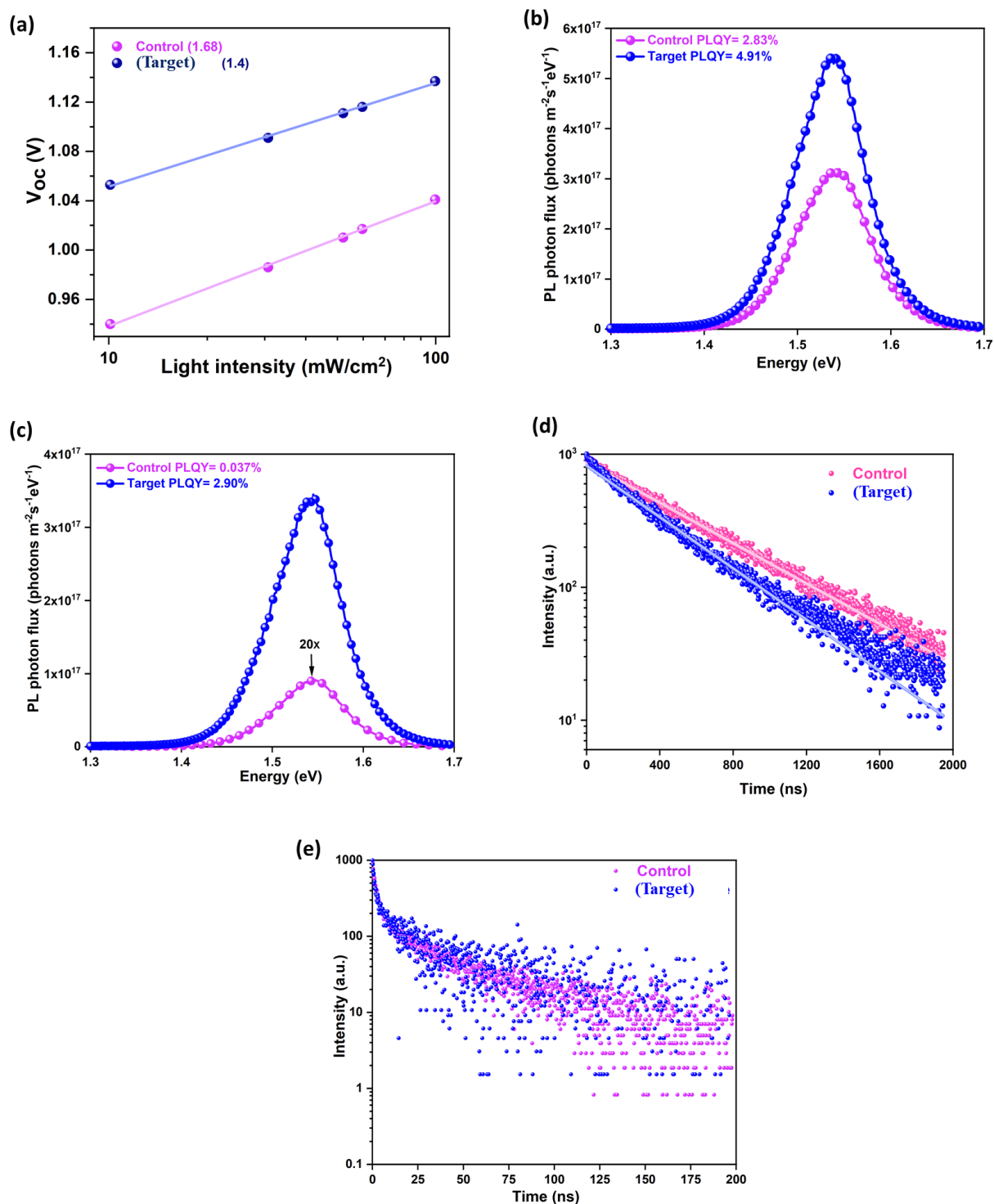


Figure 5.6 (a) Open circuit voltage (V_{oc}) at a different light intensity, (b), and (c) Absolute photon flux measurements of complete devices at 1 sun excitation from which the PLQY is determined with and without Spiro-OMeTAD, respectively. (d), (e) Time-resolved photoluminescence (TRPL) measurements of Control and Target, with and without Spiro-OMeTAD (hole transporting layer), respectively.

To get more insight on the device physics for understanding the role of nonradiative recombination, we measured the ideality factor (n_{id}) by taking the dependence of V_{OC} as a function of incident light intensity. As shown in Figure 5.6a, the n_{id} decreases from 1.68 to 1.4, for control and Target, respectively, which indicates a substantial reduction of non-radiative recombination. We next measured absolute photoluminescence (PL) photon fluxes $\Phi_{PL}(E)$ of Control and Target films (Figure 5.6b,c) and devices (i.e. with Spiro-OMeTAD) to understand the V_{OC} loss from both bulk and interfaces.¹¹ The photoluminescence quantum yields (PLQY) data is summarized in Table 5.2. The enhancement in the PLQY for the Target films and devices indicates suppression of non-radiative recombination in the bulk of the perovskite as well as at the interface. To gain further insights into the charge carrier dynamics, we performed time-resolved photoluminescence spectroscopy (TRPL) of films and devices using laser excitation pulses of low fluences ($<5\text{ nJ/cm}^2$) so that bimolecular and Auger recombination are negligible¹². The TRPL of the device shows a very similar decay feature, which suggests that the passivation did not hamper the charge transfer process (Figure 5.6d,e). Overall, these results, acquired from PV device, n_{id} , PLQY, and TRPL measurements indicate that the synergistic passivation (bulk/surface) strategy reduces the non-radiative recombination rate, leading to improvements in both V_{OC} and FF.

Table 5.2 PLQY summarized results.

| Sample | | PLQY (%) | PL peak (eV) | $V_{OC,rad}$ (V) | $V_{OC,PLQY}$ (V) | $V_{OC,loss}$ (mV) |
|---------|------------------------------|----------|--------------|------------------|-------------------|--------------------|
| Control | Perovskite | 2,83 | 1.543 | 1.258 | 1,166 | 92 |
| | Perovskite with spiro-MeOTAD | 0,037 | 1,545 | 1,262 | 1,058 | 204 |
| Target | Perovskite | 4,91 | 1,541 | 1,255 | 1,177 | 78 |
| | Perovskite with spiro-MeOTAD | 2,90 | 1,545 | 1,259 | 1,167 | 92 |

Table 5.3 TRPL summarized results.

| Condition | τ (ns) | $K_1(1/s)$ |
|-----------|-------------|------------|
| Control | 5.72 e+02 | 8.73 e+05 |
| Target | 4.50 e+02 | 1.11 e+6 |

5.3 Conclusion

In this study, we reconfigured the molecular design of the alkylammonium halide passivators. We followed a systematic approach starting from the commonly used passivator octylammonium iodide (OAI). We showed that dimethylammonium head along with octyl chain and iodide counter anion works best in the bulk whereas dimethylammonium head along with octyl chain and fluoride counter anion works best at the surface. With a synergistic combination of both bulk and surface passivation, we achieved a high PCE of 24.91% along with exceptional long-term operational stability. This systematic molecular reconfiguration strategy and scientific outcomes from this work will be beneficial for ongoing development of the metal halide perovskites.

5.4 References

- 1 S. Akin, B. Dong, L. Pfeifer, Y. Liu, M. Graetzel and A. Hagfeldt, *Adv. Sci.* (Weinheim, Baden-Wurttemberg, Ger., 2021, **8**, 2004593.
- 2 H. Lu, A. Krishna, S. M. Zakeeruddin, M. Grätzel and A. Hagfeldt, *iScience*, 2020, **23**, 1–14.
- 3 P. Chen, Y. Bai and L. Wang, *Small Struct.*, 2021, **2**, 2000050.
- 4 A. Krishna, S. Gottis, M. K. Nazeeruddin and F. Sauvage, *Adv. Funct. Mater.*, 2019, **29**, 1806482.
- 5 S. T. Williams, F. Zuo, C. C. Chueh, C. Y. Liao, P. W. Liang and A. K. Y. Jen, *ACS Nano*, 2014, **8**, 10640–10654.
- 6 K. Odysseas Kosmatos, L. Theofylaktos, E. Giannakaki, D. Deligiannis, M. Konstantakou and T. Stergiopoulos, *Energy Environ. Mater.*, 2019, **2**, 79–92.
- 7 H. Kim, S. U. Lee, D. Y. Lee, M. J. Paik, H. Na, J. Lee and S. Il Seok, *Adv. Energy Mater.*, 2019, **9**, 1–8.
- 8 S. M. Yoon, H. Min, J. B. Kim, G. Kim, K. S. Lee and S. Il Seok, *Joule*, 2021, **5**, 183–196.
- 9 J. Jeong, M. Kim, J. Seo, H. Lu, P. Ahlawat, A. Mishra, Y. Yang, M. A. Hope, F. T. Eickemeyer, M. Kim, Y. J. Yoon, I. W. Choi, B. P. Darwich, S. J. Choi, Y. Jo, J. H. Lee, B. Walker, S. M. Zakeeruddin, L. Emsley, U. Rothlisberger, A. Hagfeldt, D. S. Kim, M. Grätzel and J. Y. Kim, *Nature*, 2021, **592**, 381–385.
- 10 G. Yang, Z. Ren, K. Liu, M. Qin, W. Deng, H. Zhang, H. Wang, J. Liang, F. Ye, Q. Liang, H. Yin, Y. Chen, Y. Zhuang, S. Li, B. Gao, J. Wang, T. Shi, X. Wang, X. Lu, H. Wu, J. Hou, D. Lei, S. K. So, Y. Yang, G. Fang and G. Li, *Nat. Photonics*, , DOI:10.1038/s41566-021-00829-4.
- 11 J. C. de Mello, H. F. Wittmann and R. H. Friend, *Adv. Mater.*, 1997, **9**, 230–232.
- 12 T. Kirchartz, J. A. Márquez, M. Stolterfoht and T. Unold, *Adv. Energy Mater.*, 2020, **10**, 1904134.

5.5 Experimental Methods

5.5.1 Device fabrication: Fluorine-doped tin oxide (FTO)-glass substrates (TCO glass, NSG 10, Nippon sheet glass, Japan) were itched and cleaned by ultrasonication in Hellmanex (2%, deionized water), rinsed thoroughly with de-ionized water and ethanol, and then treated in oxygen plasma for 30 min. Approximately, 30 to 25 nm blocking layer (TiO_2) was sprayed on the cleaned FTO at 450 °C using a commercial titanium diisopropoxide bis(acetylacetonate) solution (75% in 2-propanol, Sigma-Aldrich) diluted in anhydrous ethanol (1:10 volume ratio). A 150 nm mesoporous TiO_2 layer (diluted paste (1:6.5 wt. ratio) (Dyesol 30NRD: ethanol)) spin-coated at 5000 rpm for 15 s and then sintered at 450 °C for 30 min in dry air. The perovskite films were deposited using a single-step deposition method from the precursor solution which was prepared in Argon atmosphere and containing 1.45 M of FAI, PbI_2 , and in anhydrous dimethylformamide/ dimethylsulphoxide (4:1 (volume ratio)) to achieve the desired composition: FAPbI_3 (3% PbI_2 excess+ 35 mmol% of MACl). For the additives, in case of mixing with perovskite precursor, 0.1 M was made and added to the perovskite precursor at different concentrations. The device fabrication was carried out inside a dry air box, under controlled atmospheric conditions. Perovskite solution was spin-coated in a one-step program at 5000 rpm. 270 μl of chlorobenzene was dropped on the spinning substrate. This was followed by annealing the films at 150 °C for 35 to 40 min. After cooling down, in case of passivation different concentration for each additive which was dissolved in IPA was deposited on the perovskite film at the substrate films at 5000 rpm. For completing the fabrication of devices, 90 mg of 2,2',7,7'-tetrakis(*N,N*-di-*p*-methoxyphenylamine)-9,9-spirobifluorene (spiro-OMeTAD) was dissolved in 1 ml of chlorobenzene as a hole-transporting material (HTM). The HTM was spin-coated at 5000 rpm for 30 s. The HTM was doped with bis(trifluoromethylsulfonyl)imide lithium salt (23.2 μl prepared by dissolving 520 mg LiTFSI

in 1 ml of acetonitrile), and 36 μ l of 4-tert-butylpyridine. Finally, a ~80 nm gold (Au) layer was thermally evaporated.

5.5.2 Device characterization: The current-voltage (*J-V*) characteristics of the perovskite devices were recorded under ambient temperature and air conditions with a digital source meter (Keithley model 2400, USA). A 450 W xenon lamp (Oriel, USA) was used as the light source for photovoltaic (*J-V*) measurements. The spectral output of the lamp was filtered using a Schott K113 Tempax sunlight filter (Präzisions Glas & Optik GmbH, Germany) to reduce the mismatch between the simulated and actual solar spectrum to less than 2%. The light intensity was ranging between 0.98 to 1Sun. The photo-active area of 0.158 cm² was defined using a dark-colored metal mask.

5.5.3 Incident photon-to-current efficiency (IPCE): was recorded under a constant white light bias of approximately 5 mW cm⁻² supplied by an array of white light-emitting diodes. The excitation beam coming from a 300 W Xenon lamp (ILC Technology) was focused through a Gemini-180 double monochromator (Jobin Yvon Ltd) and chopped at approximately 2 Hz. The signal was recorded using a Model SR830 DSP Lock-In Amplifier (Stanford Research Systems).

5.5.4 Scanning electron microscopy (SEM): SEM was performed on a ZEISS Merlin HR-SEM.

5.5.5 X-ray powder diffractions: X-ray patterns were recorded on a Bruker D8 Discover (Cu anode, $\lambda = 1.54060$ Å) in Bragg Brentano geometry, equipped with a Johansson $K\alpha_1$ monochromator and a Lynxeye XE detector. Lattice parameters were extracted from profile fitting using Topas 5.

5.5.6 Time-resolved photoluminescence (TRPL): The photoluminescence lifetime was measured via time-correlated single-photon counting (TCSPC) using a LifeSpec II (Edinburgh Instruments) fluorescence spectrometer with a picosecond pulsed diode laser (EPL-510, Edinburgh Instruments) at 510 nm wavelength, 85 ps pulse width, and 4.5 nJ/cm² fluence.

5.5.7 Long-term light soaking test: Stability measurements were performed with a Biologic MPG2 potentiostat under a full AM 1.5 Sun-equivalent white LED lamp. The devices were measured

with a maximum power point (MPP) tracking routine under continuous illumination at room temperature. The MPP was updated every 10 s by a standard perturb and observe method. Every minute a *JV* curve was recorded in order to track the evolution of individual *JV* parameters.

5.5.8 Photoluminescence quantum yield (PLQY): PLQY was acquired following the procedure suggested by de Mello¹¹. The samples were excited using a continuous-wave laser (OBIS LX, 660 nm) whose power was adjusted to match the photogeneration rate under 1Sun illumination (0.324 mW, 0.786mm effective beam FWHM). Signal was collected using an integrating sphere (Gigahertz Optik, UPB-150-ARTA) connected via a multimode, 400 μm diameter optical fiber (Thorlabs BFL44LS01) to a spectrometer (Andor, Kymera 193i). The system was spectrally calibrated using an irradiance calibration standard lamp (Gigahertz Optik, BN-LH250-V01).

Chapter 6

Conclusion

Perovskite solar cells have become one of the most candidates in photovoltaic technology due to their exceptional properties and low cost of materials which shows indeed rapid progress in power conversion efficiency in a short period of time. However, still many drawbacks remain behind this progress, which particularly refers to the possibility of more improvement in the stability of PSCs. The studies involved in this thesis mainly focusing on compositional and interfacial engineering towards obtaining highly efficient and stable perovskite solar cells.

In chapter 2, we investigated the effect of guanidinium iodide incorporation into mixed-cation and mixed-halides perovskite films. A gradual increase in the content of Gual shows a significant enhancement of the open-circuit voltage from 1.13 V to 1.20 V leading to the realization of >20.3% PCE. The photoluminescence and lifetime of charge carriers observed in Gual containing perovskite films were maintained in the fully assembled device, justifying the trends in the V_{OC} as well as the EQE_{EI} showed an improvement four times higher than the control. Our study shows that there is still plenty of room to improve PCE to new record levels by strategically maneuvering the precursor chemistry.

In chapter 3, we applied a straightforward strategy to reduce the undesirable surface defects via different ammonium salts (i.e. EAI, IAI, and Gual) as surface passivation agents on mixed-cation and mixed-halide perovskite films. Solid-state NMR has evidenced that they form a tightly adhering low-dimensionality passivation layer of on the preexisting perovskite grains. The introduction of these buffer layers showed a significant enhancement of the open-circuit voltage by 30 mV (EAI), 70 mV (IAI), and 40 mV (Gual), leading to the realization of

PCEs as high as 22.3%, 22.1%, and 21.0% for EAI, IAI, and Gual-treated devices, respectively. EAI and IAI showed an improvement also on the FF (+3.5% and +2%, respectively) with EAI reaching a FF of 81% on the best performing device. In contrast to the control sample, all passivated devices, after an initial drop, stabilized their efficiency with the EAI-treated device only losing 5% of its initial value after 550 h of MPP tracking. This work exemplifies the importance of interface engineering for perovskite solar cells and should stimulate other successful developments in the future.

In chapter 4, we employed MAI₃ as an additive in the perovskite precursor solution of metal halide perovskite absorber, affording passivation of Pb⁰ and charged defects as proven by XPS measurement which leads to suppression of non-radiative recombination. TRTS, PV device loss analysis, n_{id} , PLQY, and TRPL measurements indicate that the addition of MAI₃ simultaneously reduces the non-radiative recombination rate and increases the charge carrier mobility, leading to the observed improvements in both V_{OC} and FF. As a result, we achieve a PCE exceeding 23% with the MAI₃ modulated Target which also exhibits a remarkable improvement in stability with respect to the Control regardless of the external aging conditions (high temperature, ambient, MPP). This facile strategy provided in this work has the potential to stimulate other successful developments in the future.

In chapter 5, we reconfigured the molecular design of the alkylammonium halide passivators. We followed a systematic approach starting from the commonly used passivator octylammonium iodide (OAI). We showed that dimethylammonium head along with octyl chain and iodide counter anion works best in the bulk whereas dimethylammonium head along with octyl chain and fluoride counter anion works best at the surface. With a synergistic combination of both bulk and surface passivation, we achieved a high PCE of 24.91% along with exceptional long-term operational stability. This systematic molecular reconfiguration

strategy and scientific outcomes from this work will be beneficial for ongoing work on the metal halide perovskites.

In summary, we employed different strategies based on organic ammonium salts to engineer the bulk and interface of the PSCs. We did an in-depth investigation of the optoelectronic properties, local structure, and molecular interactions with a combination of characterization at different length and time scales. Our results show that it is imperative to passivate both bulk and interface defects for obtaining high efficiency and stable solar cells. From our work, one can take inspiration from the design and analysis of new materials for the passivation of the PSCs.

Curriculum Vitae (CV)

Essa A. Alharbi

📍 Av. de Prefaully, 1022 Chavannes, Renens, Switzerland.

☎ +41 766230739

📧 essa.alharbi@epfl.ch , e.alfaridi@gamil.com

[ESSA A. ALHARBI - Google Scholar](#)

Date of Birth: 03/04/1987 | **Nationality:** Saudi

Education

| | |
|--------------------------------|---|
| 20.09.2016 – 04.10.2021 | Ph.D. in Photonics doctoral programme Laboratory of Photonics and Interfaces, Institute of Chemical Sciences and Engineering, School of Basic Sciences École Polytechnique Fédérale de Lausanne Thesis: Compositional and interfacial optimization for enhancement of perovskite solar cells performance Supervisors: Prof. Michael Grätzel and Co-supervisor: MER. Dr. Shaik M. Zakeeruddin |
| 2013–2015 | Master's degree in physics-material Science King Saud University in Riyadh, Saudi Arabia Thesis: Synthesis, Physiochemical characterization and biological response of Iron oxide NPs. |
| 20.09.2016–04.10.2021 | KACST PhD Fellow École Polytechnique Fédérale de Lausanne Laboratory of Photonics and Interfaces Supervisor: Prof. Michael Grätzel Project: Compositional and interfacial optimization for enhancement of perovskite solar cells performance |
| 2015–present | Scientific Researcher National Center for Nanotechnology King Abdulaziz City for Science and Technology (KACST) in Riyadh, Saudi Arabia. |
| 2008–2015 | Physics teacher Diplomatic Quarters High School in Riyadh Ministry of education, Saudi Arabia |

Publication List

Manuscript published

1. **Alharbi, E.A.**, Alyamani, A.Y., Kubicki, D.J. Alexander R.Uhl. Walder, B. J., Alanaz, A. Luo J., Andrés B. C., Albadri, A., Albrithen, H., Alotaibi, Mohammad. H., Moser, Jacques-E., Zakeeruddin, S. M., Giordano, F., Lyndon Emsley, Michael Grätzel *et al.* Atomic-level passivation mechanism of ammonium salts enabling highly efficient perovskite solar cells. **Nat Commun.** **10**, 3008 (2019).
2. **Alharbi, E.A.**, Baumeler, T. P., Krishna, A., Alyamani, A. Y., Eickemeyer, F. T., Ouellette, O., Pan, L., Alghamdi, F. S., Wang, Z., Alotaibi, M. H., Yang, B., Almalki, M., Mensi, M. D., Albrithen, H., Albadri, A., Hagfeldt, A., Zakeeruddin, S. M., Michael Grätzel , Formation of High-Performance Multi-Cation Halide Perovskites Photovoltaics by δ -CsPbI₃/ δ -RbPbI₃ Seed-Assisted Heterogeneous Nucleation. **Adv. Energy Mater.** **2021**, **11**, 2003785.
3. **Alharbi, E. A.**, Krishna, A., Baumeler, T. P., Dankl, M., , George C., , Eickemeyer, F. Ouellette, O., P. Ahlawat,, Skorjanc, V., John, E., Yang, B., Pfeifer, L., Esther Avalos, C., Pan, L., Mensi, M., Alexander Schouwink, P., Moser, Jacques-E., Hagfeldt, A., Rothlisberger, Ursula. , Zakeeruddin, Shaik M., and Michael Grätzel, Methylammonium triiodide for holistic defect engineering of α -FAPbI₃ perovskite solar cells. *ACS Energy Lett.* 2021, 6, 10, 3650–3660
4. **Alharbi E.A.**, Dar MI, Arora N, Alotaibi MH, Alzhrani YA, Yadav P, Tress W, Alyamani A, Albadri A, Zakeeruddin SM, Michael Grätzel, Perovskite Solar Cells Yielding Reproducible Photovoltage of 1.20 V. **Research Science** **2019**, **8474698**.
5. P. Ahlawat, A. Hinderhofer, **E. A. Alharbi**, H. Lu, A. Ummadisingu, H. Niu, M. Invernizzi, S. M. Zakeeruddin, M. I. Dar, F. Schreiber, A. Hagfeldt, Michael Grätzel, U. Rothlisberger, M. Parrinello, A combined molecular dynamics and experimental study of two-step process enabling low-temperature formation of phase-pure α -FAPbI₃. **Sci. Adv.** **7**, eabe3326 (2021).
6. Domanski, K., **Alharbi, E.A.**, Michael Grätzel, Hagfeldt, A., Systematic investigation of the impact of operation conditions on the degradation behaviour of perovskite solar cells. **Nat Energy** **3**, 61–67 (2018).
7. Tress, W., Domanski, K., Carlsen, B. Agarwalla,A., , **Alharbi, E.A.**, Michael Grätzel, Hagfeldt, A., Performance of perovskite solar cells under simulated temperature-illumination real-world operating conditions. **Nat Energy** **4**, 568–574 (2019).

8. Yadav, P., Dar, M. I., Arora, N., **Alharbi, E. A.**, Giordano, F., Zakeeruddin, S. M., Michael Grätzel, The Role of Rubidium in Multiple-Cation-Based High-Efficiency Perovskite Solar Cells, **Adv. Mater.** **2017**, **29**, 1701077.
9. Yadav, P., Prochowicz, Daniel, **Alharbi, E. A.**, , Zakeeruddin, Shaik M., Michael Grätzel, Intrinsic and interfacial kinetics of perovskite solar cells under photo and bias-induced degradation and recovery, **J. Mater. Chem. C**, **2017**,**5**, 7799-7805.
10. Alanazi,A., Kubicki, D. J., Prochowicz, D, **Alharbi, E. A.**, Bouduban, M. E. F., Jahanbakhshi, F., Mladenović, Milić, J. V., Giordano, F., Ren, D., Alyamani, A. Y., Albrithen, H., Albadri, A., Alotaibi, M., Moser, Jacques-E., Zakeeruddin, S. M., Rothlisberger, U., Emsley, L., Grätzel, Michael, Atomic-Level Microstructure of Efficient Formamidinium-Based Perovskite Solar Cells Stabilized by 5-Ammonium Valeric Acid Iodide Revealed by Multinuclear and Two-Dimensional Solid-State NMR, **Journal of the American Chemical Society**, **2019**, **141**, **44**, 17659–17669.
11. **Alharbi, E. A.**, A. Wojciechowski, N. AlZayed, O.V. Parasyuk, E. Gondek, P. Armatys, A.M. El-Naggar, I.V. Kityk, P. Karasinski,, IR laser induced spectral kinetics of AgGaGe₃Se₈:Cu chalcogenide crystals, **Spectrochimica Acta Part A: Molecular and Biomolecular Spectroscopy**, **111**,**2013**, 142-149.
12. **Alharbi, E. A.**, Aziz, M.A., Oyama, M. *et al.* Gold nanoparticles deposited on fluorine-doped tin oxide substrates as materials for laser operated optoelectronic devices. **J Mater Sci: Mater Electron** **24**, 2422–2425 (2013).